73

THE EFFECT OF COMPRESSIBILITY, PHASE TRANSFORMATIONS, AND ASSUMED DENSITY STRUCTURE ON MANTLE VISCOSITY INFERRED FROM EARTH'S GRAVITY FIELD.

by

Svetlana Valeryevna Panasyuk

M.S., Applied Physics, 1988
Moscow Institute of Physics and Technology, Russia

Submitted to the Department of Earth, Atmospheric, and Planetary Sciences
in Partial Fulfillment of the Requirements for the Degree of

DOCTOR OF PHILOSOPHY

at the

MASSACHUSETTS INSTITUTE OF TECHNOLOGY

June 1998

Signature of Author ....
Department of Earth, Atmospheric, and Planetary Sciences
February 20, 1998

Certified by..
Bradford H. Hager
Cecil and Ida Green Professor of Earth Sciences
Thesis supervisor

Accepted by ....
Thomas H. Jordan
Robert R. Shrock Professor of Earth and Planetary Sciences
Department Head

The Effect of Compressibility, Phase Transformations, and Assumed Density Structure on Mantle Viscosity Inferred from Earth's Gravity Field.

by

Svetlana Valeryevna Panasyuk

Submitted to the Department of Earth, Atmospheric, and Planetary Sciences
on February 20, 1998 in Partial Fulfillment of the Requirements for the Degree of
Doctor of Philosophy

ABSTRACT

We develop a quasi-analytical solution for mantle flow in a compressible, spherical shell with Newtonian rheology, allowing for continuous radial variations of viscosity. We analyze how assumptions about compressibility affect geoid kernels. In order of decreasing importance, they are: assumptions for *g(r)*, transformational superplasticity, density contrasts at the surface and core-mantle boundaries, change in flow-dynamics, compressibility of the outer core, presence of the ocean layer, and compressibility of the inner core. The largest effects from compressibility are comparable to the effects of a moderate (40%) change in the viscosity contrast between the upper and lower mantle.

We develop a model of transformational superplasticity (TS) of the mantle. We estimate the strain rate associated with reshaping of the grains required to accommodate the volume change and relate it to the macroscopic dilatation rate of the composite. The latter is evaluated both by applying a kinetic theory of the transformation and by implementing the seismically-observed sharpness of the phase transformation. We estimate that the mantle viscosity decreases by 1-2 and 2-3 orders of magnitude at 400 and 670-km depths respectively. When TS is included, the change in the long-wavelength geoid is comparable to that caused by increasing the lower mantle viscosity by a factor of two, and the change in the short-wavelength geoid is similar to an extension of an upper mantle low-viscosity zone down to 450-km depth.

We investigate the constraints on the mantle viscosity profile from the geoid and surface dynamic topography using a variety of earth's inner-structure models when both compressibility and superplasticity are accounted for. We consider uncertainties in the observables and density data, and deficiencies of forward modeling. The inversion reveals three distinct viscosity profile families that all identify one order of magnitude stiffening within the lower mantle, followed by a soft D''-layer. The main distinction between the families is the location of the lowest-viscosity layer, -- at 400-km, 670-km, or right under the lithosphere. All viscosity profiles have a reduction of viscosity within the major phase transformations, leading to reduced dynamic topography, so that whole-mantle convection is consistent with small surface topography.

Thesis Supervisor: Bradford H. Hager
Title: Cecil and Ida Green Professor of Earth Sciences

ACKNOWLEDGMENTS

I appreciate the extensive, fulfilling, and critical discussions of my work during the graduate study at MIT by the members of my thesis committee, Brad Hager, Tom Jordan, Chris Marone, Rick O'Connell, and Rob van der Hilst. Your valuable opinions always were and will be a substantial contribution in my forming as a scientist.

Special thanks are to my advisor, Brad, for taking risk of admitting his first international student, for the generous financial support during my study at MIT. My Moscow alma-mater, MIPT, had taught me to have an independent opinion and fight for it, to argue and disagree with others until an understanding is reached. Only by the end of my term at MIT I realized to appreciate Brad's patience dealing with this difficult side of my character. His unique intuition in physics allowed me to form and strengthen one of my own. I value his teaching me to work independently and letting to present the results by myself.

I thank Rick O'Connell and Tom Jordan for numerous, inspiring scientific discussions during my course work and research study, at MIT, Harvard, and different conferences. Thank you, Rick, for reducing my stress level before the defense and giving me the confidence. I gained much knowledge in kinetic theory and statistical mechanics in application to geophysics from my communications with Slava Solomatov (I remember those many hours spent on several-page e-mails back and forth!). I am grateful to Alessandro Forte for being a generous and willing collaborator, you will always be an authority for me in theoretical work.

My indoor study was well mixed by the GPS "outing club". Astonishing view of the sky-high Tien Shan mountings, glacials, and captivating glide of the Issuk-kul lake were always in my mind, even during never-ending hours against the computer while patching gaps in the data. The Central Asia GPS crew: Brad, Tom Herring, and Peter Molnar have taught me to do the experiment right and the GAMIT-software experts: Bob King and Simon McClusky have guided me through the millions of data-points. Thank you all for the great experience, I wish I could fit this part of my research into the thesis.

At MIT I met a great, supportive group of students and made new friends. Carolyn Ruppel, the incredibly thoughtful, caring, and understanding, made our transition from Russia to America much less painful and stressful. Carolyn, your unbounded energy and enthusiasm always wonder and encourage me. Steven Shapiro and his family welcomed us to a world of American traditions and hospitality. Steve's open and warm nature won Sanka's love from the first day my son came to our office. Thank you, Steve, for being such a good friend to my family and me! Summer ice-cream with the post-glacial relaxation-time discussions with Mark Simons, and the life-science chats with Mousumi Roy, Susan Mercer, Gretchen Eckhardt, Anke Friedrich and Yu Jin kept my spirits up. I am grateful to know the sixth floor students and post-docs to shear the offices, computer labs, the disc spaces and cpu: Steve, Danon Dong, Bonnie Souter, Clint Conrad, Katy Quinn, Gang Chen, Simon and Ming Fang. Thank you guys for the great parties! The discussions with always energetic fifth floor students: Jim Gaherty, Peter Puster, and Pat McGovern, the loudly bouncing rock-people upstairs: Gunter Siddiqi and Gretchen, and the top-floors geologists: Steve Parman and Anke, have opened my eyes on other geosystems.

I am thankful to Terri Macloon, who was not only the patient and understanding listener of my at first primitive English, but who introduced me to many nuances and subtleties of the American life and language. You and Jane Shapiro contribute greatly to the friendly atmosphere of the sixth floor. I would also like to thank Beverly Kozol-Tattlebaum for her warm hospitality, charming and caring spirit that sets the welcome tone of the whole Department administration.

Our Department hockey team helped me to gain back my confidence on the ice. I am grateful to Brad for introducing me to the hockey, because this game led me through the hardest time of my graduate school: several months prior the defense. This time would be much more painful and stressful, if not for the Cambridge Youth Hockey, where I started to coach my son's squirts team and still enjoy this experience. Thank you, coaches Frank and Danny, parents, and mainly the kids for trusting me, letting me to shear with you my love for the skating and hockey!

My family -- my pride, there is something which one cannot explain in words, but only through the feelings. My parents, Elena and Valerii Meleshkin, and my sister Lina are always close, always with me, even when I realize how long it takes for the telephone signal to cross the ocean and reach Moscow. Your rare visits and often calls led me through the lonely home-sick times. My dearest, precious men, Alexander and Sanka, without you I would have not be here right now. Your smiles and happiness, your joyful spirits and generous nourishment, your critique and the trust, are all so much an essential and necessary part of me and my life. This work is for you.

TABLE OF CONTENTS

Chapter I. INTRODUCTION

Recent meetings of the geophysical community recognize a rapid development of Earth sciences, from high-accuracy instruments for experiments and observations, to complicated analytical and highly sophisticated numerical models. The flood of new data and information produced requires scientists to cooperate in order to gain insight on the earth's structure and its evolution with time. It becomes necessary to develop interdisciplinary methods that allow us to assemble the results of observational, analytical, and numerical studies. However, such a unification requires a thorough analysis of each constituent of the information, an understanding of the extent to which the results of each study are robust, and an estimation of the associated uncertainties, errors, and model deficiencies.

The papers assembled within this thesis describe our ongoing effort to build an interdisciplinary approach in order to understand Earth's behavior on a global scale; long times and large distances. We start by analyzing the effects of Earth's compressibility, introducing it into a method that was used to relate the slowly creeping mantle material to anomalies in the gravitational field (Chapter II). To understand the physics of the strongest changes in the mantle's density, related to solid-solid phase transitions, we develop a model of transformational superplasticity of polycrystalline mantle material (Chapter III). We analyze the cumulative effect of compressibility and superplasticity on the mantle viscosity profile inferred from geoid field modeling (Chapter IV). We construct an inverse problem that allows us to find viscosity profiles based on the fit to the geoid and the surface dynamic topography. An analysis of the analytical method uncertainties and the errors associated with the data involved is done within Chapters IV and V. To complete the joint inversion, we develop a model of surface dynamic topography and the related uncertainties (Chapter V). A more complete description of the chapters follows.

In Chapter II we analyze the effects of mantle compressibility on geoid kernels. We develop a quasi-analytical solution to compute geoid kernels for a compressible mantle with Newtonian rheology. Compressibility enters into the flow problem directly, through the continuity equation, and indirectly, by influencing parameters such as gravitational acceleration *g(r)* and density contrasts across compositional boundaries. In order to understand all these effects, we introduce them sequentially, starting with an incompressible Earth model and ending up with a realistic model that includes a compressible mantle, inner, and outer core, phase changes in the transition zone, and an ocean.

In Chapter III we develop a model of transformational superplasticity (TS) of the mantle as it undergoes a solid-solid phase change. By considering various scenarios of the evolution of the grain-geometry in a polycrystalline material composed of two phases of different densities, we estimate the strain rate and stress associated with the reshaping of the grains required to accommodate the volume change. We relate the deviatoric strain rate of the reshaping grains to the macroscopic dilatation rate of the entire composite, where the latter is evaluated both by applying a kinetic theory of the transformation and by implementing the seismically-observed sharpness of the phase-transformation. We calculate the degree of softening of the mantle which would occur at the onset of the phase transformations at 400- and 670-km depths. To account for uncertainties in stress (or strain rate) and grain size, we construct a deformation mechanism map for a three-component mantle and a variety of grain sizes, tectonic stresses, and strain rates. We calculate the TS-field for a particular mantle flow model. We describe the effects of a phase transformation on mantle dynamics as jump conditions on the vertical and the lateral velocities across the thin two-phase layer.

In Chapter IV we investigate how gravitational potential and surface topography constrain the mantle viscosity when compressibility and superplasticity are accounted for. We perform a joint inversion of geoid and dynamic topography for the radial mantle viscosity structure with a simultaneous accounting for errors. We identify three classes of errors, which are related to density perturbations (e.g., uncertainty in the seismic tomography models), to insufficiently constrained observables (e.g., dynamic topography derived from surface topography and bathymetry after an ambiguous correction for static topography, such as subsidence of crust, oceanic lithosphere, tectosphere), and to the limitations of our analytical model (e.g., absence of lateral viscosity variations). We estimate the errors for geoid and dynamic topography in the spectral domain and define a fitting criterion. Our minimization function weights the squared deviation of the compared quantities with the corresponding error, so that the components with the most reliability contribute to the solution more strongly than less certain ones. To improve the convergence and accuracy of the inverse method, we modify the analytical approach developed in Chapter II in order to account for a continuous, exponential variation of viscosity, together with a possible reduction of viscosity within the phase change regions due to the effect of transformational superplasticity.

In Chapter V we create a model of surface dynamic topography based on a global crustal model and the ages of the oceanic floor. We model the static topography fields following several commonly accepted methods. Since the modeled fields scatter widely around the mean, we build a model of dynamic topography by reducing the observed topography by the field averaged over the assemblage of modeled static topography fields. Carrying the uncertainties associated with the crustal structure and the oceanic ages and with the scatter of static topography, we estimate the spatial and the spectral errors which accompany our model. We compare the dynamic topography obtained by correction for the static topography with the dynamic topography calculated based on the geoid-topography inversion.

Chapter II. UNDERSTANDING THE EFFECTS OF MANTLE COMPRESSIBILITY ON GEOID KERNELS[1]

SUMMARY

We develop a quasi-analytical solution to compute geoid kernels for a compressible mantle with Newtonian rheology. By separating the stresses induced by self-gravitation from the stresses resulting from viscous flow, we simplify the equations and gain some insight. For realistic variations in the background density field $\rho_0(r)$, the solution, obtained using propagator matrices, converges rapidly. Compressibility enters into the flow problem directly, through the continuity equation, and indirectly, by influencing parameters such as gravitational acceleration $g(r)$ and density contrasts across compositional boundaries. In order to understand all these effects, we introduce them sequentially, starting with an incompressible earth model and ending up with a realistic compressible model that includes a compressible inner and outer core, phase changes in the transition zone, and an ocean.

The largest effects on geoid kernels are from different assumptions for $g(r)$; possible effects of transformational superplasticity and differences in assumptions for density contrasts at the surface and at the core-mantle boundary are next in importance. The effects of compressibility on the flow itself are somewhat smaller, followed by the effect of compressibility of the outer core. A gravitationally consistent treatment of the ocean layer yields geoid kernels that are very similar to those for a "dry" planet. The compressibility of the inner core has a negligible impact on the geoid kernels. The largest effects from compressibility are comparable to the effects of a moderate (40 per cent) change in the viscosity contrast between the upper and lower mantle.

Key words: geoid, Green's functions, mantle convention, mantle reology, mantle viscosity, phase transitions.

---

[1] published in *Geophysical Journal International*, by Panasyuk, S.V., Hager, B.H., and A.M. Forte, **124**, 121-133, 1996.

INTRODUCTION

Since the pioneering work of Pekeris (1935), it has been recognized that mantle convection causes dynamic deformation of the Earth's surface, and that this surface deformation has an important, often dominant, effect on the geoid. With the development of geophysical models of mantle heterogeneity, there has been substantial interest in increasingly realistic computations of geoid anomalies for a given distribution of density anomalies within the mantle.

Parsons and Daly (1983) formulated the problem of the calculation of geoid anomalies for a convecting mantle in terms of kernels. They expressed lateral variations in density, as well as geoid anomalies, in the harmonic domain. For a model in which there are no lateral variations in viscosity, one can compute the geoid kernel, the geoid produced by a unit mass anomaly of a given wavelength at a given depth, including the effects of dynamic topography. The total geoid anomaly caused by an assumed density distribution in the mantle is obtained by a convolution of these kernels with the density field. Parsons and Daly (1983) presented kernels for an incompressible, isoviscous mantle, assuming Cartesian geometry.

Richards and Hager (1984) and Ricard *et al.* (1984) extended the kernel approach to spherical geometry and included the effects of self-gravitation, a fluid core, and radial variations in viscosity. The resulting equations can be solved analytically using propagator matrix techniques (e.g., Gantmacher 1960; Hager and O'Connell 1981; Hager and Clayton 1989) to calculate geoid kernels for an incompressible planet. Because they had determined that the net effects of adding a self-gravitating ocean layer on geoid kernels are negligible to first order, these authors published only the simpler formulation for an oceanless planet, without explicitly mentioning the ocean. Forte and Peltier (1987) extended the Earth model to include the effect of a global ocean layer on dynamic topography and the geoid, but under the assumption that the ocean surface remains spherical, rather than following an equipotential surface. Using either approach, and taking the distribution of interior density anomalies as given by a plate tectonic model or by seismic tomography, it is possible to generate models that explain most of the long-wavelength geoid (e.g., Hager *et al.* 1985; Forte and Peltier 1987; Hager and Clayton 1989; Hager and Richards 1989; King and Masters 1992; Ricard *et al.* 1993).

However, a parcel of mantle that flows from the uppermost mantle to the core-mantle boundary almost doubles in density, so the effects of compressibility on mantle flow and geoid kernels should also be considered. Forte and Peltier (1991a) and Dehant and Wahr (1991) derived the equations for compressible flow driven by internal density heterogeneities. The resulting equations are more complicated than for incompressible flow, and they were solved using numerical techniques. Forte and Peltier (1991a) investigated the effects of realistic radial density variations on geoid kernels using the density profile from earth model PREM (Dziewonski and Anderson, 1981) and found that for a constant-viscosity mantle, these effects result in changes in geoid kernels of 10 per cent or less, with relatively little dependence on spherical harmonic degree.

An isoviscous mantle cannot, however, explain the geoid. Although models of mantle viscosity structure that predict the observed geoid vary in detail, all have an increase in viscosity between the upper and lower regions of the mantle. For these models, geoid kernels typically change sign with depth. In this case, Forte and Peltier (1991a) showed that the kernels calculated for an incompressible model can be quite different from those calculated for a more realistic model with a compressible mantle and outer core. They corrected their previous (1987) formulation to include a gravitationally consistent treatment of the ocean, which allows its surface to deform according to the equipotential surface. The calculated geoid differed significantly (up to 32 per cent at degree 2 for their preferred viscosity profile) from one computed under the assumption of an undeformed (spherical) ocean surface. They also presented a gravitationally consistent treatment of a compressible outer core, concluding that its impact was comparable to that of the ocean surface deformation (up to 26 per cent at degree 2). Forte and Peltier (1991b) also noted the strong effect of the additional internal loads created by the interaction of the perturbed gravitational potential with the radial gradient of the background density profile in the mantle.

These results elicited significant interest and controversy. For example, Thoraval, Machetel and Cazenave (1994) computed kernels for a compressible mantle with the PREM density structure, including a deformable ocean surface. They concluded that the deformation of the ocean surface has an important effect, but that compressibility of the outer core has a negligible effect, in agreement with the conclusions of Ricard *et al.* (1984), who had used a simpler model with an inviscid mantle to address the effects of compressibility. Corrieu, Thoraval and Ricard (1995) discussed the effect of the ocean by comparing the total response of a dry versus a wet planet. They concluded that the total effect of the ocean is negligible, as is compressibility of the outer core.

One of the main reasons that these seemingly contradictory conclusions have been reached is that there are a number of parameters that affect geoid kernels, and different workers have assumed different values for these parameters. These different parameter choices have had effects on the kernels that are often larger than the effect of compressibility alone. For example, the function assumed for the gravitational acceleration $g(r)$ has varied among models and the effects on the geoid kernels of assuming different $g(r)$ are large compared to the effects of compressibility on the flow itself (Panasyuk, Forte and Hager, 1993). The treatment of the ocean is also different in different models. In our view, a useful way to understand the differences among the models is to introduce these differences one at a time, investigating the effect of each separately.

In this paper, we present a detailed analysis of the effects of compressibility on geoid kernels. We first present the equations governing flow in a form that leads to physical insight into the separation of the effects of self-gravitation and of flow-induced stresses, and also which can be solved quasi-analytically using a propagator matrix technique. We then consider the various effects of compressibility separately. First, we investigate the effects of $g(r)$. Next we determine the effects of different assumptions about density contrasts at the surface and at the core-mantle boundary. We then investigate the effects of compressibility, *sensu stricto*, on geoid kernels, and examine the effects of transformational superplasticity at phase change boundaries. We next determine the effects of compressibility of the core and deformation of the inner core, as well as the effects of the ocean. To place these effects in context, we also consider the effects on geoid kernels of altering the viscosity contrast between the upper and lower mantle by a moderate amount.

MATHEMATICAL FORMULATION

We can treat the Earth's mantle as a high-viscosity fluid, with flow driven by a distribution of density anomalies that is assumed known, for example from a geodynamical model (e.g., Hager 1984; Forte and Peltier 1991a; Ricard *et al.* 1993) or from seismic tomography (e.g., Hager *et al.* 1985; Forte and Peltier 1991a; Forte, Dziewonski and Woodward 1993; King and Masters 1992). The governing equations include the continuity equation

$$\frac{\partial \rho}{\partial t} + \operatorname{div}(\rho \mathbf{v}) = 0, \tag{II-1}$$

and the equation of motion

$$\rho \frac{d\mathbf{v}}{dt} = \mathbf{F}, \tag{II-2}$$

where ρ is density, $\mathbf{v}$ is the flow velocity, and $\mathbf{F}$ denotes both viscous forces and gravitational forces: $\mathbf{F} = \operatorname{div}\tau + \rho \nabla V$. The potential V is given by Poisson's equation:

$$\Delta V = -4\pi\gamma\rho, \tag{II-3}$$

where γ is the gravitational constant. Finally, we assume the constitutive law for a Newtonian viscous fluid with zero bulk viscosity:

$$\tau_{ij} = -p\delta_{ij} + \tau_{ij}^{\mathrm{d}} = -p\delta_{ij} + 2\eta\dot{\varepsilon}_{ij}^{\mathrm{d}} \tag{II-4}$$

where p is the pressure, τ_{ij}^{d} is the deviatoric stress, $\dot{\varepsilon}_{ij}^{\mathrm{d}} = \dot{\varepsilon}_{ij} - \dot{\varepsilon}_{kk}\delta_{ij}/3$ is the deviatoric strain rate, and η is the shear viscosity. Since the density perturbations that excite mantle flow are much smaller than the ambient hydrostatic densities, it is useful to express the flow-related quantities as first-order deviations from their hydrostatic reference values:

$$\begin{aligned} \rho(r,\theta,\vartheta) &= \rho_0(r) + \rho_1(r,\theta,\vartheta) \\ p(r,\theta,\vartheta) &= p_0(r) + p_1(r,\theta,\vartheta) \\ V(r,\theta,\vartheta) &= V_0(r) + V_1(r,\theta,\vartheta) \end{aligned} \tag{II-5}$$

Subtracting the hydrostatic reference state and ignoring the inertial term in (2), as is appropriate for mantle flow, leads to:

$$\begin{cases} (\rho_0+\rho_1)\mathrm{div}(\mathbf{v})+\mathbf{v}\cdot\nabla\,(\rho_0+\rho_1)=0 \\ -\nabla p_1+\mathrm{div}(\tau^{\mathrm{d}})+\rho_0\nabla V_1+\rho_1\nabla V_0=0 \\ \Delta V_1=-4\pi\gamma\rho_1 \end{cases} \tag{II-6}$$

In eq. (6), the time derivative of density is ignored since mantle-flow velocities are much smaller that the acoustic-wave velocity (e.g., Landau and Lifshitz 1987). This system is solved in spherical coordinates (r,θ,φ). The continuity equation, keeping terms to first-order accuracy, is:

$$\mathrm{div}(\rho\mathbf{v})\approx\rho_0(r)\mathrm{div}(\mathbf{v})+v_r\frac{\partial\rho_0(r)}{\partial r}=0 \tag{II-7}$$

or

$$\mathrm{div}(\mathbf{v})=-\frac{v_r}{\rho_0(r)}\frac{\partial\rho_0(r)}{\partial r}=-\chi\cdot\frac{v_r}{r}, \tag{II-8}$$

where $\chi(r)=\frac{r}{\rho_0(r)}\frac{\partial\rho_0(r)}{\partial r}$

The momentum (Stokes) equations are:

$$\frac{r\partial}{\partial r}(-p_1+\rho_0V_1)-\chi\rho_0V_1+r\mathrm{div}_{\mathrm{r}}\tau^{\mathrm{d}}=r\rho_1 g \tag{II-9a}$$

$$\left(\mp\frac{\partial}{\partial\theta}+\frac{i}{\sin\theta}\frac{\partial}{\partial\varphi}\right)(-p_1+\rho_0V_1)+r\left(\mp\mathrm{div}_\theta\tau^{\mathrm{d}}+i\mathrm{div}_\varphi\tau^{\mathrm{d}}\right)=0 \tag{II-9b}$$

The variables are expressed in terms of products of radial functions and spherical harmonics [e.g., Hager and Clayton (1989), although here we use complex harmonics]:

$$v_r(r,\theta,\varphi)=\sum_{l,m}y_1^{lm}(r)\mathrm{Y}_{lm}(\theta,\varphi) \tag{II-10a}$$

$$v_{\theta,\varphi}(r,\theta,\varphi)=\sum_{l,m}\left\{y_2^{lm}(r)\mathrm{Y}_{lm}^{\theta,\varphi}(\theta,\varphi)\pm y_9^{lm}(r)\mathrm{Y}_{lm}^{\varphi,\theta}(\theta,\varphi)\right\} \tag{II-10b}$$

$$\tau_{rr}(r,\theta,\varphi)=\sum_{l,m} y_3^{lm}(r)\mathrm{Y}_{lm}(\theta,\varphi) \tag{II-10c}$$

$$\tau_{r\theta,\varphi}(r,\theta,\varphi)=\sum_{l,m}\left\{y_4^{lm}(r)\mathrm{Y}_{lm}^{\theta,\varphi}(\theta,\varphi)\pm y_{10}^{lm}(r)\mathrm{Y}_{lm}^{\varphi,\theta}(\theta,\varphi)\right\} \tag{II-10d}$$

$$V_1(r,\theta,\varphi)=\sum_{l,m} y_5^{lm}(r)\mathrm{Y}_{lm}(\theta,\varphi) \qquad \frac{\partial V_1(r,\theta,\varphi)}{\partial r}=\sum_{l,m} y_6^{lm}(r)\mathrm{Y}_{lm}(\theta,\varphi) \tag{II-10e}$$

$$\rho_1(r,\theta,\varphi)=\sum_{l,m} y_8^{lm}(r)\mathrm{Y}_{lm}(\theta,\varphi), \tag{II-10f}$$

where $f_i(r,\theta,\varphi)=\sum_{l,m} y_i^{lm}(r)\mathrm{Y}_{lm}(\theta,\varphi)=\sum_{l=0}^{L}\sum_{m=-l}^{l} y_i^{lm}(r)P_l^m(\cos\theta)\exp(im\varphi)$

and derivatives are $Y_{lm}^{\theta}(\theta,\varphi)=\dfrac{\partial Y_{lm}(\theta,\varphi)}{\partial\theta}$ and $Y_{lm}^{\varphi}(\theta,\varphi)=\dfrac{1}{\sin\theta}\dfrac{\partial Y_{lm}(\theta,\varphi)}{\partial\varphi}$.

To make the derivation of the set of equations simpler and the resulting equations better conditioned, we used the operators

$$\partial^0=\frac{r\partial}{\partial r} \text{ and } \partial^{\pm}=\frac{1}{\Lambda}\left(\mp\frac{\partial}{\partial\theta}+\frac{i}{\sin\theta}\frac{\partial}{\partial\varphi}\right),$$

where $\mathit{\Lambda}=\sqrt{l(l+1)}$,

and a new set of poloidal variables:

$$\mathbf{u}(r)=\begin{bmatrix} y_1\bar{\eta} & y_2\bar{\eta}\Lambda & (y_3+\rho_0 y_5)r & y_4 r\Lambda & y_5 r\bar{\rho}\Lambda & y_6 r^2\bar{\rho}\end{bmatrix}^{\mathrm{T}} \tag{II-11}$$

where $\bar{\eta}$ is a (constant) reference viscosity and $\bar{\rho}$ is a (constant) reference density.

A few comments about the choice for u_3 may be useful. The term $\rho_0 y_5$ represents the contribution to the total perturbed pressure from the interaction of the perturbed potential with the background density field. This gravitationally induced pressure perturbation, which is not directly associated with viscous flow, is subtracted from the total τ_{rr} to keep only that part of τ_{rr} associated with viscous flow in u_3.

After some manipulation, we obtain the following matrix equation:

$$\partial^0\mathbf{u}_l=\mathbf{A}_l\mathbf{u}_l+\mathbf{b}_l \tag{II-12}$$

where the source vector is

$$\mathbf{b}_\ell(r) = \begin{bmatrix} 0 & 0 & g(r) & 0 & 0 & -4\pi\gamma r\bar{\rho} \end{bmatrix}^{\mathrm{T}} r^2 y_8 \tag{II-13}$$

and, defining $\eta^* \equiv \eta_0(r)/\bar{\eta}$, the matrix $\mathbf{A}_l$ is

$$\begin{bmatrix} -(2+\chi) & \Lambda & 0 & 0 & 0 & 0 \\ -\Lambda & 1 & 0 & 1/\eta^* & 0 & 0 \\ (12+4\chi)\eta^* & -6\Lambda\eta^* & 1 & \Lambda & \chi\rho_0/\Lambda\bar{\rho} & 0 \\ -(6+2\chi)\Lambda\eta^* & 2(2\Lambda^2-1)\eta^* & -\Lambda & -2 & 0 & 0 \\ 0 & 0 & 0 & 0 & 1 & \Lambda \\ 0 & 0 & 0 & 0 & \Lambda & 0 \end{bmatrix} \tag{II-14}$$

Henceforth, for notational convenience, we omit the subscript *l*.

Note that $\mathbf{A}$ can be represented as a sum of three matrix expressions:

$$\mathbf{A}(r) = \mathbf{A}_0 + \chi(r)\mathbf{A}_1 + \frac{\chi(r)\rho_0(r)}{\bar{\rho}}\mathbf{A}_2 \tag{II-15}$$

Here $\mathbf{A}_0$ is equivalent to the matrix for incompressible flow (Hager and Clayton, 1989). The matrix $\mathbf{A}_1$ gives the effect of compressibility on flow. Compressibility also enters into **b** due to its effect on $g(r)$.

We can gain some physical insight into $\mathbf{A}_2$ (see also, Forte and Peltier, 1991b), which expresses the coupling of u_3, the term involving the radial stress caused by flow, and u_5, the potential term, by considering the problem of a planet loaded by an external potential. [If this external potential is the tidal potential, this is the classic problem in which Love numbers are defined (e.g., Vening Meinesz 1946; Munk and MacDonald 1960; Sleep and Phillips 1979; Hager 1983).] For loading by an external potential V_1, after equilibrium is reached, there is no flow, so $[u_1\ u_2\ u_3\ u_4]$ are identically zero throughout the interior. In particular, $u_3 = 0$ requires that $\tau_{rr} = -\rho_0 V_1$, so the total radial stress is due only to the potential, with no contribution from viscous dissipation. The requirement that $\partial u_3 = 0$ is met, because, in the case of loading of a compressible fluid planet by an external potential, the condition that surfaces of constant density be equipotential surfaces (displaced by an amount δN) gives for the perturbed density ρ_1:

$$\rho_1 = -\frac{\partial \rho_0}{\partial r}\delta N = -\frac{\chi \rho_0}{r}\frac{V_1}{g(r)} \tag{II-16}$$

In this case, the contribution to ∂u_3 from b_3 cancels the contribution from $A_{35}u_5$. Thus the single nonzero term in $\mathbf{A}_2$ expresses the "correction" to the perturbed density for the gravitationally induced change in pressure.

Propagator matrix

Because $\mathbf{A}_0$ is a constant within a layer of uniform viscosity, the set of equations for incompressible flow can be solved analytically using the propagator matrix technique. The depth dependencies of $\mathbf{A}_1$ and $\mathbf{A}_2$ bring additional complications into the solution, since $\mathbf{A}(r)$ is no longer permutable in subintervals. However, under the condition that $\mathbf{A}(r)$ is "almost" permutable in small intervals of thickness Δr between radii r_1 and r_2, that is, that $\mathrm{A}(r')\mathrm{A}(r'') = \mathrm{A}(r'')\mathrm{A}(r') + (*)$, $(r', r'') \in (r_1, r_2)$, where $(*)$ is much less than the product of the matrices, the propagator $\mathbf{P}_a^c$ between the upper external boundary, *a*, and lower one, *c*, can be written as

$$\mathbf{P}_a^c(\mathbf{A}) = \lim_{\Delta r \to 0} \exp\left\{ \int_{c+\Delta r}^{c} \mathbf{A}(r) d \ln r \right\} \times \ldots \times \exp\left\{ \int_{a}^{a-\Delta r} \mathbf{A}(r) d \ln r \right\}, \tag{II-17}$$

where we evaluate analytically the integrals in the sub-propagators $\mathbf{P}_{r_2}^{r_1}$:

$$\mathbf{P}_{r_2}^{r_1} = \exp\left\{ \mathbf{A}_0 \ln\frac{r_1}{r_2} + \mathbf{A}_1 \ln\frac{\rho_0(r_1)}{\rho_0(r_2)} + \mathbf{A}_2 \frac{\rho_0(r_1) - \rho_0(r_2)}{\bar{\rho}} \right\} \tag{II-18}$$

We can write the value of the $\mathbf{u}$ vector on boundary *c* in terms of its value on boundary *a* and the source terms $\mathbf{b}(r)$ as

$$\mathbf{u}(c) = \mathbf{P}_a^c \mathbf{u}(a) + \int_a^c \mathbf{P}_r^c \mathbf{b}(r)\, dr/r \tag{II-19}$$

Assuming that neither $\mathbf{P}_r^c$ nor $\mathbf{b}(r)$ varies rapidly with depth, it is computationally convenient to approximate the continuous volumetric density contrast $\rho_1(r_j)$ distributed throughout the j-interval $\left(r_j - \delta r_j/2, r_j + \delta r_j/2\right)$ as a sheet density contrast $\sigma\left(r_j\right) = \rho_1\left(r_j\right)\delta r_j$. Then the integral in (19) can be represented as a summation:

$$\mathbf{u}(c) = \mathbf{P}_a^c\mathbf{u}(a) + \sum_{j=1}^{J}\mathbf{d}\left(r_j\right) \tag{II-20}$$

where the source vector

$$\mathbf{d}\left(r_j\right) = \mathbf{P}_{r_j}^c\left[0 \quad 0 \quad g\left(r_j\right) \quad 0 \quad 0 \quad -4\pi\gamma r_j\bar{\rho}\right]^{\mathrm{T}} r_j\sigma\left(r_j\right).$$

Expression (20) is a quasi-analytical solution to the system of differential equations (12) expressed in terms of the matrixants of boundary values and sources. The solution is quasi-analytic in that we evaluate the limit in (17) numerically. The product of layer propagators converges to its limit in (17) rapidly and monotonically. Sufficient accuracy is achieved by dividing the mantle into ~ 30 layers. Except for the case of phase changes, discussed below, **u** is continuous across the mantle.

Boundary conditions

PREM contains discontinuities in $\rho_0(r)$ at a number of depths. In calculating geoid kernels, we must choose which of these to treat as boundaries separating layers of different composition, and which to treat as due to phase changes. We assume that the discontinuities in PREM at 220, 400 and 670 km depth are due to phase changes and that the other discontinuities are compositional in origin (the discontinuity in the PREM model at 220 km is probably more spread out in the Earth.). These are the boundaries between the inner and outer cores (ICB) at r=1221.5 km, between the core and the mantle (CMB) at r=3480 km, between mantle and crust at a depth of 24.4 km, between upper and lower crust at a depth of 15 km, between upper crust and ocean at 3 km depth, and the boundary between ocean and air at the surface (SUR).

We assume that the crust responds as a passive layer on top of the convecting mantle, so that the crust does not change its thickness, but is only deflected radially, in response to mantle flow. For this assumption, the dynamic topography and total mass anomalies are nearly identical to those for a model which has no crust. For simplicity, we replace the lower and upper crust in the PREM model with material with the same density as the top of the mantle (ρ_0=3.38 Mg m^{-3}), and define the interface at 3 km depth as the "ocean-mantle boundary" (OMB). Alternatively, one could treat the boundaries at 24.4 km and 15 km depth as phase changes, allowing flow to penetrate through the crust. The dynamic topography in such a treatment is different, but the geoid kernels are unaffected for density anomalies within the mantle.

Mantle flow and self-gravitation lead to dynamically maintained topography at the compositional boundaries SUR, OMB, CMB, and ICB. Since the time scale of mantle convection is long compared to the time scale for development of quasi-steady dynamic topography, we assume that the radial velocity at each of these compositional interfaces is zero (e.g., Richards and Hager, 1984). At any (deformed) boundary between two materials, the physical boundary conditions are that, in addition to the normal velocity vanishing, the tangential velocity, the traction vector, the potential, and the gravitational acceleration are all continuous. However, the matrixant approach requires the propagation of the boundary values between surfaces of constant radius. The physical boundary conditions at a boundary *d* deflected a distance δb away from reference radius *r* can be analytically continued to *r* using a Taylor's series (e.g., Richards and Hager 1984; Hager and Clayton 1989; Forte and Peltier 1991a). To first order, mathematically, there is a jump in normal stress at the reference boundary

$$\tau_{rr}\Big|_{r-}^{r+} = \tau_{rr}\Big|_{d-}^{d+} - \frac{\partial \tau_{rr}}{\partial r}\Bigg|_{d-}^{d+} \delta b \approx 0 - \rho_0 g\Big|_{d-}^{d+} \delta b = \Delta\rho^d g \delta b\,, \tag{II-21}$$

where we choose the unconventional definition $\Delta\rho^d = \rho_0^{d-} - \rho_0^{d+}$ to keep the numerical value positive. There is also a jump in perturbed gravitational acceleration g_1:

$$\frac{\partial g_1}{\partial r}\Bigg|_{d-}^{d+} = -4\pi\gamma\rho_0\Big|_{d-}^{d+} = 4\pi\gamma\Delta\rho^d \tag{II-22}$$

at the reference boundary. These result in a jump condition for **u**:

$$\mathbf{u}\big|_{b-}^{b+} = \left[0 \quad 0 \quad \Delta\rho^b b g^b\left(\delta b - V_1^b/g^b\right) \quad 0 \quad 0 \quad -4\pi\gamma b^2 \Delta\rho^b \bar{\rho}\delta b\right]^{\mathrm{T}}. \qquad \text{(II-23)}$$

Note that the jump in u_3 depends on the deflection δb away from the equipotential surface V_1^b/g^b, not from its reference radius. This deflection is the quantity that is preserved in the geological record of sea-level. We define the quantity $\left(\delta b - V_1^b/g^b\right)$ as the "dynamic" topography, i.e., that part of the topography maintained by stresses from viscous flow. The total topography δb has contributions both from flow stresses and from gravitationally induced boundary deformation V_1^b/g^b.

We now apply these boundary conditions to the interfaces that we assume to be of compositional origin. To begin, just above SUR $(r=e)$, the perturbed potential satisfies Laplace's equation, so

$$\begin{cases} V_1(r) = V_1^{e+}\left(\dfrac{e}{r}\right)^{l+1} = V_1^{e+}, \text{ for } r \to e+ \\ g_1(r) = -\dfrac{l+1}{r}V_1^{e+}\left(\dfrac{e}{r}\right)^{l+1} = -\dfrac{l+1}{r}V_1^{e+}, \text{ for } r \to e+ \end{cases} \qquad \text{(II-24)}$$

To apply eq. (23), we must know δe, but this is just the surface geoid anomaly $\delta e = \delta N^e = V_1^e/g^e$, so

$$\begin{cases} V_1^{e-} = V_1^{e+} \\ g_1^{e-} = g_1^{e+} - g_1\big|_{e-}^{e+} = -\dfrac{l+1}{e}V_1^{e+} + 4\pi\gamma\Delta\rho^e\delta e = \left(-(l+1) + \dfrac{4\pi\gamma\Delta\rho^e e}{g^e}\right)\dfrac{V_1^{e+}}{e}. \end{cases} \qquad \text{(II-25)}$$

Note that u_3 remains zero within the ocean because the total stress is just due to the gravitational potential, with no contribution from viscous dissipation.

To determine $\mathbf{u}^{a+}$, we need only to "propagate" u_5 and u_6 from the SUR to the OMB (r=a) using Laplace's equation. The solution in terms of $R = a/e$ becomes:

$$V_1^{a+} = G_1 \cdot V_1^{e+},$$

where

$$G_1 = R^{-(l+1)} + \left(R^l - R^{-(l+1)}\right) \cdot \frac{4\pi\gamma\Delta\rho^e e/g^e}{2l+1}; \qquad \text{(II-26)}$$

$$g_{r1}^{a+} = G_2 V_1^{e+}/a\,,$$

where

$$G_2 = -(l+1)R^{-(l+1)} + \left(lR^l + (l+1)R^{-(l+1)}\right)\frac{4\pi\gamma\Delta\rho^e e/g^e}{2l+1}\,. \qquad \text{(II-27)}$$

The values of G_1 and G_2 are given in Table 1 for degrees 2-5. Because R is very close to unity, G_1 is nearly unity and $G_2 \approx -l-0.5$, as can be seen from the first-order Taylor's series approximations

$$G_1 \approx 1 + l\cdot\left(\frac{e-a}{e}\right) \text{ and } G_2 \approx -(l+1) + \frac{3\Delta\rho^e}{\bar{\rho}}\,.$$

The quantities G_1 and G_2 are derived in a similar way to the quantities P and G in Forte and Peltier (1991a), with a different normalization and misprints corrected.

Table 1. G Matrix

l	G_0	G_1	G_2
2	1.7927	1.001152	-2.4488
3	2.8385	1.001624	-3.4521
4	3.8673	1.002096	-4.4563
5	4.8872	1.002568	-5.4615

The remaining boundary is the CMB. Within the core, the entire perturbed stress is due to interaction of the background density with the perturbed potential. The perturbed radial gravitational acceleration is proportional to the perturbed potential:

$$g_1^{c-} = G_0 V_1^{c-}/c \qquad \text{(II-28)}$$

For an incompressible core, G_0 is found by solving Laplace's equation within a homogeneous core, with the simple result that $G_0 = l$.

Compressible inner and outer core

For a compressible core, the perturbed potential results in density anomalies within the core (e.g., Munk and McDonald 1960; Forte and Peltier 1991a), since surfaces of equal potential and equal density must coincide. Furthermore, there is a mass anomaly that results from the deflection of the ICB.

The potential in the outer core satisfies Poisson's equation with a "secondary" source defined as

$$\delta\rho^{S} = -\frac{V_1}{g}\frac{\partial\rho_0}{\partial r}.$$

In analogy with the gravitational part of system (14), we write Poisson's equation as a system of homogeneous differential equations:

$$\begin{cases} \partial u_5 = u_5 + u_6 \\ \partial u_6 = \left[\Lambda^2 + 4\pi\gamma\chi\rho_0 r/g\right]u_5 \end{cases}, \tag{II-29}$$

or in matrix form: $\partial\mathbf{u} = \mathrm{A}(r)\mathbf{u}$,

where $\mathbf{u}(r) = \begin{bmatrix} V_1(r)r \\ g_1(r)r^2 \end{bmatrix}$,

and the matrix **A** can be presented as a sum of two matrix expressions:

$$\mathrm{A}(r) = \begin{bmatrix} 1 & 1 \\ \Lambda^2 & 0 \end{bmatrix} + 4\pi\gamma\chi\frac{\rho_0 r}{g(r)}\begin{bmatrix} 0 & 0 \\ 1 & 0 \end{bmatrix} = \mathrm{A}_0 + f(r)r\mathrm{A}_1, \tag{II-30}$$

with $\mathbf{A}_0$, $\mathbf{A}_1$ matrices that are independent of radius.

The solution can be obtained in the same manner as for compressible mantle flow. The values of the **u** vector between the CMB (c^-) and ICB (b^+) are related by

$$\mathbf{u}(c^-) = \mathbf{P}_{b+}^{c-}\mathbf{u}(b^+), \tag{II-31}$$

where the propagator is $\mathbf{P}_b^c = \mathbf{P}_{c+\Delta r}^{c}\ldots\mathbf{P}_{b-\Delta r}^{b-2\Delta}\mathbf{P}_b^{b-\Delta r}$ and each sub-matrixant can be approximated for small intervals Δr as

$$\mathbf{P}_{r_2}^{r_1} = \exp\left\{\int_{r_2}^{r_1}\mathrm{A}(r)\frac{1}{r}dr\right\} = \exp\left\{\mathrm{A}_0\ln\frac{r_1}{r_2} + \mathrm{A}_1 4\pi\gamma\int_{r_2}^{r_1}\frac{\chi\rho_0}{g(r)}dr\right\}. \tag{II-32}$$

The connection between the two boundaries can be written as:

$$\begin{bmatrix} cV_1^{c-} \\ c^2 g_1^{c-} \end{bmatrix} = \mathbf{P}_{b+}^{c-}\cdot\begin{bmatrix} bV_1^{b+} \\ b^2 g_1^{b+} \end{bmatrix} \tag{II-33}$$

Therefore, compressibility of the outer core is expressed as a self-gravitational load accounted for in calculating the propagator (32).

The potential anomaly and its derivative on the ICB can be related to the value for the potential at a surface that is very close to the centre of the Earth. The inner core is treated as a passive (i.e. non-convecting) creeping solid, gravitationally loaded by the perturbed potential, and is in a quasi-static equilibrium (Forte and Peltier, 1991a). It can be treated as a compressible fluid sphere with a surface of constant potential. Applying the boundary conditions across the reference ICB, the value of the **u** vector on the outside of the reference ICB in terms of its values inside is:

$$\begin{cases} bV_1^{b+} = bV_1^{b-} \\ b^2 g_1^{b+} = b^2\left(g_1^{b-} - 4\pi\gamma\Delta\rho^b V_1^{b-}/g^b\right) \end{cases}; \tag{II-34}$$

where the deflection of the equipotential surface is $\delta b = V_1^b/g^b$.

Substitution of eq. (34) into eq. (33) gives the matrix equation

$$\begin{bmatrix} cV_1^{c-} \\ c^2 g_1^{c-} \end{bmatrix} = \mathbf{P}_{b+}^{c-} \begin{bmatrix} 1 & 0 \\ -4\pi\gamma b\Delta\rho^b/g^b & 1 \end{bmatrix} \begin{bmatrix} bV_1^{b-} \\ b^2 g_1^{b-} \end{bmatrix}, \tag{II-35}$$

where the connection between the surface of the compressible inner core and the surface of the arbitrarily chosen small incompressible sphere around the center of the Earth is similar to the solution of Poisson's equation for the outer core, eq. (33), and can be written using boundary conditions across the surface of this sphere at reference radius x as

$$\begin{bmatrix} bV_1^{b-} \\ b^2 g_1^{b-} \end{bmatrix} = \mathbf{P}_{x+}^{b-} \begin{bmatrix} xV_1^{x+} \\ x^2 g_1^{x+} \end{bmatrix} = \mathbf{P}_{x+}^{b-} \begin{bmatrix} xV_1^{x+} \\ x\left(l - 4\pi\gamma x\Delta\rho^x/g^x\right)V_1^{x+} \end{bmatrix}. \tag{II-36}$$

Combining eq. (35) and eq. (36) into one matrix equation gives

$$\begin{bmatrix} cV_1^{c-} \\ c^2 g_1^{c-} \end{bmatrix} = \mathbf{P}^{\text{core}} \begin{bmatrix} 1 \\ l - 4\pi\gamma x\Delta\rho^x/g^x \end{bmatrix} xV_1^{x+}, \tag{II-37}$$

where the complete matrixant for the compressible core is defined as

$$\mathbf{P}^{\text{core}} = \mathbf{P}_{b+}^{c-} \begin{bmatrix} 1 & 0 \\ -4\pi\gamma b\Delta\rho^b/g^b & 1 \end{bmatrix} \mathbf{P}_{x+}^{b-}. \tag{II-38}$$

The matrix equation (37) can be solved with respect to g_{r1}^{c-} in terms of V_1^{c-} using eq. (28), $g_1^{c-} = G_0 \cdot V_1^{c-} / c$ to define the unknown quantity G_0:

$$G_0 = \frac{\begin{bmatrix} \mathbf{P}_{21}^{core} & \mathbf{P}_{22}^{core} \end{bmatrix} \begin{bmatrix} 1 \\ l - 4\pi\gamma x \Delta\rho^x / g^x \end{bmatrix}}{\begin{bmatrix} \mathbf{P}_{11}^{core} & \mathbf{P}_{12}^{core} \end{bmatrix} \begin{bmatrix} 1 \\ l - 4\pi\gamma x \Delta\rho^x / g^x \end{bmatrix}}. \qquad \text{(II-39)}$$

The quantity G_0 derived here is similar to the quantity R derived in Forte and Peltier (1991a), but includes the effect of a compressible inner core.

As can be seen from the last equation, the effects of core compressibility and the deflection of all internal surfaces are decoupled. The importance of the outer and inner core self-gravitational load for geoid calculations can be checked by letting the value for the background density be constant, i.e. $\chi = 0$ in the propagator eq. (32) and similarly for the inner core. The isolated effect of accounting for the mass anomaly due to deflection of the ICB can be determined by setting its value to zero, i.e. $\Delta\rho^b = 0$ in the expression for the complete matrixant (38).

Values of G_0 for the PREM density structure are given in Table 1. For $l = 2$, $G_0 / l \approx 0.9$, with the value approaching unity as l increases.

Phase changes

PREM contains discontinuities in $\rho_0(r)$ at several depths z within the mantle (670, 400, and 220 km) that we treat as phase boundaries, where density changes continuously, albeit very rapidly, over intervals of thickness Δz of approximately 1 km (e.g., Benz and Vidale 1993). Within these regions, there is at least one unusual effect, and potentially two. First, the compressibility parameter χ becomes very large, so that the terms in $\mathbf{A}_1$ and $\mathbf{A}_2$ that are elsewhere relatively small corrections become much greater than the terms in $\mathbf{A}_0$. Second, within a region undergoing a phase change, the effective viscosity may be dramatically decreased, a phenomenon know as "transformational superplasticity" (e.g., Sammis and Dein 1974; Paterson 1983; Ranalli 1991). In this case, A_{24} could become very large. While we could, in principal, continue to propagate our solution through this region in the usual way, it would be necessary to subdivide the thickness Δz of the phase change region (~ 1 km) into many even thinner layers. This procedure would lead to very time-consuming calculations. We choose instead to evaluate the system of equations (12) in the limits that the density jump is constant, but $\Delta z/z$ approaches zero, and that the effective viscosity of the region, η_z^*, also approaches zero. Our approach is similar to that Corrieu *et al.* (1995), who considered only the effects of large χ through the phase-change region. But if η_z^* becomes small enough, however, the $1/\eta_z^*$ term in **A** could become comparable to or larger than the terms that involve χ, and the product $\eta^*\chi$ could become negligible. In this limit, there is a jump condition on **u** given by

$$\mathbf{u}\Big|_{z-}^{z+} = \left[u_1\Big|_{z-}^{z+} \quad u_2\Big|_{z-}^{z+} \quad \left\{ -4\eta_z^* u_1\Big|_{z-}^{z+} - \Delta\rho^z z V_1^z \right\} \quad 2\Lambda\eta_z^* u_1\Big|_{z-}^{z+} \quad 0 \quad 0 \right]^{\mathrm{T}}, \tag{II-40}$$

where $u_2\Big|_{z-}^{z+} = \dfrac{u_4^z}{\eta_z^*}\dfrac{\Delta z}{z}$; $u_1\Big|_{z-}^{z+} = \dfrac{\Delta\rho^z}{\rho^{z-}} u_1^{z+}$; and η_z^* is the normalized viscosity of the region undergoing the phase change.

The jump in u_1 results directly from continuity of mass flux across the boundary (e.g., Forte and Peltier, 1991a). The jump in u_2 results from the interaction of a finite shear stress on a material with a (potentially) very small effective viscosity. There are also jumps in radial stress (u_3) and tangential stress (u_4), first pointed out by Corrieu *et al.* (1995). The latter jump occurs because the normalized hoop stresses, $\tau_{\theta\theta}$ and $\tau_{\varphi\varphi}$, are required to enforce the change in shape that occurs as an element of mantle traverses the phase-change region, changing its volume without changing its angular width (Hager and Panasyuk 1994). These are proportional to $\eta^*\chi$. As the thickness of the phase-change region decreases, χ increases, such that the product of hoop stresses times layer thickness remains constant. It is interesting that the shear traction does not vanish, despite the effective viscosity becoming very small, so long as $\eta_z^*\chi$ remains finite.

These "jump" conditions are calculated assuming that the phase boundary is at a constant radius. In addition, we might wish to apply a model of topography δz, for example from seismology (Shearer and Masters 1992) or from consideration of thermodynamics (Dehant and Wahr, 1991). In this case, the jump in **u** at the boundary becomes

$$\mathbf{u}\Big|_{z-}^{z+} = \left[u_1\Big|_{z-}^{z+} \quad u_2\Big|_{z-}^{z+} \quad \left\{ -4\eta_z^* u_1\Big|_{z-}^{z+} + z\Delta\rho^z g^z \left(\delta z - \frac{V_1^z}{g^z} \right) \right\} \quad 2\Lambda\eta_z^* u_1\Big|_{z-}^{z+} \quad 0 \quad -4\pi\gamma\Delta\rho^z z^2 \delta z \right]^{\mathrm{T}}.$$

(II-41)

KERNELS CALCULATED USING VARIOUS ASSUMPTIONS

At the OMB and the CMB, shear tractions vanish, so $u_4 = 0$. Combining the internal and external boundary conditions with the matrixant approach (including the effects of phase changes) leads to the system of equations

$$\begin{bmatrix} 0 \\ u_2^{c+} \\ \Delta\rho^c c g^c \left(\delta c - V_1^c / g^c \right) \\ 0 \\ V_1^c \bar{\rho} c \Lambda \\ \left(G_0 V_1^c / c - 4\pi\gamma\Delta\rho^c \delta c \right) \bar{\rho} c^2 \end{bmatrix} = \mathbf{P}_a^c \cdot \begin{bmatrix} 0 \\ u_2^{a-} \\ -\Delta\rho^a a g^a \left(\delta a - G_1 V_1^e / g^a \right) \\ 0 \\ G_1 V_1^e \bar{\rho} a \Lambda \\ \left(G_2 V_1^e / a + 4\pi\gamma\Delta\rho^a \delta a \right) \bar{\rho} a^2 \end{bmatrix} + \mathbf{d}(r_J), \qquad \text{(II-42)}$$

which can be solved with respect to the new vector

$$\mathbf{w} = \left[u_2^{a-} \quad u_2^{c+} \quad \delta a \quad \delta c \quad V_1^e \quad V_1^c \right]^{\mathrm{T}} \qquad \text{(II-43)}$$

to obtain tangential flow velocities, total boundary deflections, and potential anomalies.

The solution depends on the normalized viscosity $\eta^*(r)$ (including the viscosity assumed for the phase change region, η_z^*), on the density structure, $\rho_0(r)$, and on the radii e, a, and c that enter into the propagators. It depends on the gravitational acceleration, $g(r)$, that enters in the source term and boundary conditions. It also depends on the values of the density contrasts $\Delta\rho^e$, $\Delta\rho^a$, and $\Delta\rho^c$ that enter into the boundary conditions. Note that the mass anomaly resulting from the *dynamic* topography ($\delta c - V_1^c / g^c$ or $\delta a - V_1^a / g^a$) is independent of the density contrast at a surface – increasing this density contrast results in a proportional decrease in the dynamic topography, keeping the net mass anomaly from dynamic topography, as well as the gravity anomaly from this mass anomaly constant. However, the mass anomaly associated with the *total* topography (δc or δa), which includes the effects of self-gravitational attraction of deformed boundaries, does depend on the density contrast at each boundary. Hence the effects of self-gravitation enter only indirectly, through the u_6 term.

Table 2: Parameters Used in the Models

Model	1u, 1j	2u, 2j	3u, 3j	4u, 4j	5j	6j	7j	8j	9j	10j	11j	12j
$g(r)$	P	C	10	P	P	P	P	P	P	P	P	P
$\Delta\rho^e, \frac{Mg}{m^3}$	0.00	0.00	0.00	0.00	0.00	0.00	0.00	0.00	0.00	0.00	1.02	1.02
$\Delta\rho^a, \frac{Mg}{m^3}$	4.45	4.45	4.45	3.38	3.38	3.38	3.38	3.38	3.38	3.38	2.36	2.36
$\Delta\rho^c, \frac{Mg}{m^3}$	5.45	5.45	5.45	4.34	4.34	4.34	4.34	4.34	4.34	4.34	4.34	4.34
χ	0	0	0	0	P	P	P	P	P	P	P	P
η^*_z					aver	1/20	1/100	1/20	1/20	1/20	1/20	1/20
outer core	I	I	I	I	I	I	I	P	P	P	P	P
inner core	I	I	I	I	I	I	I	P	I	P	P	P
$\Delta\rho^{ICB}$	0	0	0	0	0	0	0	P	P	0	P	P

Compressibility enters the system of equations governing flow (12), in three fundamentally different ways. First, through its effect on the flow field – in order to conserve flux, flow velocities decrease as the density increases with depth. This effect of compressibility on the flow field is given by $\mathbf{A}_1$. Second, there is the less direct effect of compressibility on the stress due to self-gravitation, given by the single non-zero term in $\mathbf{A}_2$ linking the flow variables and the potential variables. This term provides a correction to the density field to account for the warping of surfaces of constant density to conform to equipotential surfaces. Finally, there is the indirect effect of compressibility on gravitational acceleration $g(r)$. Since $g(r)$ enters both in the body force terms **b**, eq. (13), and in the relation between stress and dynamic topography, eq. (23) and eq. (41), variations in *g(r)* are important (Panasyuk *et al.* 1993). In the following section we investigate these effects separately to gain insight into the physics of compressible flow in a self-gravitating planet. We start with the incompressible Earth model used initially by Richards and Hager (1984), adding complications sequentially, until we end up with a "realistic" model based on the PREM $\rho_0(r)$ (Fig. 1a). The parameters that are varied in these models are identified in Table 2.

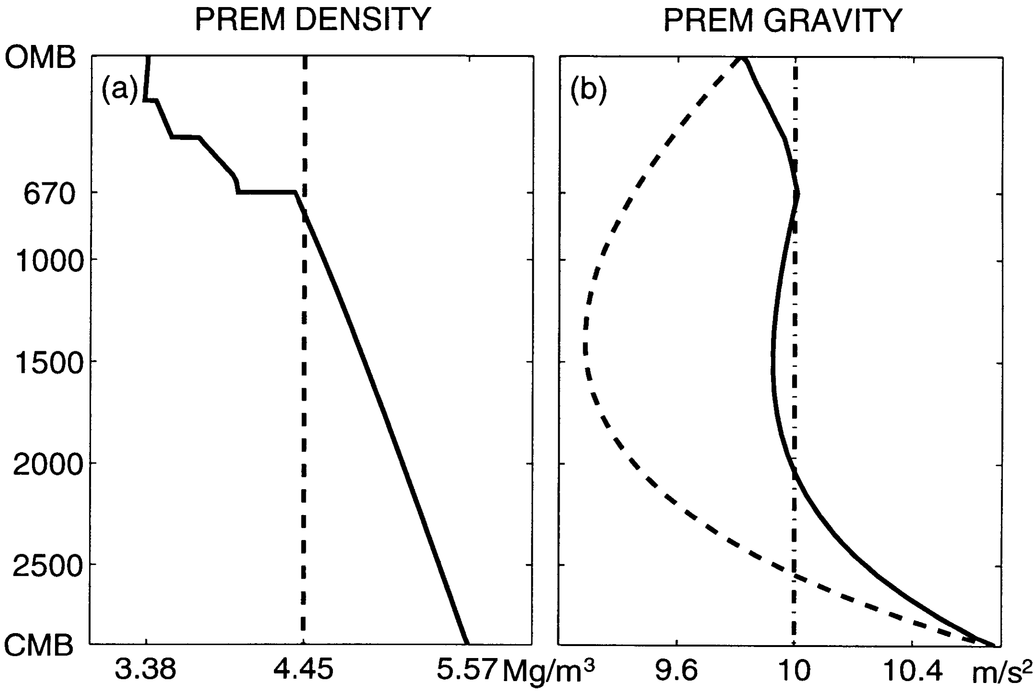

Figure II-1. (a) Density as a function of depth for our modified PREM mantle model (solid) and our incompressible model (dashed). (b) Three choices of *g(r)* used to calculate geoid kernels. The solid line is for the PREM $\rho_0(r)$. The dashed line is calculated in a consistent way for the incompressible mantle ρ_0=4.45 Mg m^{-3}, while the dot-dashed line is for a constant value of 10 m s^{-2}.

The effects of *g(r)*

For the Earth, *g(r)* is determined uniquely by the actual $\rho_0(r)$. For a model planet, however, the choice of *g(r)* is arbitrary, and different modelers have chosen different values. [There is no requirement that *g(r)* be consistent with the density assumed for the "fluid" mantle. For example, in laboratory convection experiments, it is common to embed fine wires attached to thermocouples in the convecting fluid. This mesh of wires has negligible effect on the flow. One could similarly conceive of a fine mesh of dense wires in a self-gravitating fluid sphere that does not participate in the flow, but that does affect $g(r)$.] In the earlier work assuming incompressible flow, it was common to choose $g(r)$ (dashed lines in Fig. 1) consistent with a given mass of the core and a constant $\rho_0(r)$ in the mantle (e.g., Richards and Hager 1984; Ricard *et al.* 1984; Hager and Richards 1989; Corrieu *et al.* 1995). For such a model (Fig. 1b), $g(r)$ has a maximum of 10.6 m s^{-2} at the CMB, falls to 9.4 m s^{-2} at mid-mantle depths, then rises to 9.8 m s^{-2} at the OMB. Forte and Peltier (1987; 1991a) and Thoroval *et al.* (1994) chose, for simplicity, a constant $g(r) = 10$ m s^{-2} , close to the radially averaged value for PREM, while Corrieu *et al.* (1995) chose $g(r)$ consistent with the PREM $\rho_0(r)$ (solid lines in Fig. 1) for their compressible flow model. For this choice, $g(r)$ has a maximum of 10.6 m s^{-2} at the CMB and a minimum of 9.8 m s^{-2} at the surface, but has a value near m s^{-2} 10 throughout most of the mid-mantle.

To isolate the effects of $g(r)$ on the geoid kernels, we plot (Fig. 2a) kernels at spherical harmonic degrees 2 and 5 for an incompressible mantle with uniform viscosity for these three choices of $g(r)$. Model 1u (solid line) uses the PREM value of gravity; Model 2u (dashed) uses a "self-consistent" $g(r)$, while Model 3u (dot-dashed) uses a constant value of 10 m s^{-2}. (Here, "u" denotes uniform viscosity.) These kernels behave as might be expected from the different assumptions for $g(r)$.

For example, the kernels for the "self-consistent" $g(r)$ are always more positive than the kernels for the PREM $g(r)$. The geoid anomaly produced by a density anomaly at a given depth in the mantle depends both on the mass anomaly itself, and on the mass anomaly resulting from the dynamic topography induced by the mantle flow, which has the opposite sign. For an isoviscous mantle, the negative mass anomaly from the dynamic topography dominates, and the total geoid anomaly is negative. Because the self-consistent $g(r)$ is consistently less than that for PREM, for a given internal mass anomaly, there is a smaller body force driving flow and hence less dynamic topography for the same mass anomaly. Less dynamic topography leads to a less negative geoid anomaly, regardless of harmonic degree.

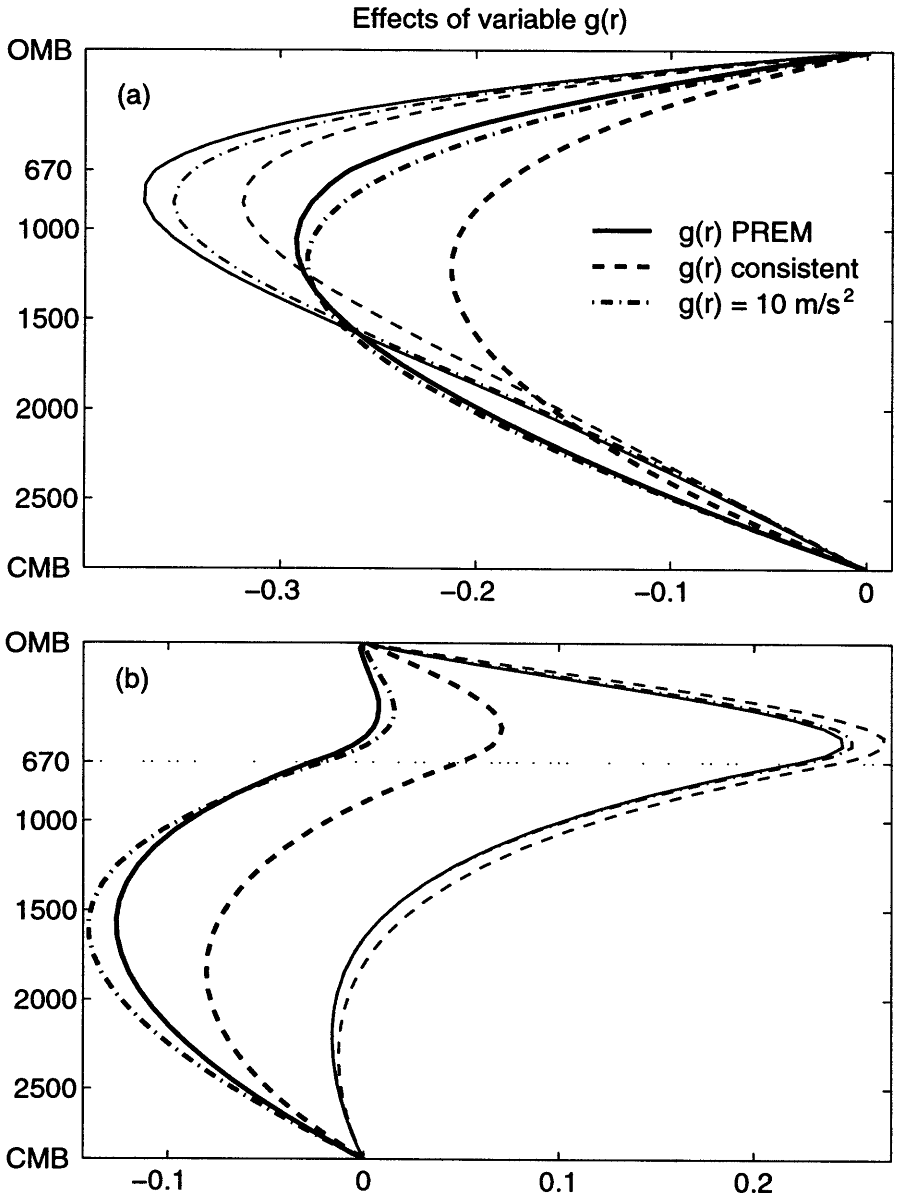

Figure II-2. Geoid kernels at spherical harmonic degrees 2 (heavy line) and 5 (light line) for an incompressible mantle. Kernels for models with a uniform viscosity are shown in (a), while kernels for models with a viscosity jump by a factor of 20 at 670 km depth are shown in (b). Kernels are shown for the three choices of *g(r)* plotted in Fig. 1(b). The "consistent" *g(r)* (dashed line, Models 2u, 2j) is that calculated assuming a constant mantle density of 4.45 Mg m^{-3}. The "constant" model (dot-dashed line, Models 3u, 3j) has a constant value of $g(r) = 10$ m s^{-2}, while the "PREM" *g(r)* (solid line, Models 1u and 1j) is calculated from the $\rho_0(r)$ given by the PREM model.

The kernels for the "constant" *g(r)*, which are close to those for the PREM *g(r)*, illustrate the effects of different *g* at the boundaries. For example, in the vicinity of 670 km depth the PREM *g(r)* and the constant *g(r)* are approximately equal, so the body forces and viscous stresses are comparable in both models. The models, however, have different surface gravity; the larger *g(r)* at the surface for the "constant-*g*" model results in less dynamic topography for the same flow stress. Less dynamic topography results in less negative geoid kernels. The effect of different gravity at the CMB can be seen for the kernels at degree 2. For example, the body forces and viscous stresses are comparable in the two models for density contrasts at a depth of about 2000 km. The kernel for constant *g(r)* is more negative than for PREM *g(r)* at this depth because the former model has smaller *g* at the CMB, and hence more dynamic topography for the same stress. At degree 5, however, the influence of the CMB is severely attenuated. In this case, the kernel for constant *g* is more positive than that for PREM *g* because only the effects of deformation of the OMB are important, and *g* at the OMB is higher for the former model.

All mantle viscosity models proposed to match the geoid have at least a moderate viscosity increase between the upper and lower mantles. To show the effects of varying *g(r)* for a more "realistic" viscosity model, we plot the kernels for simple two-layer models with a viscosity jump of a factor of 20 at 670 km depth (Fig. 2b). Although all kernels are shifted to the right as the result of a viscosity increase with depth, the differences among the kernels for different assumptions of *g(r)* are similar to those for an isoviscous model. For example, the kernels for the consistent *g(r)* (Model 2j; "j" denotes viscosity jump) are always more positive than the others, for the same reason. At degree 2, Model 3j, with constant *g(r)*, still has more positive kernels in the upper mantle, and more negative kernels in the lower mantle, than does Model 1j, with PREM *g(r)*, but the crossover of the kernels occurs at a different depth because the increase in viscosity with depth makes the effects of CMB topography more important than for a mantle with uniform viscosity. Again, at degree 5, the effects of CMB topography are negligible, and the effects of different values of *g* at the surface dominate.

Density contrasts at the OMB and the CMB

The values assumed for density contrasts at the OMB and CMB are important because of the effects of self-gravitation on the total topography and mass anomalies at these interfaces. Given the same flow stresses acting on the OMB (or CMB), larger density contrasts there do not change the mass anomaly due to the dynamic (flow induced) topography, but do increase the mass anomaly associated with the geoid undulations, therefore acting to amplify the geoid anomalies at these boundaries. In Fig. 3(a) we show kernels for incompressible Model 4u (solid line), which has the modified PREM values for $\Delta\rho^c$=4.34 Mg m^{-3} and $\Delta\rho^a$=3.38 Mg m^{-3} (without a crust or ocean), along with kernels for Model 1u (dashed line), which has self-consistent values for density contrasts, $\Delta\rho^c$=5.45 Mg m^{-3} and $\Delta\rho^a$=4.45 Mg m^{-3}. [For these and all subsequent models, we assume the PREM $g(r)$.] For an isoviscous mantle, the geoids at both the OMB and the CMB are negative for all degrees. Since Model 1 has larger density contrasts across these boundaries, the self-gravitation of these boundaries amplifies the geoid anomalies considerably. The effect is largest at degree 2, as would be expected for a process that results solely from self-gravitation, but is still substantial at degree 5.

The kernels for Model 4j, with a viscosity jump at 670 km depth, are positive near the top of the mantle and negative near the bottom of the mantle. At degree 5, the larger density contrast at the OMB in Model 1j behaves as expected, amplifying the geoid kernels. At degree 2, however, the effects are more subtle. For this model, the dynamic topography and the geoid at the CMB are negative, even for density contrasts in the upper mantle. The self-gravitational amplification of the topography at the CMB gives a negative contribution to the geoid at the surface from the deformation of the CMB. This effect is larger for the larger density contrast at the CMB in Model 1j. The additional negative contribution from the CMB more than compensates for the slight amplification of the relatively small positive geoid anomaly at the surface due to the larger density contrast at the OMB, so the net effect is a slightly more negative kernel.

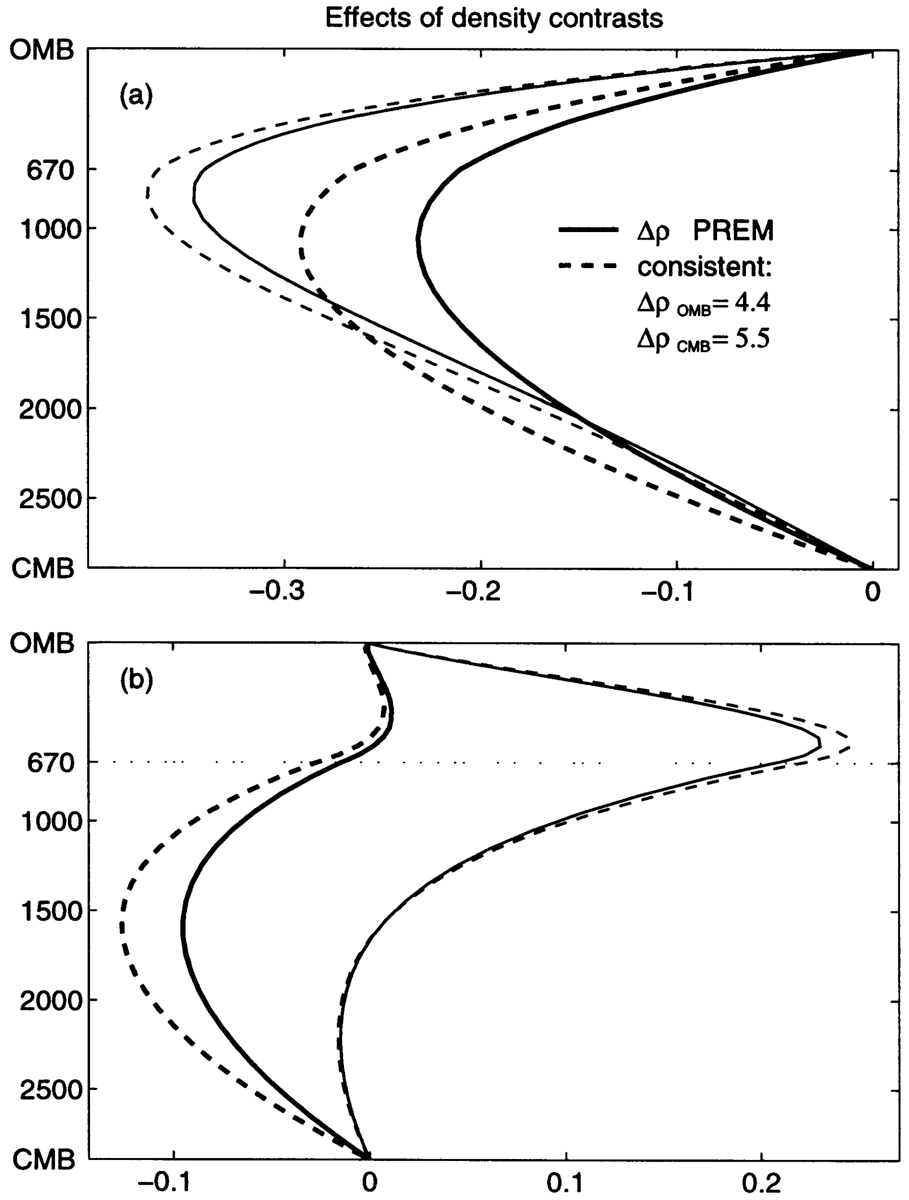

Figure II-3. Geoid kernels at spherical harmonic degrees 2 (heavy line) and 5 (light line) are for incompressible mantle Model 4 (solid), which has the same density contrast at the CMB as PREM (4.34 Mg m^{-3}), and a density contrast at the OMB of 3.38 Mg m^{-3}. For comparison, kernels for Model 1 (dashed), with respective density contrasts of 5.45 and 4.45 Mg m^{-3}, are also plotted. The PREM *g(r)* is used. Kernels are shown for an isoviscous mantle [(a), Models 1u, 4u] and for a model with a jump in viscosity by a factor of 20 at 670 km depth [(b), Models 1j, 4j].

Compressible flow

The next level of complication is to include the effects of compressibility on mantle flow. In Fig. 4 we show kernels for two models with the same density contrasts (based on PREM) and viscosity profile (jump by a factor of 20 at 670 km depth). Model 5j (solid) has the PREM compressibility structure, while Model 4j (dashed) is the incompressible model discussed above. In both models, we assume no ocean, an incompressible core, and that no softening occurs, so $\eta_z^* = (\eta_{z-}^* + \eta_{z+}^*)/2$, when evaluating the jump conditions across the density discontinuities representing phase boundaries.

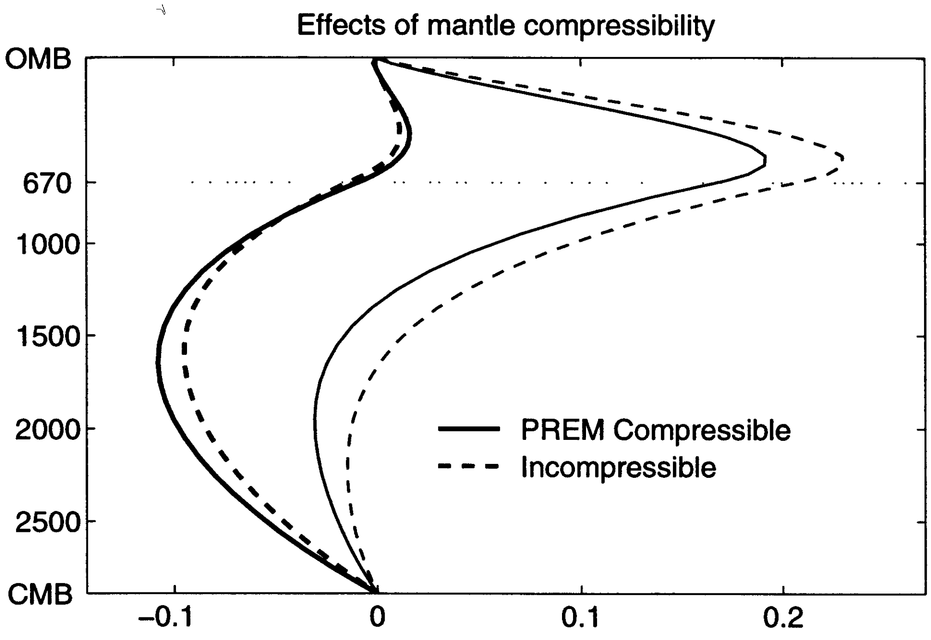

Figure II-4. Geoid kernels at spherical harmonic degrees 2 (heavy line) and 5 (light line) for a model with a viscosity jump at 670 km depth by a factor of 20, assuming the "PREM" $g(r)$ and PREM density contrasts. Kernels are shown for a compressible model with the $\rho_0(r)$ given by the PREM (Model 5j, solid) and for an incompressible model with constant $\rho_0(r)$ (Model 4j, dashed).

For a compressible mantle, to maintain constant mass flux, flow has slower velocities at depth and faster ones at the surface than for an incompressible mantle. Slower/faster flow velocities result in lower/higher viscous stresses, leading to a decrease/increase in the dynamic topography at the CMB/OMB. Correspondingly, surface geoid anomalies for higher harmonics are more affected by changes of OMB topography, leading to a shift to the left of the kernels. This expectation holds at degree 5. On the other hand, lower harmonics are sensitive to changes at the CMB as well, and show a more complicated response, depending on the specific density and viscosity structure. For example, at degree 2, the rapid variation of density with depth within the transition zone in the PREM model, coupled with the jump in viscosity at 670 km depth, leads to slightly more positive kernels in the upper mantle. Unlike the effects of self-gravitation shown by Figs 2 and 3, the direct effects of compressibility on the kernels are larger at degree 5 than at degree 2. We might expect the kernels for a compressible model to resemble those of an incompressible model with a decrease in viscosity with depth. Since the normal stress has coupled dependence on viscosity as well as on the radial velocity gradient, $\tau_{rr} = -p + 2\eta\,\partial v_r/\partial r$, a reduction in lower mantle viscosity leads to higher flow velocities everywhere, but being coupled with smaller viscosity at depth results in lower stress/topography at the CMB.

Transformational superplasticity

Sammis and Dein (1974) first pointed out that mantle convection might be affected by extreme softening of material as it undergoes a phase transition – a general phenomenon known as "transformational superplasticity." A number of microphysical processes have been proposed (e.g., Sammis and Dein 1974; Paterson 1983; Poirier 1985; Ranalli and Schloessin 1989; Ranalli 1991; Hager and Panasyuk 1994). While it is generally agreed that transformational superplasticity leads to a dramatic reduction in effective viscosity, neither the mechanism, nor the magnitude of this effect is well constrained.

We can evaluate the impact of transformational superplasticity on geoid kernels by comparing kernels for models based on different assumptions about the viscosity of the ~ 1 km thick phase-change regions. We show geoid kernels of three models (Fig. 5), from the case in which no softening occurs, $\eta_z^* = \eta_z^{*\mathrm{aver}} = \left(\eta_{z-}^* + \eta_{z+}^*\right)/2 = 10.5$ (Model 5j, dot-dashed line), to the proposed $\eta_z^* = 1/20$ (Model 6j, solid line), and for an even more significant reduction in viscosity $\eta_z^* = 1/100$ (Model 7j, dashed line). The overall effect of two thin regions of reduced viscosity on the flow and the geoid is subtle and depends on wavelength as well as on the particular background viscosity and density profiles. To show two possible situations, we plot kernels for harmonics l=2 and l=12 on Fig. 5 (harmonic l=5 shows the same changes as l=2, but with slightly smaller amplitudes).

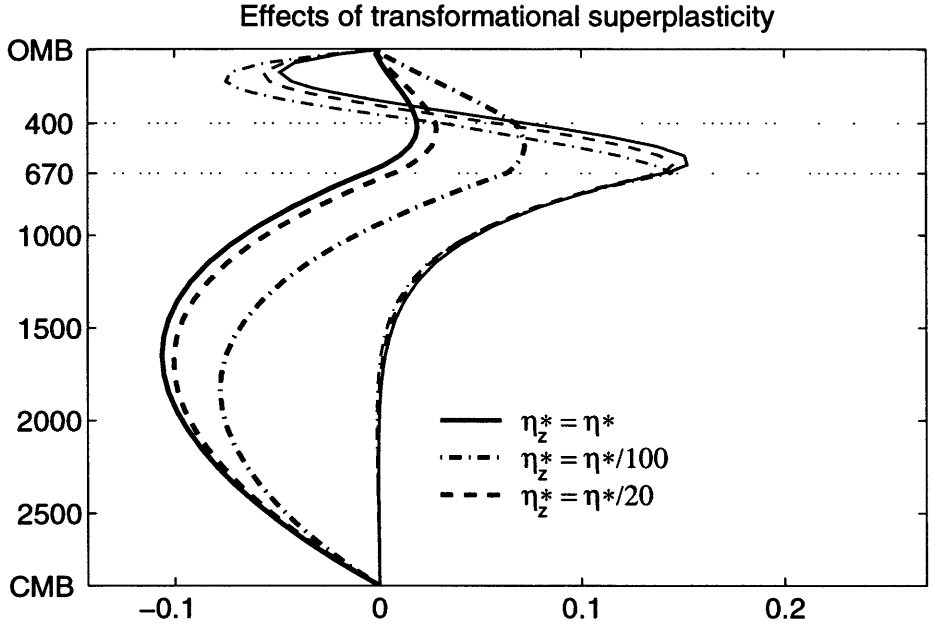

Figure II-5. Geoid kernels at spherical harmonic degrees 2 (heavy line) and 12 (light line) for models with different assumptions about the viscosity used in evaluating the jump conditions at the density discontinuities at 220, 400, and 670 km depth in the PREM model. $\eta_z^* = \eta_z^{*aver} = 10.5$ (Model 5j, solid line), $\eta_z^* = 1/20$ (Model 6j, dashed line), $\eta_z^* = 1/100$ (Model 7j, dot-dashed line).

In general, the presence of thin low-viscosity layers in the upper mantle facilitates the turning of the flow in the vicinity of the OMB. The ability of the flow to turn more easily as it approaches the OMB leads to reduced stress/topography there. The geoid kernels shift to the right due to the weaker gravitational compensation of interior density anomalies by deflection of the OMB (compare heavy dash and dash-dotted lines with the solid one in Fig. 5). If the centre of a convecting cell is above the low viscosity layer for short wavelength sources (e.g. l=12) the situation reverses: there is less dynamic support from below and larger dynamic topography at the OMB. Correspondingly, the geoid kernels shift to the left (compare the heavy dash and dash-dotted lines with the solid one in Fig. 5). Intermediate-wavelength sources induce a flow which experiences a trade-off between these two situations, depending on the density and viscosity profiles of the mantle. Given our simplified 2-layered viscosity structure (jump by 20 at 670 km depth), PREM density profiles, and two softened phase regions in upper mantle (at 400 and 670 km), geoid kernels of l=2 shift to more positive values (see Fig. 5) and l=12 kernels shift to more negative values. The effect of a reduction in effective viscosity by a factor of 100 in 1 km thick zones at 400 and 670 km depth is comparable to the effect of increasing the viscosity of the lower layer by 40 per cent (compare Figs 5 and 7 and see later discussion).

Outer and inner core

To evaluate the effect of compressibility of the outer and inner cores, in Fig. 6, we compare kernels for Model 8j (solid line) calculated assuming the PREM compressibility of the core and PREM density jump at the ICB with those for Model 6j (dashed line) calculated assuming that the core is incompressible, with uniform density.

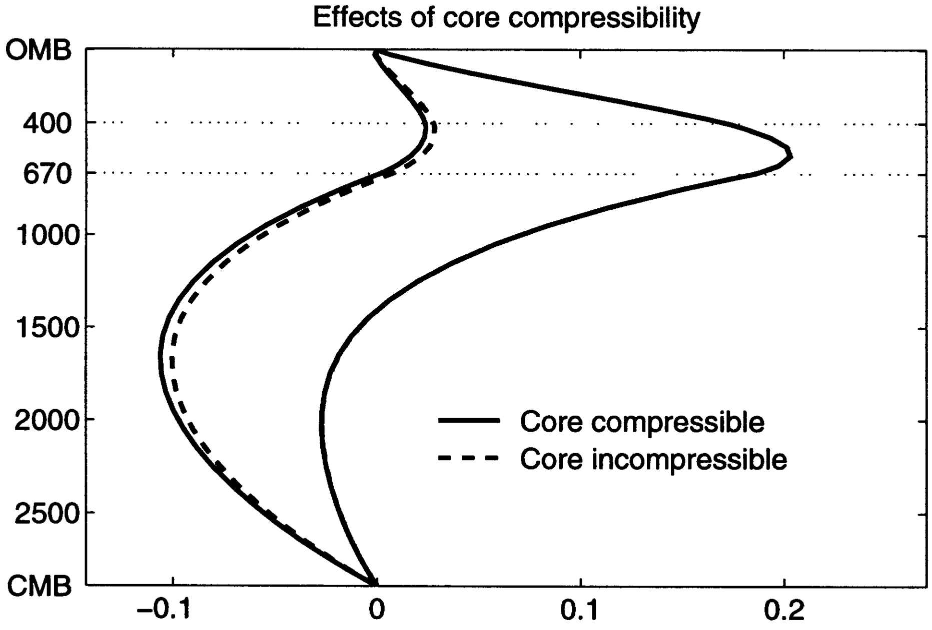

Figure II-6. Geoid kernels at spherical harmonic degrees 2 (left) and 5 (right) for models with different assumptions about the compressibility of the core. Model 8j (solid line) has the PREM compressibility structure in the core, while Model 6j (dashed) has an incompressible core.

The effects of including compressibility of the core are quite similar to the effects of increasing the density contrast at the CMB (Model 4j, Fig. 3b). The self-gravitational amplification of the negative geoid anomaly at the CMB shifts the kernels for degree 2 to slightly more negative values. Because of the rapid attenuation of the effects of the CMB with increasing harmonic degree, there is no resolvable effect of the density structure of the core at degree 5. To investigate the effects of compressibility of the inner core, we calculated kernels for Model 9j, which has an incompressible inner core. To investigate the effects of the assumed density jump at the ICB, we calculated kernels for Model 10j, in which we set the density contrast at the ICB to zero. Kernels for these two models overlay those for Model 8j – the gravitational effects of the inner core are essentially invisible in the geoid kernels.

Ocean

In Model 11j, we add the total effect of an ocean by using the density of sea water for the density contrast at the SUR and decreasing the density contrast at the OMB by the same amount. The kernels overlay the kernels for Model 8j in Fig. 6. The reason for this small contribution of the ocean to geoid undulations on the surface becomes clear when we treat the total topography as the sum of the dynamic topography and the geoid anomaly. The mass anomaly associated with the former is independent of the density contrast at the OMB – the reduction in density contrast associated with adding an ocean layer is exactly counterbalanced by an increase in dynamic topography. The geoid anomaly includes the self-gravitational interaction of mass anomalies at all boundaries, including both the OMB and SUR. Adding an ocean layer increases the density contrast at boundary SUR by exactly the same amount as it decreases the density contrast at the OMB. Because the thickness of the ocean is negligible compared to the radius of the Earth, the equipotential surfaces at OMB and SUR are essentially parallel. Thus the total mass anomaly from self-gravitational interaction of these surfaces is almost identical for the cases with and without an ocean. These arguments are still correct locally for a planet such as Earth that is partially dry and partially covered with an ocean, so long as the effects of an elastic lithosphere are negligible at the wavelengths where self-gravitation is important.

Finally, to place the effects of compressibility in perspective, we also show (Fig. 7) the effects of increasing the viscosity jump of the lower mantle by 40 per cent, to a factor of 28 (Model 12j). The changes are rather large, and comparable in magnitude and form to those caused by differing assumptions of *g(r)* (Model 2j, Fig. 2b), and to those caused by a 1/100 reduction in viscosity of the phase-change regions (Model 7j, Fig. 5). So there is a trade-off between mantle viscosity structure, the effects of compressibility (see also Forte, Woodward and Dziewonski 1994; Corrieu *et al.* 1995), and transformational superplasticity at phase-change zones.

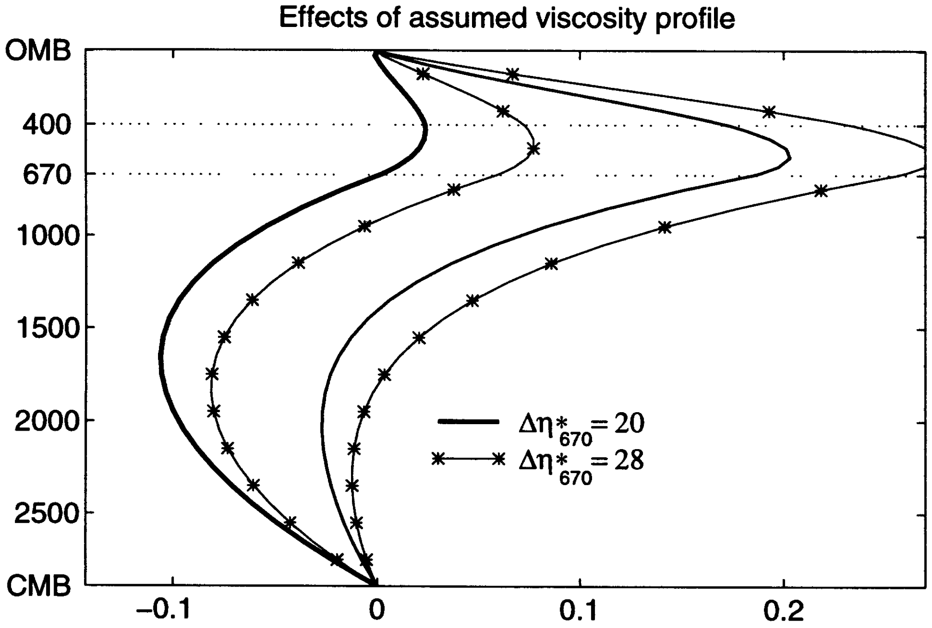

Figure II-7. Geoid kernels at spherical harmonic degrees 2 (heavy line) and 5 (light line) for models with different values of lower mantle viscosity. Model 11j (solid) has a viscosity jump by a factor of 20; Model 12j (stars) has a viscosity jump by a factor of 28 at 670 km depth.

In order to quantify the relative importance of all the effects described, we calculate the absolute difference between geoid kernels for a model which considers a particular effect and one which does not, and show it on the a plot in two perspectives: one shows the differences in geoid as a function of depth of the source for the most sensitive harmonic, *l*=2 (Fig. 8a), and the other shows the changes in geoid from a single upper mantle density source as a function of order of spherical harmonic, l=2-15, of this load. To clarify the significance of one effect versus another, we use a logarithmic scale for the absolute differences in geoid. The sharp features of reduced amplitude on both Figs 8(a) and (b) are due to zero cross-overs.

For example, to illustrate the effects of constant $g(r)$ and consistent $g(r)$ versus realistic $g(r)$, we difference models 3j with 1j, and 2j with 1j (dotted lines in Figs 8a and b); to show the effects of choices for the density contrasts at the OMB/CMB and at the ICB, we difference models 4j with 1j, and 10j with 8j (dot-dashed lines, heavy and light respectively). The effects of compressibility of the mantle (models 5j with 4j), core (models 8j with 6j) and inner core (models 8j with 9j) are displayed by solid lines, those of superplastic softening (models 6j and 7j with 5j) with dashed lines, and those of the ocean (models 8j with 11j) with circles. Finally, to put all effects in perspective relative to changes in effective viscosity of the lower mantle, we plot the difference between our reference model (11j) and one which has a 40 per cent increase in lower mantle viscosity, model 12j (crossed line).

The largest differences in geoid kernels for our different models at degree 2 (Fig. 8a) come from different assumptions for the gravitational acceleration $g(r)$ (dotted line) and from the introduction of a significant (1/100) softening of the phase-change region (dashed line). These reach a value of almost 10^{-1}, which, for the model with a viscosity jump by a factor of 20 at 670 km depth, can change the kernels by nearly 50 per cent. The maximum differences caused by different assumptions about the density contrasts at the SUR and the CMB (dash-dotted line) are about a factor of 2 smaller, but still important.

The effects of compressibility of the mantle *senso stricto* and of moderate transformational superplasticity (viscosity reduced by 1/20) are third in importance at degree 2 (thick solid and dashed lines). The effects of compressibility of the outer core (thin solid line), important only at degree 2, are small, but noticeable.

The effects of a "realistic" treatment of the inner core are negligible. So are the total effects of the ocean. Earlier studies that chose not to discuss the effects of the ocean (e.g., Richards and Hager 1984; Ricard *et al.* 1984) were justified in their neglect of the ocean layer on geoid kernels.

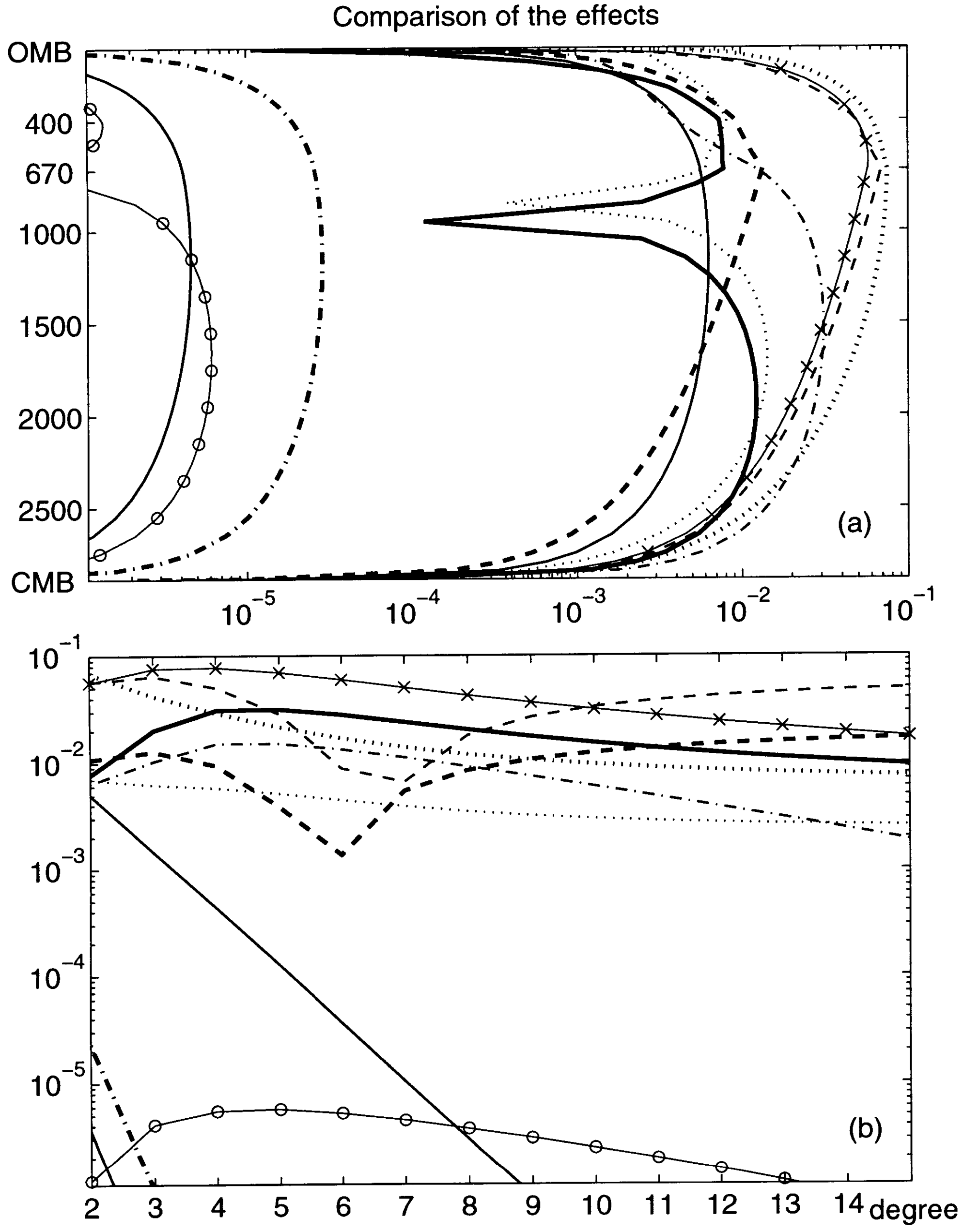

Figure II-8. Summary. Logarithm of the absolute value of the difference between the kernels at degree 2 (a) and between the surface geoid from an upper mantle source (at 525 km depth) for different l=2-15 (b). The crossed solid line is for a jump in mantle viscosity by a factor of 28 at 670 km depth. The dotted heavy and light lines are for the "consistent" (thick line) and "constant" $g(r)$. The dashed heavy and light lines are for the moderate transformational superplasticity (1/20 reduction in viscosity) and for significant (1/100) softening of the phase-change regions. The light dash-dot line shows the effects of density jumps at the OMB and the CMB, while the heavy dash-dot line shows the effect of the density jump at the ICB. The heavy solid line is for mantle compressibility; the light solid lines are for outer and inner core compressibility (the latter has much smaller amplitude). The light O line is for the ocean.

The relative significance of these effects changes as a function of wavelength, as is shown on Fig. 8b for a source located at 525 km depth. For intermediate wavelengths (l=4-8), the dominant effects are a significant reduction in the phase-change-region viscosity and mantle compressibility, following by the choice of *g(r)*, density contrasts at boundaries, and transformational superplasticity. For short wavelengths (l=9-15), the dominant effects are softening of the phase-change regions, following by the mantle compressibility, and then by the choice of *g(r)*. The different assumptions about the core and the presence of the ocean become completely insignificant as the order of the harmonic increases.

For comparison, the effect of increasing the viscosity of the lower mantle by 40 per cent is to change the geoid kernels by an amount comparable to all of the effects of compressibility taken together. Current models of mantle viscosity structure estimated from matching the observed and predicted geoids vary by orders of magnitude. The main reason for this large variation in inferred viscosity structure is that the models of density heterogeneity used differ substantially.

However, although the effects of ignoring compressibility and transformational superplasticity are relatively small compared to the effects of the uncertainties in density heterogeneities driving the flow, we believe that, in the future, these models should use realistic assumptions about the background density structure. Using our quasi-analytical formulation, kernels for compressible flow are not much more difficult to calculate than those for incompressible flow.

Although our attempt to understand quantitatively the effects of compressibility on geoid kernels has been comprehensive, it has not addressed other phenomena that affect the geoid. In particular, we have not addressed in this paper the effects of the lateral variations in effective viscosity that occur within the convecting mantle and at plate boundaries. Just as compressibility contributes both to $\mathbf{A}_l$ and $\mathbf{b}_l$ in eq. (12), lateral variations in viscosity also contribute, both to $\mathbf{A}_l$ and to $\mathbf{b}_l$ (e.g., Richards and Hager 1989; Zhang and Christensen 1993; Forte and Peltier 1994). For lateral variations in interior viscosity of the magnitude of those models inferred using seismic tomography, these changes are small enough that general inferences from geoid models, such as a moderate increase in viscosity with depth, are robust (e.g., Richards and Hager 1989;

Forte and Peltier 1994). As we have seen in our analysis of the effects of compressibility, however, relatively small changes in $\mathbf{A}_l$ and $\mathbf{b}_l$ can lead to quantitative differences in geoid kernels comparable to those resulting from moderate changes in the radial viscosity structure. Furthermore, studies that have treated plate boundaries as low viscosity regions have demonstrated that weak plate boundaries can result in changes in the long-wavelength geoid of tens of per cent or more (e.g., Ribe 1992; Zhang and Christensen 1993; King and Hager, 1994), even changing the sign of the geoid (Simons, 1995). A quantitative study of the effects of lateral variations in viscosity along the lines of our study of the effects of compressibility would be very useful.

ACKNOWLEDGMENTS

We thank Catherine Thoraval, Valerie Corrieu, and Yanick Ricard for preprints of their papers and for useful comparisons of codes. Support for SVP and BHH was supported by NASA grant NAG5-1911. AMF acknowledges support provided by NSF Grants EAR92-19361 and EAR92-05390 (while still at Harvard University) and continued support by the IPGP/CNRS.

REFERENCES

Benz, H. M. and J. E. Vidale, 1993. Sharpness of upper-mantle discontinuities determined from high-frequency reflections, *Nature,* **365,** 147-150.

Corrieu, V., C. Thoraval and Y. Ricard, 1995. Mantle dynamics and geoid Green functions, *Geophys. J. Int.,* **120,** 516-523.

Dehant, V. and J. M. Wahr, 1991. The response of a compressible, non-homogeneous earth to internal loading: theory, *J. Geomag. Geoelectr.,* **43,** 157-178.

Dziewonski, A. M. and D. L. Anderson, 1981. Preliminary reference Earth model, *Phys. Earth Planet. Int.,* **25,** 297-356.

Forte, A. M. and W. R. Peltier, 1987. Plate tectonics and aspherical Earth structure: the importance of poloidal-toroidal coupling, *J. Geophys. Res.,* **92,** 3645-3679.

Forte, A. M. and W. R. Peltier, 1991a. Viscous flow models of global geophysical observables 1. Forward problems, *J. Geophys. Res.,* **96,** 20,131-20,159.

Forte, A. M. and W. R. Peltier, 1991b. Gross earth data and mantle convection: New inferences of mantle viscosity, in *Glacial Isostasy, Sea-Level and Mantle Rheology,* pp. 425-444, Eds. R. Sabadini, K. Lambeck and E. Boschi, Kluwer, Boston.

Forte, A. M. and W. R. Peltier, 1994. The kinematics and dynamics of poloidal-toroidal coupling in mantle flow: The importance of surface plates and lateral viscosity variations, *Adv. Geophys.,* **36,** 1-119.

Forte, A. M., A. Dziewonski and R.L. Woodward, 1993. Aspherical structure of the mantle, tectonic plate motions, nonhydrostatic geoid, and topography of the core-mantle boundary, *Am. Geophys. Union, Geophys. Mon.,* **72,** 135-166.

Forte, A. M., R. L. Woodward and A. M. Dziewonski, 1994. Joint inversions of seismic and geodynamic data for models of three-dimensional mantle heterogeneity, *J. Geophys. Res.,* **99,** 21,857-21,877.

Gantmacher, F. R., 1960. *The theory of matrixes.* Chelsea, New York, NY.

Hager, B. H., 1983. Global isostatic geoid anomalies for plate and boundary layer models of the lithosphere, *Earth Planet. Sci. Lett.,* **63,** 97-109.

Hager, B. H., 1984. Subducted slabs and the geoid: Constraints on mantle rheology and flow, *J. Geophys. Res.,* **89,** 6003-6015.

Hager, B. H. and R. W. Clayton, 1989. Constraints on the structure of mantle convection using seismic observations, flow models, and the geoid, in *Mantle Convection,* pp. 657-763, ed. R. W. Peltier, Gordon and Breach Science Publishers, New York, NY.

Hager, B. H. and R. J. O'Connell, 1981. A simple global model of plate dynamics and mantle convection, *J. Geophys. Res.,* **86,** 4843-4867.

Hager, B. H. and S. V. Panasyuk, 1994. Large deviatoric strain rates from flow through a phase change: implication for the rheology and dynamics of the transition zone, *EOS Trans. Am. Geophys. Un.,* **75,** 641.

Hager, B. H. and M. A. Richards, 1989. Long-wavelength variations in Earth's geoid: physical models and dynamical implications, *Phil. Trans. R. Soc. Lond.,* A, **328,** 309-327.

Hager, B. H., R. W. Clayton, M. A. Richards, R. P. Comer, A. M. Dziewonski, 1985. Lower mantle heterogeneity, dynamic topography and the geoid, *Nature,* **313,** 541-545.

King, S. D. and B. H. Hager, 1994. Subducted slabs and the geoid, 1, Numerical experiments with temperature-dependent viscosity, *J. Geophys. Res.,* **99,** 19 843-19 852.

King, S. D. and G. Masters, 1992. An inversion for radial viscosity structure using seismic tomography, *Geophys. Res. Lett.,* **19,** 1551-1554.

Landau, L. D. and I. M. Lifshitz, 1987. *Fluid mechanics.* Pergamon Press, Oxford.

Munk, W. H. and G. J. F. MacDonald, 1960. *The Rotation of the Earth--A Geophysical Discussion,* Cambridge University Press, Cambridge.

Panasyuk, S. V., A. M. Forte and B. H. Hager, 1993. The effect of the assumed g(r) on geoid kernels for compressible and incompressible mantle flow models, *EOS Trans. Am. Geophys, Un.,* **74,** 558.

Paterson, M. S., 1983. Creep in transforming polycrystalline materials, *Mech. Materials,* **2,** 103-109.

Parsons, B. and S. Daly, 1983. The relationship between surface topography, gravity anomalies, and the temperature structure of convection, *J. Geophys. Res.,* **88,** 1129-1144.

Pekeris, C. L., 1935. Thermal convection in the interior of the Earth, *Mon. Not. R. Astr. Soc., Geophys. Suppl.,* **3,** 343-367.

Poirier, J. P., 1985. *Creep of Crystals,* Cambridge University Press, Cambridge.

Ranalli, G., 1991. The microphysical approach to mantle rheology, in *Glacial isostasy, sea-level and mantle rheology,* pp. 343-378, eds R. Sabadini, K. Lambeck and E. Boschi, Kluwer Academic Publishers, Boston.

Ranalli, G. and H. H. Schloessin, 1989. Role of episodic creep in global mantle deformation, *Am. Geophys. Un., Geophys. Mon.,* **49,** 55-63.

Ribe, N., 1992. The dynamics of thin shell with variable viscosity and the origin of toroidal flow in the mantle, *Geophys. J. Int.,* **110,** 537-552.

Ricard, Y., M. A. Richards, C. Lithgow-Bertelloni and Y. Le Stunff, 1993. A geodynamic model of mantle density heterogeneity, *J. Geophys. Res.,* **98,** 21 895-21 909.

Ricard, Y., L. Fleitout, and C. Froidevaux, 1984. Geoid heights and lithospheric stresses for a dynamic Earth, *Ann. Geophys.,* **2,** 267-286.

Richards, M. A. and B. H. Hager, 1984. Geoid anomalies in a dynamic Earth, *J. Geophys. Res.,* **89,** 5987-6002.

Sammis, C. G. and J. L. Dein, 1974. On the possibility of transformational superplasticity in the Earth's mantle, *J. Geophys. Res.,* **79,** 2961-2965.

Shearer, P. M. and T. G. Masters, 1992. Global mapping of topography on the 660 km discontinuity, *Nature,* **355,** 791-796.

Simons, M., 1995. Localization of geoid and topography: Constraints on the tectonics and mantle dynamics of Earth and Vinus, PhD. thesis, Mass. Inst. of Technol., Cambridge, USA.

Sleep, N. H. and R. J. Phillips, 1979. An isostatic model for the Tharsis Province, Mars, *Geophys. Res. Lett.,* **6,** 803-806.

Thoraval, C. P., P. Machetel and A. Cazenave, 1994. Influence of mantle compressibility and ocean warping on dynamical models of geoid, *Geophys. J. Int.,* **117,** 566-573.

Vening Meinesz, F. A., 1946. The indirect isostatic or Bowie reduction and the equilibrium figure of the earth, *Bull. Geodes.*, **1,** 33-107.

Zhang, S. and U. Christensen, 1993. Some effects of lateral viscosity variations on geoid and surface velocities induced by density anomalies in the mantle, *Geophys. J. Int.*, **114,** 531-547.

Chapter III. A MODEL OF TRANSFORMATIONAL SUPERPLASTICITY IN THE UPPER MANTLE. [2]

ABSTRACT

We develop a model of transformational superplasticity of the mantle as it undergoes a solid-solid phase change. By considering various scenarios of the evolution of grain geometry in a polycrystalline material composed of two phases of different densities, we estimate the strain rate associated with the reshaping of the grains required to accommodate the volume change. We relate the deviatoric strain rate of the reshaping grains to the macroscopic dilatation rate of the entire composite, where the latter is evaluated both by applying a kinetic theory of the transformation and by implementing the seismically-observed sharpness of the phase-transformation. We estimate that, depending on the grain-geometry and the kinetics, the deviatoric strain rates can exceed the dilatational strain rates by an order of magnitude.

We calculate the degree of softening of the mantle which would occur at the beginning of the phase transformations at 400- and 670-km depths. For a power-law rheology with stress exponent n=3, mantle viscosity decreases by up to one to two orders of magnitude within the first 1.5 km of the upper transition, and by two to three orders of magnitude within the first 1 km for the transition at 670-km depth. To account for uncertainties in strain rate (or stress) and grain size, we construct a deformation mechanism map for a three-component mantle and a variety of grain sizes, tectonic stresses, and strain rates. In the dislocation creep regime, the high transformational stresses place an upper bound on the effective viscosity of the composite.

We calculate the transformational-superplasticity (TS) field for a particular mantle flow model and show that variations of effective viscosity on the order of one order of magnitude occur at half of the dominant flow wavelength. We describe the effects of a phase transformation on mantle dynamics as jump conditions on the vertical and the

---

[2] in press in *Geophysical Journal International*, by Panasyuk, S.V., and B.H. Hager, 1998.

lateral velocities across the thin two-phase layer. An abrupt change in the azimuthal velocity would facilitate mixing across the phase-change region and cause refraction of currents passing through this depth. The largest deviation of the flow velocities occurs within the major up- and down-wellings. We also show that when TS is included, the change in the long-wavelength geoid is comparable to that caused by a 50% increase in the viscosity of the lower mantle, and the change in the short-wavelength geoid is similar to an extension of an upper mantle low-viscosity zone down to 450-km depth.

Key words: mantle convection, mantle rheology, mantle viscosity, phase transitions, upper mantle.

INTRODUCTION

That polycrystalline material might deform superplastically during a solid-solid phase change has attracted the attention of materials science. The large elongations in metals and alloys (discovered by Sauveur 1924) and increased creep rate in some ceramics were repeatedly observed and are now commonly recognized as superplastic phenomena (Edington *et al.* 1976; Poirier 1985; Maehara & Langdon 1990; Meike 1993). However, the possibility of superplastic deformation of other non-metallic materials, such as rocks and minerals under geologic conditions, has received less attention. There have been only a few geologic experimental studies of phase transitions, first done by Sammis & Dein (1974), attempting to measure and observe the superplasticity of rocks. Besides direct experimental measurement, the anomalous softening of mantle material might be seen through its effect on the viscous response of mantle rocks. For example, a thin layer of reduced viscosity associated with a phase change is seen in some models of the global geoid (e.g. Forte *et al.* 1993; Panasyuk 1998), of glacial isostatic adjustment (e.g. Milne *et al.* 1997) and of polar motion (Steinberger & O'Connell 1996). The complex bending of subducted slabs depicted by regional seismic tomography (e.g. van der Hilst 1995) might be associated with anomalous weakening during phase transformations. We develop here a model of transformational superplasticity (TS) for the upper mantle and investigate its effect on mantle flow. Before describing our method, we introduce the basis of our model, discuss characteristic features of TS from the experimental studies, and outline the paper content.

Numerous experimental studies show that superplasticity occurs during diffusional (e.g., nucleation and growth type) as well diffusionless (e.g. martesitic type) transformations. Hence, no unique microscopic mechanism exists (Edington *et al.* 1976). Nevertheless, several characteristic features of transformational superplasticity have been reported in experimental studies: 1) strain rate is proportional to applied load, volume change, and heating/cooling rate; 2) a low applied stress, sufficient to cause flow during the transformation, is insufficient to cause the same deformation outside the transformational environment. Based on the second observation, an internal stress generated during the phase change was considered to play an important role in deformation (first by Greenwood & Johnson 1965). An increased strain rate during transformation was associated with a rise of stress which caused an additional flux of dislocations (Kot & Weiss 1970; Poirier 1982) in the low-temperature dislocation creep regime.

In this paper we develop a model of transformational superplasticity (TS) associated with mantle convection through the phase transitions at 400 km and 670 km depth. The key assumption in this model is that, because the pressure at these depths is so high, individual mineral grains are forced to deform in order to maintain the mechanical integrity of the material. The rate of reshaping of the grains is controlled by the rate at which mantle convection moves the material through the phase transition region. Given the geometry of the mineral grains and the rate of volume change, the deviatoric strain rate of an individual mineral grain can be estimated. We can then use the well-known empirical relations between imposed strain rate, stress, and effective viscosity to calculate the reduction in effective viscosity caused by this mechanism.

For a range of plausible grain geometries, the deviatoric strain rate associated with the reshaping of individual mineral grains to maintain geometric compatibility can be an order of magnitude or more larger than the volumetric strain rate. The volumetric strain rate may be much greater than typical strain rates associated with mantle convection. Thus, the grains deform faster than the typical ambient mantle, and it seems likely that the grain reshaping occurs in the power law creep regime. Although the microscopic mechanism by which power law creep occurs is not well understood (e.g. Karato, 1989), for our purposes, the exact mechanism is not important, since the length scales that we consider are those of individual grains, for which the experimental evidence for power-law creep is well established. This macroscopic approach distinguishes our approach from those that focus on a particular, more speculative, microscopic mechanism (e.g. by Paterson, 1983). In the Methodology section we explore the effect of different grain geometries, different types of transformation kinetics, and the presence of an untransforming component in an aggregate. We build a mathematical apparatus to estimate the amplitude of the TS phenomenon.

In the Results section we estimate the degree of softening for mantle material that starts to change phase at 400 km and 670 km depths. For the upper transition we apply kinetic theory for a metastable reaction and estimate the TS magnitude for n=3 power-law rheology, including moderate variations in grain geometry. Constructing a deformation mechanism map (DMM) for a range of possible mantle parameters, we evaluate the degree of softening for linear-to-power law rheologies. Then we estimate the TS for mantle flow across the phase transformation at 670 km depth. Because our model is based on an assumed grain geometry that may or may not be realistic, it is important to investigate how geodynamical observations can be used to test the predictions of the model. We build a model of compressible mantle flow in response to density anomalies (deduced from seismic tomography) and construct a map of the reduced viscosity at 670-km depth. We discuss the characteristic features of the TS-field and how both uniform and laterally varying softening inside the transformation region affect flow velocities, slab trajectories, and the geoid.

METHODOLOGY

Laboratory experiments designed to investigate mantle rheology are often carried out under an externally imposed shear strain rate $\dot{\gamma}$. The relationship between the scalar $\dot{\gamma}$ and the shear stress τ is often written

$$\dot{\gamma} = A\left(\frac{\tau}{\mu}\right)^n \left(\frac{b}{d}\right)^m, \tag{III-1}$$

where μ is the shear modulus, b is the Burgers vector, d is the grain size and A (dimension time^{-1}) is a function of temperature, pressure, composition, oxygen fugacity, grain orientation, and other parameters.

For mantle flow calculations, the state of the deviatoric stress at each point of the media, a tensor σ_{ij}, is related to the deviatoric strain rate tensor $\dot{\varepsilon}_{ij}$ as:

$$\sigma_{ij} = 2\eta_{\text{eff}}\dot{\varepsilon}_{ij}, \tag{III-2}$$

where η_{eff} is the effective viscosity. To link the laboratory description of rheology to the convection description of rheology, the usual assumption is that the scalar strain rate $\dot{\gamma}$ and the scalar shear stress τ in (1) can be related to the second invariant of strain rate and stress tensors respectively, e.g., $\dot{\gamma} = \sqrt{I_2} = \sqrt{\dot{\varepsilon}_{ij}\dot{\varepsilon}_{ij}/2}$. (We use Einstein summation notation unless otherwise specified). To describe the effective viscosity we can use either the stress τ or the strain rate $\dot{\gamma}$:

$$\eta_{\text{eff}} = \frac{\mu}{2A}\left(\frac{d}{b}\right)^m \left(\frac{\mu}{\tau}\right)^{n-1} = \frac{\mu}{2A^{1/n}}\left(\frac{d}{b}\right)^{\frac{m}{n}} \dot{\gamma}^{\frac{1}{n}-1} \tag{III-3}$$

To illustrate how the reshaping of grains associated with a phase change increases the second invariant of the strain rate tensor and hence reduces the effective viscosity, we carry out a thought experiment. Let us consider two nearly identical samples of a material, where the only difference is that one undergoes a phase change and the other is stable. An external, macro-scale strain rate is imposed on both pieces, $\dot{\varepsilon}_{ij}^{\text{mantle}}$ (e.g. of tectonic origin), of such amplitude that they both deform with power-law rheology ($n=3$), independent of grain size (m=0). For these assumptions, the effective viscosity is inversely proportional to the cubic root of second invariant of the deviatoric strain rate tensor. Non-transforming sample grains deform with an effective viscosity $\eta_{\text{mantle}} \propto I_{2\,\text{mantle}}^{-1/3}$. The grains of the transforming sample, as we show later, in addition to the externally imposed deformation undergo continuous, randomly oriented ($\left\langle \dot{\varepsilon}_{ij}^{\text{rsh}} \right\rangle = 0$, zero average over the scale of the entire sample) reshaping until the phase-change reaction is complete. That is the strain rate components within each grain could be expressed as, $\dot{\varepsilon}_{ij}^{\text{transf}} = \dot{\varepsilon}_{ij}^{\text{mantle}} + \dot{\varepsilon}_{ij}^{\text{rsh}}$. Hence, the transforming grains deform with a reduced effective viscosity $\eta_{\text{transf}} \propto I_{2\ \text{transf}}^{-1/3}$. Thus, deforming in response to the same externally imposed strain rate, $\dot{\varepsilon}_{ij}^{\text{mantle}}$, the transforming sample appears to be softer than the stable one with the ratio of effective viscosities:

$$\delta = \frac{\eta_{\text{transf}}}{\eta_{\text{mantle}}} = \left(\frac{I_2^{\text{mantle}}}{I_2^{\text{transf}}} \right)^{1/3} \tag{III-4}$$

Therefore, to evaluate the TS magnitude one needs to compare the deviatoric strain rates increased by the transformation $\langle \dot{\gamma} \rangle = \sqrt{I_2^{\text{transf}}}$ to the ones of the ambient mantle.

To characterize the transformational strain rate $\langle \dot{\gamma} \rangle$, let us consider a piece of material which undergoes transformation from the lower density phase (A) to the denser phase (B). During time interval *dt* the B-phase grows by the same mass as the A-phase decays. However, due to the density mismatch, now the mass occupies less space, and the volume of the entire piece reduces by *dV*. That allows us to define the macroscopic volumetric strain rate for the material:

$$\dot{\varepsilon}_{\text{vol}} = \frac{dV}{Vdt} = -\frac{d\rho}{\rho dt} \tag{III-5}$$

The composite material displays a finite compressibility, although each phase is assumed to be incompressible. How do the incompressible tightly-packed grains accommodate the volume change? To relate the macroscopic volumetric strain rate to the grain-scale processes inside the aggregate, we consider the evolution of the grain volume and shape. Mantle phase transformations are mainly controlled by pressure. Macroscopically, the reaction proceeds up to completion as mantle flow drags material to different depths. Microscopically, the pressure gradients along the transformational front (A-B grain interface) may affect the local transformation rate and therefore the grain shape. We propose that the adjoining/contiguous grains accommodate the overall volume change by reshaping: the deviatoric deformation causes an additional intragranular strain rate and stress. As we show in the next section, the deviatoric strain rate of reshaping is proportional to the dilatation rate:

$$\langle \dot{\gamma} \rangle = F_{\mathrm{geom}} \dot{\varepsilon}_{\mathrm{vol}} , \qquad \text{(III-6)}$$

where the effect of grain geometry, F_{geom}, is evaluated in section 2.2, followed by methods of estimating $\dot{\varepsilon}_{\mathrm{vol}}$.

It is worth noting here that the combination of equations 2-6 is in agreement with the experimentally observed characteristic features of transformational superplasticity mentioned above: the strain rate is proportional to the applied load (e.g. tectonic stress, $\sigma_{ij}^{\mathrm{mantle}}$), the volume change (e.g. *dV*), and the rate of volume change (e.g. *dV/dt*).

Grain geometry evolution

To investigate how the deviatoric strain rate of a reshaping grain is related to the macro-scale dilatation rate, we consider the phase transformation on the scale of several grains. We analyze two distinct types of grain geometry, characterized by the geometry of the denser phase (Figs 1 and 2). In both cases we assume that the rate of the transformation is given by the rate of the volume reduction, *dV/dt*, which is similar to the condition that the volumetric strain rate is given (eq. 5).

One possible scenario of grain geometry evolution is shown in Fig. 1, where we assume that the B-grains (black) grow with roughly equant geometry (e.g., controlled by strong surface tension). For illustrative purposes, although the transformation progresses continuously, we consider a thought experiment in which the transformation proceeds in three discrete steps, with the strain increment in each step small compared to the total transformational strain. During these steps, the microstructure is assumed to be in equilibrium with the imposed deviatoric strain rate and deviatoric stresses, so steady-state flow prevails. We focus on two areas: one is the contact between the growing and dissolving (gray) phases and another is the outer border of the region considered.

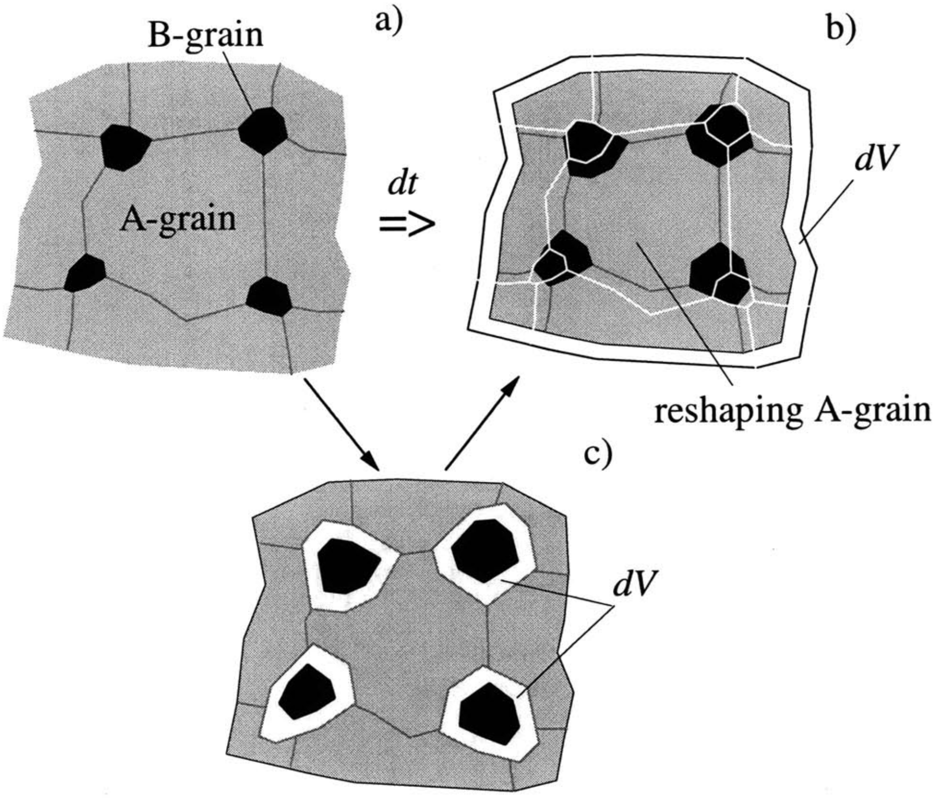

Figure III-1. Cartoon of the grain geometry evolution during a solid-solid phase transformation involving a density change, assuming that conditions favor the roughly equant geometry. Higher density B-phase grains (black) grow at the corners of less dense A-phase grains (gray). In time *dt* the old phase loses the same mass as the new phase gains, and the entire aggregate collapses by the volume *dV* (white gaps in c or white area in b). The grains supporting the framework (here the A-phase) change shape: the A-A borders move inward, and the A-B interfaces move outward to preserve continuity (compare c and b). That deviatoric deformation is related to the macroscopic dilatation of the entire sample. [The white line in b) repeats the geometry in a)].

In step one (Fig. 1a), the grains of the denser phase B are in equilibrium with the grains of old phase A. In step two (Fig 1c), during time interval *dt* a part of the A-grain transforms to B-phase at the A-B contact. Due to the density mismatch ($\rho_A < \rho_B$), now the transformed mass occupies space less by *dV*, which would open up a gap between grains of the two phases (shown by white areas). In step three (Fig. 1b), to preserve continuity and avoid empty space, flow toward the boundary between the A-B phases is required. For the geometry given, at least the A-phase grains would have to deform to fill in the gap. On the other hand, in the same time period *dt* the overall volume reduction *dV* (see Fig. 1b) occurs on the scale of the aggregate. Thus, the grains supporting the framework have to change shape in accordance with the aggregate volume collapse. Controlled by the rate of the entire volume collapse, the incompressible A-grains accommodate the total volume change by reshaping: the A-A interfaces move inward, and the A-B interfaces move outward. Similarly, at the end of the transformation, when they touch each other, the B-grains undergo the same kind of deviatoric deformation.

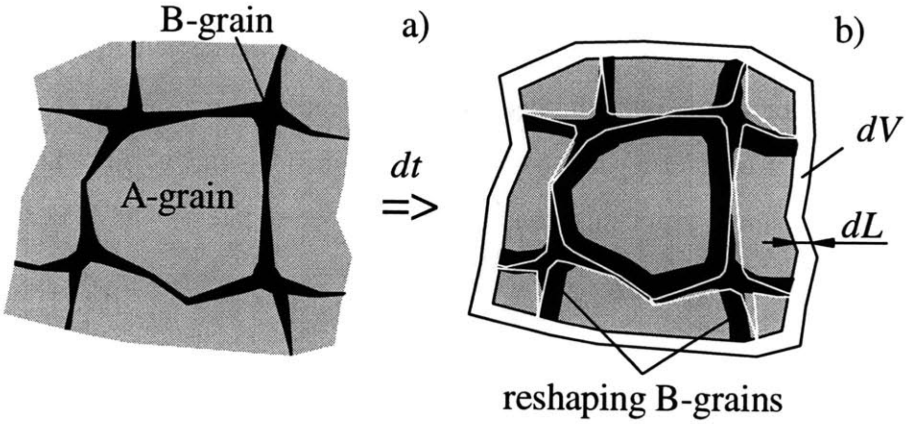

Figure III-2. Cartoon of the grain geometry evolution during a solid-solid phase transformation involving a density change, assuming that the pressure along the phase-contacts causes the B-grains (black) to grow first via development of thin films between the A-phase (gray) grains, and later through thickening. In time *dt* the old phase loses the same mass as the new phase gains, and the entire aggregate collapses by the volume *dV* (white area). The framework-supporting grains (here the B-phase) change shape: the B-B contacts move inward (by *dL*), and the A-B interfaces move outward to preserve continuity. That deviatoric deformation is related to the macroscopic dilatation of the entire sample. [The white line in b) repeats the geometry in a).]

The grain geometry evolution could change dramatically if the pressure gradient along the A-grain surface [introduced by its reshaping or externally by strong nonhydrostatic stress (Green *et al.* 1992)] were large enough to control the transformation front at the B-grain surface. Higher effective pressure would tend to cause a speed-up of the reaction near the A-A contact (or at the surfaces experiencing higher normal stresses) and a slow-down of the reaction closer to the A-grain corners. A plausible geometry resulting is shown in Fig. 2, where B-grains develop a star-like shape. As in the case considered above, there are two types of interfaces in the system, those between similar phases and those between different phases. Once the B-grains touch each other, they stop growing at the B-B contact areas. Moreover, the B-grains would have to contract parallel to the newly formed films, with the centers of the "stars" moving closer together, to accommodate the overall volume change (Fig. 2b). The transformation proceeds at the A-B interface, where the complementing flow would be directed from the shape-changing B-grain toward the A-grain. Since the B-grains adjoin each other early in the transformation, they would undergo internal deformation (thickening and shortening) throughout most of the reaction.

Although the two scenarios of transformational geometry are quite different, the magnitude of the reshaping-grain surface displacement can be described in a similar way. The inward displacement equals the decrease in the radial dimension of the entire piece *dL* (see Fig. 2b). Considering the volume change in time, *dt*, we introduce the radial velocity of the reshaping grain surface in 3D and 2D coordinates:

$$v_{\text{in}}^{\text{3D}} = \frac{dL}{dt} = \dot{\varepsilon}_{\text{vol}} \frac{L}{3} \text{ and } v_{\text{in}}^{\text{2D}} = \dot{\varepsilon}_{\text{vol}} \frac{L}{2}. \tag{III-7}$$

Since the reshaping grain is incompressible, the outward flux must be equal to the inward flux:

$$v_{\text{out}} S_{\text{out}} = v_{\text{in}} S_{\text{in}}, \tag{III-8}$$

where S_{out} is the A-to-B contact area, and S_{in} is the similar-phase contact area. Note, that although the mass of each grain is changing during transformation, the deviatoric deformation considered here can be described as for an incompressible grain.

The last equations are written in terms of the macroscopic dilatation rate, but the displacements they describe are purely deviatoric: they cause a change of grain shape, not volume. The inward and the outward fluxes imposed at the grain surface create stresses which drive flow of matter inside the reshaping grains. We propose that the gradients of the internal flow velocities are the origin of the intra-grain strain rate during the transformation.

Geometry effect, F_{geom}

The magnitude of the internal deformation is controlled by the amount of grain to be displaced inward in response to the volume collapse. For each particular grain it depends on the hardness and geometry of its neighbors. If we consider all the complexity of these interactions, the problem becomes overwhelmingly difficult to solve. Instead, to understand the general effect of grain reshaping on material rheology, we assume that the rate of transformation is given, and simplify the grain geometry in Fig. 1 and Fig. 2 to the two end-member situations shown in Fig. 4 and Fig. 3 respectively. Then we calculate the second invariant of the deviatoric strain rate tensor inside the reshaping grain, $I_2 = \dot{\varepsilon}_{ij}\dot{\varepsilon}_{ij}/2$, and compare the deviatoric strain rate, $\langle\dot{\gamma}\rangle = \sqrt{I_2}$ (as in eq. 6), averaged over the grain volume, to the ambient mantle strain rates in order to calculate the reduction of the material viscosity.

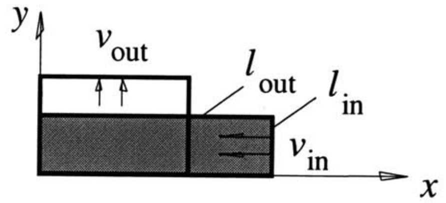

Figure III-3. Homogeneous deformation of the B-grain film occurring at the beginning of the transformation in the scenario in Fig. 2. To accommodate the macroscopic volume collapse, the B-B contact areas (in 2D, of length l_{in}) move inward with velocity v_{in}. To preserve continuity a flow occurs toward the A-B contact with velocity v_{out} across the surface distance l_{out}.

We begin with the simpler case of reshaping grain geometry, a B-grain cage growing around the A-phase grains (Fig. 2). While the volume of the central part of the B-grain is relatively small, the deformation of the B-grain wings is almost homogeneous. Therefore, to calculate the deviatoric strain rate averaged over the B-grain volume at the beginning of the reaction, $\langle\dot{\gamma}\rangle_{\text{brick}}$, we consider a pure shear deformation of a single B-wing: a two dimensional brick, which shortens in the horizontal direction and thickens in the vertical (see Fig. 3, where l_{in} and l_{out} in 2D have similar meaning as S_{in} and S_{out} in 3D). The inward velocity for the 2D rectangular brick would be:

$$v_{\text{in}} = \frac{l_{\text{in}} + l_{\text{out}}}{2}\dot{\varepsilon}_{\text{vol}},$$

in analogy with eq. (7). Since the off diagonal shear components, $\dot{\varepsilon}_{xy}$, are zero for that deformation, the second invariant of the strain rate tensor simplifies to $I_2 = \dot{\varepsilon}_{xx}^2 = \dot{\varepsilon}_{yy}^2$, where the horizontal normal component is

$$\dot{\varepsilon}_{xx} = \frac{dx}{xdt} = \frac{v_{\text{in}}}{l_{\text{out}}}.$$

Substituting the inward velocity, we write the averaged deviatoric strain rate as:

$$\langle \dot{\gamma} \rangle_{\text{brick}} = \frac{l_{\text{in}} + l_{\text{out}}}{2l_{\text{out}}} \dot{\varepsilon}_{\text{vol}} = \frac{1}{2\lambda} \dot{\varepsilon}_{\text{vol}}, \qquad \text{(III-9)}$$

where λ is in terms of the fraction of the reshaping material: $\lambda = \sqrt{1 - f_\mu}$.

The "pure shear" approximation breaks down when the contribution from the central part of the grain grows. The requirement of zero deviatoric strain rate at the grain center and the high gradient of the flow at the radius of the central part (where the wings are attached) enlarges the second invariant significantly. To estimate the average strain rate of this highly heterogeneous deformation, we consider a more complicated grain geometry and mass flux distribution.

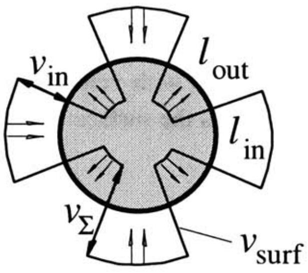

Figure III-4. Heterogeneous deformation simulating the reshaping of the A-grain in the case of the equant geometry (as in Fig. 1) or of the B-grain in the late stage of the star-like geometry (as in Fig. 2b). The flow of the incompressible circular grain is driven by boundary conditions on the radial velocity. The flux inward with velocity v_{in} across length l_{in} (in response to the macroscopic volume collapse) equals the flux outward with velocity v_{out} across length l_{out}. The surface velocity contrast v_Σ is related to the macroscopic dilatation rate.

The bulkier shape of the B-grain resembles the deformation state in the reshaping A-grain of the round-geometry case (Fig. 1). The reshaping of the A-grain can be viewed as viscous flow of an incompressible medium driven by surface boundary conditions on the radial velocity. Then the amplitude of the deviatoric strain rate is scaled with the surface velocity contrast, $v_\Sigma = v_{\text{in}} + v_{\text{out}}$, and the length scale is related to the ratio between the outward and the inward flow areas. To get a qualitative estimate of the deviatoric strain rate, we consider viscous flow of a 2D-circular grain of radius R which is driven by its surface motion, with velocity contrast (using eq. 7 and eq. 8):

$$v_{\Sigma} = \frac{v_{\mathrm{in}}}{\lambda} = \frac{L}{2\lambda}\dot{\varepsilon}_{\mathrm{vol}}. \tag{III-10}$$

(see Appendix for complete derivation). The actual problem is very complex due to the variety of grain geometries. Our choice of a circular geometry underestimates the amplitude of the deviatoric strain rate because the introduction of any sharp edges or corners will increase the flow velocity gradients (if the flux and the volume are kept the same), and hence will raise the deviatoric strain rate, $\langle \dot{\gamma} \rangle$.

The second invariant of the strain rate tensor for 2-D cylindrical incompressible flow in terms of shear and normal components of the deviatoric strain rate:

$$I_2(r,\theta) = \dot{\varepsilon}_{rr}^2 + \dot{\varepsilon}_{r\theta}^2, \tag{III-11}$$

is a function of position inside the grain.

On the local (r,θ) scale, the introduction of sharp edges in the grain geometry, particularly at the triple junctions where the outward flow is close to the inward flow, enlarges the flow gradients and therefore the second invariant significantly. For the same reasons, the amplitude of I_2 is sensitive to the relative size of the grains; it enlarges locally around the A-B border at the beginning and end of the transformation. To investigate these effects on the scale of the entire grain, we calculate the amplitude of the deviatoric strain rate averaged over the grain:

$$\langle \dot{\gamma} \rangle_{\mathrm{cirle}} = \left\langle \sqrt{I_2(r,\theta)} \right\rangle_{\mathrm{grain}}, \tag{III-12}$$

where the strain rate partitions proportionally to the volume fraction. The weak (high strain rate) outer layers of the grain would accommodate more strain compared to the central ones. Later, when calculating the viscosity of the entire composite, we use an approach which accounts for the effect of the interconnected weak layers (see eq. 16). However, here we use a simple averaging to illustrate the similarity between the results of a numerical evaluation of the $\langle \dot{\gamma} \rangle$-amplitude in the general case (12) and the results of analytical solutions in several distinctive situations.

First, let us consider the state of the transformation when the areas for outflow and inflow are almost equal to each other. The surface boundary condition on the reshaping grain can then be approximated by a monochromatic function, for example, a sinusoid with a wavenumber equal to the number of outflow areas. The second invariant becomes a radial function only, and the averaged deviatoric strain rate simplifies to:

$$\langle \dot{\gamma} \rangle_{\text{mono}} \propto \frac{\pi}{2\sqrt{f_\mu}} \dot{\varepsilon}_{\text{vol}} . \qquad \text{(III-13)}$$

At the very beginning of the transformation, the size of the B-grain is much smaller than the A-grain, and its shape is close to spherical. Then the flow is mainly concentrated around the B-grain and, being little influenced by the neighboring B-grains, can be approximated as radially symmetric. The problem becomes similar to one of a collapsing bore-hole (or pore) in glaciology or to a micro-flow described by Morris (1992). The continuity equation in 3D-spherical geometry gives the radial flow velocity as: $v_r = C/r^2$, where r is the distance from the center of the B-grain, and the constant $C = \frac{1}{4\pi} \frac{dV}{dt}$ is determined by conserving mass across the A-B contact area. The deviatoric strain rate averaged over the grain volume becomes:

$$\langle \dot{\gamma} \rangle_{\text{pore}} = \frac{2}{f_\mu} \ln\left(\frac{R_A}{R_B} \right) \dot{\varepsilon}_{\text{vol}} , \qquad \text{(III-14)}$$

where $R_A >> R_B$. If during the nucleation period the new-born grains are a hundred times smaller than the old grains, the deviatoric strain rate can exceed the dilatation rate by an order of magnitude. The larger the number of nucleation sites, the bigger the transformational strain rate.

In a more realistic, general case (eq. 12), we evaluate the amplitude of $\langle \dot{\gamma} \rangle$ numerically for two cases: when the number of A-grains equals the number of B-grains, s=1, and when the number of nucleation sites is four times more, s=4.

To summarize the effect of the grain configuration, we plot the geometry function F_{geom} (as in eq. 6) versus the fraction of B-phase for the different approximations (9, 12, 13, 14) on the same axes (see Fig. 5). We display the areas where the approximation does not work with dashed lines. Note that the "circle" case curves show a weak dependence on s, which is in accordance to the "mono" and the "pore" approximations. Since the Fourier set is not effective in expanding a delta-function, the "circle" case blows up at $f_\mu \rightarrow 0, 1$. We thus have to bound this case by the value from the collapsing pore estimation. Also, these curves exceed the "mono" approximation due to the introduction of sharp edges (coupling between long- and short-wavelength flow).

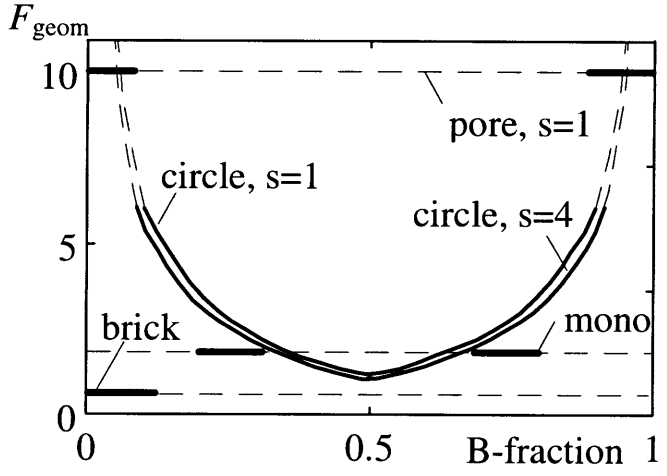

Figure III-5. The geometry function (the coefficient of proportionality between the deviatoric strain rate of the reshaping grain and the volumetric strain rate of the entire aggregate) versus the degree of transformation. The solid lines correspond to the areas of validity for the different approximations considered. The "pore" and "brick" cases describe the beginning of the transformation in the equant and the star-like geometry respectively. The "circle" is for the heterogeneous deformation of the contiguous grains in the developed stage of the transformation, where s equals the number of the new-phase grains per old-phase grain. The "mono" line corresponds to an idealized monochromatic deformation of the reshaping grain.

Summarizing, the value of the transformational deviatoric strain rate is proportional to the dilatational strain rate, with a factor of one to ten. A sharp geometry of the transforming grains and a difference in the phase volume fractions enlarge the coefficient of proportionality.

Volumetric strain rate, $\dot{\varepsilon}_{\mathrm{vol}}$

The next step in evaluating the transformational strain rate is to calculate the macroscopic volumetric strain rate, $\dot{\varepsilon}_{\mathrm{vol}}$ (eq. 6). According to its functional dependence (5) the dilatation rate can be expressed through the rate of the relative density or volume change. Correspondingly, we consider two ways to determine $\dot{\varepsilon}_{\mathrm{vol}}$.

One way is to estimate the rate of relative density change. Dealing with phase transformations associated with mantle convection, one should keep in mind that convective flow drives the material through the transformational pressure for a given temperature. For a Lagrangian piece of mantle the pressure changes at rate proportional to the flow velocity, v_{fl}. This velocity relates the volumetric dilatation rate to the sharpness of the density change:

$$\dot{\varepsilon}_{\mathrm{vol}} = \frac{v_{\mathrm{fl}} d\rho}{dz \rho}. \tag{III-15}$$

It is possible to estimate the thickness *dz* of the sharp changes in density by analyzing seismic waves reflected from them (Engdahl & Flinn 1969; Whitcomb & Anderson 1970). Analysis of the reflection coefficient as a function of acoustic impedance contrast across the phase change region constrains its thickness to about 1-4 km (Richards 1972; Lees *et al.* 1983; Benz & Vidale 1993) for both major phase changes, at 400- and 670-km depths. This does not necessarily mean that the transformation has completed inside such a small pressure interval, but it assures that most of the density change $d\rho$ occurs within it (we discuss the nature of metastable transformations below).

Two uncertainties arise when using seismic reflectivity estimations. The first is that the dilatation rate depends on the rate of vertical mantle flow. Secondly, the data represent the overall change in density, without distinction as to whether it is mainly due to a large number of new-born small grains, or to fast growth of a few grains born at the beginning of the reaction, a distinction that is crucial for the rheology.

To resolve this dilemma we use an additional way of estimating $\dot{\varepsilon}_{\mathrm{vol}}$; we calculate the rate of relative volume change. Assuming that the volume of a particular phase is $V=NV_{\iota}$ (here V_{ι} is the volume of one grain and N is the number of grains), its change with time can be written as $dV/dt = V_t \, dN/dt + N \, dV_t/dt$, where dN/dt can be seen as a nucleation rate and dV_t/dt as a growth rate. Although it is very difficult to estimate the nucleation and growth rates for the actual non-isobaric, non-isothermal solid-solid phase transformations occurring in the mantle, one can at least estimate their relative importance under specified conditions.

To describe a non-isothermal solid-solid transformation of normal hot mantle material, an analytical approach was taken by Solomatov & Stevenson (1994). A phase transformation between the α–β structure of multi-component olivine is assumed to occur by the nucleation and growth mechanism. Due to the small concentration of fayalite in mantle olivine, $Mg_{1.8}Fe_{0.2}SiO_4$, there is a thin region where both phases coexist in equilibrium and where the macroscopically observed density changes occur. Depending on the particular *pT*-composition path taken by a piece of material, the thickness of the two-phase region varies, directly affecting the seismic reflectivity coefficient. Similar to many solid-solid transformations involving a density change, deep mantle phase changes cannot initiate at equilibrium conditions. A finite protrusion into the metastable region produces a driving force large enough to overcome an energetic barrier created by the elastic stresses and the surface tension around a nucleus. Many factors, such as chemical diffusion, multiple components, or an effective shape factor can increase this metastable overstep further. If at equilibrium conditions the transformation width is about 10-20 km (Rubie *at el.* 1990), sluggish kinetics (the transformational front propagates slower than the convective one) and a large nucleation barrier (comparable to the equilibrium width) can reduce the width to 3-4 km (Solomatov & Stevenson 1994). The non-equilibrium reaction starts by an avalanche-like nucleation and proceeds through a long period of return to equilibrium mainly through the growth of stable grains. Since olivine consists of two components, growth is controlled by chemical diffusion. Thus, the growth rate depends not only on the value of the metastable overshoot, but also on the crystal size. The domination of one process over the other allows us to view the overall volume change in terms of the nucleation rate, $dV/dt \approx V_t \, dN/dt$, during the nucleation period, and in terms of the growth rate,

$dV/dt \approx N\, dV_i/dt$, during the rest of the reaction (if post-nucleation ripening can be ignored).

Applying seismic reflectivity data, we estimate an order of magnitude volumetric strain rate (due to uncertainty in the vertical velocity). To calculate the functional dependence of $\dot{\varepsilon}_{\mathrm{vol}}$ versus depth for the phase change at 400-km depth, we apply Solomatov's model. Both approaches give comparable results (see Results section).

Mixed rheology / weak framework

Introducing the degree of softening due to grain reshaping (eq. 4), we did not take into account that only a fraction of the grains experiences the additional deformation, and that the size and the number of the new-phase grains change continuously with time. The heterogeneous distribution of the parameters controlling deformation (e.g., diffusion coefficient, grain size and shape) strongly affects the rheological law of the entire aggregate. There are several methods to calculate the volume averaged strain rate or stress for a composite material. Here we apply a phenomenological approach suggested by Handy (1994), who analyzed the flow laws of rheologically and structurally heterogeneous rocks consisting of interconnected strong/weak phases. The advantage of Handy's approach is that when calculating the degree of stress and strain partitioning, in addition to the volume fraction of a particular phase, it also accounts for the viscosity contrast between phases, as well as the impingement effect.

Since mantle phase transformations are mainly pressure-driven, it is likely that the new phase would tend to form an interconnected frame (e.g. the geometry in Fig. 2 or a developed stage of the reaction shown in Fig. 1b). Due to smaller grain size and larger intragranular stress, that phase might be weaker than the old, dissolving one. An aggregate with an interconnected weak phase would tend to creep more easily than one with isolated weak grains. To account for the particular configuration when calculating the bulk rheology, we write the viscosity of the aggregate composed of strong (*s*) and interconnected weak (*w*) phases:

$$\eta_{\mathrm{aggr}} = \eta_{\mathrm{w}} f_w^{2\delta-1} + \eta_{\mathrm{s}} \left(1 - f_w^{\delta}\right)^2 f_s^{-1}, \qquad \text{(III-16)}$$

where η and f are the effective viscosity and the volume fraction, and $0<\delta<1$ is the parameter defining the viscosity contrast between phases, $\delta = \eta_\mathrm{w} / \eta_\mathrm{s}$ (Handy, 1994). When the phases are very different, $\delta \to 0$, the aggregate viscosity is mainly determined by the weaker phase, which is compensated by its volume fraction. In order to reduce the extrapolation ambiguities, instead of calculating the absolute value we consider the reduction of the effective viscosity, $\zeta = \eta_\mathrm{mantle} / \eta_\mathrm{aggr}$: the ratio of the ambient mantle viscosity (when no transformation exists) to the viscosity of the aggregate undergoing a phase transformation under the same pT-conditions. Substituting eq. (16) we obtain the macroscopic effective viscosity reduction inside the transformational region:

$$\zeta = \left[\frac{\eta_\mathrm{w}}{\eta_\mathrm{mantle}} f_w^{2\delta-1} + \frac{\eta_\mathrm{s}}{\eta_\mathrm{mantle}} \left(1 - f_w^\delta\right)^2 f_s^{-1} \right]^{-1} \qquad \text{(III-17)}$$

Here we evaluate equation (17) analytically for different types of mantle rheology, but under the condition that only one creep mechanism operates. Later, in the Results section, we calculate the viscosity reduction for the most relevant plastic deformation mechanisms for the mantle: diffusion creep and climb-controlled creep (Ranalli 1991), which can operate simultaneously.

Suppose that the ambient mantle and the transforming aggregate have a power-law rheology with $n=3$. Then the reshaping phase would be weakened due to additional deformation, and the viscosity contrast parameter is: $\delta = \left(I_2^\mathrm{mantle} / I_2^\mathrm{transf} \right)^{1/3}$ (as in eq. 4). Therefore, for climb-controlled creep the viscosity reduction becomes:

$$\zeta_\mathrm{disl} = \left[\delta f_w^{2\delta-1} + \left(1 - f_w^\delta\right)^2 f_s^{-1} \right]^{-1}, \qquad \text{(III-18)}$$

which can be further simplified for the high-viscosity-contrast phases (using eq. 6):

$$\zeta_\mathrm{disl}\Big|_{\delta\to 0} \approx f_w \left(\frac{\langle \dot{\gamma} \rangle}{\dot{\gamma}_\mathrm{mantle}} \right)^{2/3} = f_w \left(\frac{F_\mathrm{geom} \dot{\varepsilon}_\mathrm{vol}}{\dot{\gamma}_\mathrm{mantle}} \right)^{2/3} \qquad \text{(III-19)}$$

Suppose that the ambient mantle and the transforming aggregate have a linear rheology. That is, assume that the stresses are low and that diffusion creep, sensitive to grain size, becomes dominant, defining a linear rheology with effective viscosity: $\eta_{\text{eff}} \propto d^m$ (Frost & Ashby 1982). Then the newly growing phase would be weaker due to reduced grain size. Let us consider the beginning of the transformation, when the new grains are very small and the dissolving ones are about the same size, *d*, as the ones of the ambient mantle. Then the viscosity contrast parameter is: $\delta = \left(d_{\text{B}}/d\right)^m$, and for the highly different phases the viscosity reduction becomes:

$$\zeta_{\text{diff}}\Big|_{\delta\to 0} \approx f_w\left(\frac{d}{d_B}\right)^m . \qquad \text{(III-20)}$$

Since the number of new-born and successfully growing B-grains may be constrained by the saturation of the available nucleation sites, we express the volume fraction in terms of the grain number and size: $f_\mu = \frac{V_B}{V} = \frac{d_B^3 N_B}{d^3 N}$. Introducing the number of nucleation sites per grain, $s = N_B/N$, we write the viscosity reduction for diffusion creep as:

$$\zeta_{\text{diff}}\Big|_{\delta\to 0} \approx s\left(\frac{d}{d_B}\right)^{m-3} . \qquad \text{(III-21)}$$

A greater effect is expected for material deforming by Coble creep (m = 3) when the viscosity reduction is determined by the number of nucleation sites per grain, *s*. To provide a noticeable softening during Nabarro-Herring creep (m = 2), the number of nucleation sites has to exceed the grain size ratio: $s >> d/d_B$.

RESULTS

Here we integrate our model of TS-phenomenon with available kinetic theory, seismic and rheological data. Complications arise because the TS value is related to the deviatoric deformation, so it varies laterally with the flow pattern. How important are these variations? To answer, we first estimate the mean TS value for the two major phase changes, at 400- and 670-km depths. Then we calculate the laterally varying transformational softening and discuss the TS-effect on the geoid and on mantle flow velocities.

Phase change at 400 km depth.

In this section we estimate the reduction of effective viscosity for the phase transformation at a depth of about 400 km. We apply kinetic theory (Solomatov 1995) to calculate the grain growth and the phase fractions as functions of time (depth for steady flow). For the mid-point of the transformation we estimate the TS for power-law rheology, and then we calculate the degree of softening for mixed rheologies using the DMM technique and available rheological data for olivine.

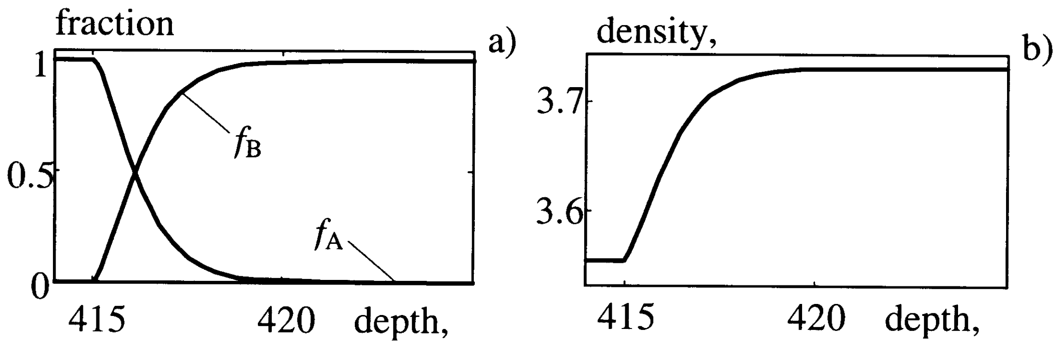

Figure III-6. The olivine-spinel phase transformation of mantle sinking at velocity v_{fl} =5 cm year^{-1} at depth 400 km and temperature 1800 K. An equilibrium thickness of the two-phase region is assumed as 10 km. The parameter characterizing the maximum overpressure (or supercooling) is p=60. Volume fractions of the olivine phase (f_A) and the spinel-structure phase (f_B) are displayed versus depth (a). Most of the 6 per cent density change occurs in the 2-3 km thick layer (b).

As was discussed in the Methodology section, we consider a transformation which starts from high-temperature metastable conditions. The nucleation stage completes rapidly and the relaxation proceeds through grain growth alone. We assume an equilibrium thickness of the two-phase region of 10 km and a parameter for the maximum overpressure (or supercooling) of p=60. Assuming that the mantle sinks through the phase change region at a characteristic velocity of v_{fl} =5 cm year^{-1}, we calculate the volume fraction of dissolving, f_A, and growing, f_B, phases as functions of depth (Fig. 6a). The major part of the 6 per cent density change occurs during the first 2-3 km (Fig. 6b).

Given the rate of density change we calculate the macroscopic volumetric strain rate $\dot{\varepsilon}_{\text{vol}}^{\text{kinetic}}$ and plot it versus depth in Fig. 7 (thick line) together with the dilatation rate evaluated from seismic reflections ($\dot{\varepsilon}_{\text{vol}}^{\text{seismic}}$, dashed line) and a typical creep rate for the mantle ($\dot{\gamma}_{\text{mantle}} \approx 10^{-15}\,\text{sec}^{-1}$, dashed-dotted line). The theoretical curve, $\dot{\varepsilon}_{\text{vol}}^{\text{kinetic}}(z)$, reaches its maximum value of $5\cdot 10^{-14}\,\text{sec}^{-1}$ at a depth near the mid-point of the transformation. The result is consistent with the estimate from seismic reflectivity data: $\dot{\varepsilon}_{\text{vol}}^{\text{seismic}} \approx 6\cdot 10^{-14}\,\text{sec}^{-1}$, where we applied eq. 15 and assumed that 6 per cent of the density variation occurs in a 1.5 km thick two-phase region. Given $\dot{\varepsilon}_{\text{vol}}^{\text{kinetic}}$ and a moderate effect of grain-geometry, F_{geom}=5, we calculate the transformational strain rate $\langle\dot{\gamma}\rangle$ (eq. 6, thin line in Fig. 7)

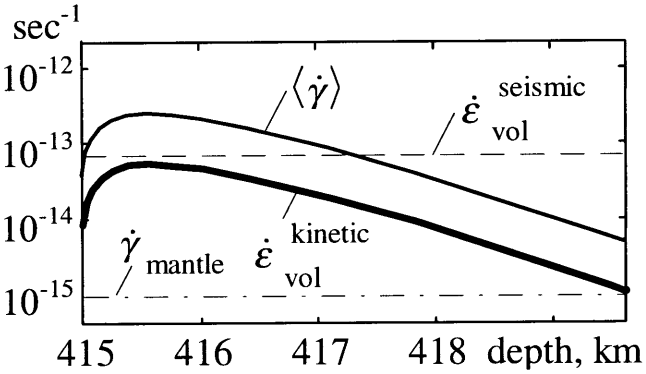

Figure III-7. Strain rates versus depth of polycrystalline material passing through the transformational conditions. The macroscopic volumetric strain rates, $\dot{\varepsilon}_{\text{vol}}^{\text{kinetic}}$ (thick solid line, calculated using the kinetic theory) and $\dot{\varepsilon}_{\text{vol}}^{\text{seismic}}$ (dashed line, evaluated from the seismic reflections), are superimposed on a typical creep rate of the mantle, $\dot{\gamma}_{\text{mantle}}$≈$10^{-15}$ sec^{-1} (dash-dotted line) and the transformational strain rate, $\langle\dot{\gamma}\rangle$ (thin line, calculated given $\dot{\varepsilon}_{\text{vol}}^{\text{kinetic}}$ and F_{geom}=5).

Given volume fractions (Fig. 6a), transformational strain rate (Fig. 7), and creep rate of the ambient mantle, and assuming power-law rheology we can estimate the viscosity reduction using eq. 19. For high transformational strain rates, $\langle\dot{\gamma}\rangle >> \dot{\gamma}_{\text{mantle}}$, we obtain the effective viscosity reduction in the first 1 km of the reaction:

$$\zeta_{\text{disl}}^{400} \approx 25 \div 35. \qquad \text{(III-22)}$$

Of course, variations of vertical flow velocity and ambient mantle deviatoric strain rate would affect the TS value.

To estimate the superplasticity for a mixed-rheology mantle one needs to define the deformation parameters: grain size, tectonic stress or strain rate, diffusion coefficients, activation volume, etc., and their variation with depth. Unfortunately, no data are available to describe the deformation of mantle material at the depths of the phase transformations on geologic time scales. Extrapolation of results from laboratory experiments by several orders of magnitude in strain rate and poorly constrained oxygen fugacity introduce large uncertainties to the absolute values, but should still be representative of their relative dependencies. To account for this we normalize the constitutive relationships (Frost & Ashby 1982) and build a DMM to explore the relative dependencies (Fig. 8). Although the preceding discussion is cast in terms of strain rates, DMM are typically plotted as contours of relative effective viscosity in stress vs. grain-size coordinates. We arbitrarily choose a reference grain size and stress where strain rates from two linear rheologies (Coble creep, m=3 and Nabarro-Herring creep, m=2) and power-law rheology contribute equally.

Contours of the ambient (no transformation) effective viscosity are calculated according to Frost & Ashby (1982) and are shown in Fig. 8 by the thick solid lines. These fields of dominant flow mechanism can be distinguished on the map. Below and to the left of the NW-SE diagonal the material creeps mainly by diffusional flow; viscosity increases with grain size and is independent of stress. For $d<d_0$, viscosity decreases as d^3, while for $d>d_0$, viscosity depends on d^2, so the vertical contours of effective viscosity are more closely spaced on the left side of the DMM. Above and to the right of the diagonal power-law creep is dominant and the effective viscosity is independent of grain size but decreases as stress increases.

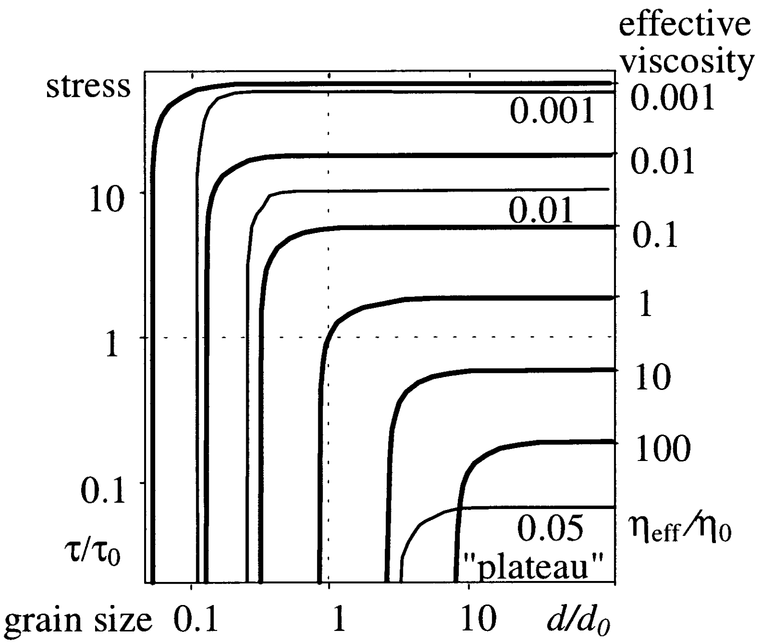

Figure III-8. Deformation mechanism map for mantle material at a depth of about 400 km and temperature 1800 K. The axes, grain size (abscissa) and deviatoric stress (ordinate), are scaled with reference values chosen such that the three deformation mechanisms, climb-controlled creep (above and right of the NW-SE diagonal), diffusion-through-lattice creep (right side, below the diagonal), and diffusion-along-grain-boundaries creep (left side, below the diagonal) contribute equally at the reference stress, grain size, and mantle strain rate. Contours of the effective viscosity of the non-transforming mantle are shown by the thick lines. The contour levels relative to the reference value are displayed along the right side of the map. The relative effective viscosity of the transforming mantle is shown by the thin contour lines. The field forms a dislocational creep "plateau" of constant viscosity (right bottom corner) controlled by the transformational stresses. A value of $s=10$ is assumed.

To construct a DMM for a superplastic mantle, we calculate the effective viscosity (16) by converting the transformational strain rate from Fig. 7 into stress and display the contours by the thin lines in Fig. 8. The transformational stress controls the viscosity in the low stress power-law regime (at lower tectonic stress and large grain size): the effective viscosity field develops a dislocation creep "plateau" of constant viscosity (bottom right corner). For the data used in Fig. 8, the effective viscosity of the transforming mantle reaches its maximum at the plateau with a value of about 5 per cent of the reference viscosity. The effect of the transformation is small when the internal and external stresses are comparable (upper part of Fig. 8) and/or when the grain boundary diffusional regime becomes dominant (left side of Fig. 8).

By comparing the viscosities for the ambient (thick contours) and transformational mantle (thin contours), we can determine TS value, ζ, as a function of the assumed stress and grain size in the ambient mantle. There are three main regions of variation in TS, corresponding to the three participating deformational mechanisms. The maximum reduction, by over a factor of 1,000 in the bottom-right corner, occurs in the low stress, large grain size regime. The diffusion creep region (vertical contour lines) is subdivided into two areas. For $d/d_0<1$ softening is controlled by Coble creep (left contour $\zeta=1.5$), while in the region dominated by Nabarro-Herring creep in the ambient mantle, the reduction in viscosity due to TS results from moving the high-stress regime into this area. If we constrain the number of nucleation sites to one ($s=1$), grain-size related superplasticity provides only a small degree of softening - less than a factor of two. To explore the effect of granularity, we show the effect of TS when $s=10$. In agreement with eq. (21), the degree of softening equals the site number in Coble creep (far left). The viscosity is 7 times less, compared to its value for the untransforming mantle during Nabarro-Herring creep.

For a broad range of typical mantle parameters, the reduction of the effective viscosity varies from 10 to 200 times. Of course, one should remember that in estimating the transformational strain rate, we chose a moderate value for the grain-geometry effect. Should the particular configuration cause larger internal strain rates in the aggregate, the effect of transformational superplasticity becomes stronger.

Phase change at 670 km depth.

The solid-solid phase transformation at a depth of about 670-km is fundamentally different from the α–β transition because it involves a change in the chemical composition between the components. The olivine and pyroxene-garnet components transform into an aggregate of magnesiowustite and perovskite. Since there are no reliable rheological data for these components, and no well-developed theory to describe the kinetics of this phase transformation, we do not present a detailed analysis of transformational superplasticity of the mantle at that depth. However, assuming that chemical diffusion is a controlling factor in this non-isothermal reaction and that a similar transformation-imposed strain-rate mechanism to the one we have been studying operates, we estimate the effective viscosity reduction using the same approach we have been using.

Given a 10 per cent density change across the 1 km thick phase change region, a mantle flow velocity on the of order 5 cm/year, and a geometry effect F_{geom}=5, the transformational strain rate is $\langle\dot{\gamma}\rangle_{670} \approx 7.5 \cdot 10^{-13}\,\text{sec}^{-1}$. Using eq. (19) we obtain a reduction of viscosity in the power-law regime:

$$\zeta_{670}^{\text{disl}} \approx 70. \qquad \text{(III-23)}$$

Transformational Superplasticity field.

Although anomalous softening is a characteristic feature at 400- and 670-km depths, its magnitude varies with the pattern and vigor of the flow. The lateral variations of viscosity within the thin layer couple the various wavelengths, introducing a non-linearity into the dynamics of mantle flow. In this section we calculate the laterally varying softening for an Earth model and analyze its frequency characteristics.

The maximum effect would occur if the mantle deformed by power-law rheology and the softening were large enough to approximate it with eq. (19). The TS magnitude then would be a power function of the spatial ratio between the radial flow velocity and the deviatoric strain rate:

$$\zeta_{\text{phase}} \approx \left(\frac{v_{\text{rad}}}{\dot{\gamma}_{\text{mantle}} dz}\right)^{2/3}, \qquad \text{(III-24)}$$

where we assumed that the combined effect of the relative density change, the geometry effect, and the volume fraction is of order unity. We built a compressible mantle model with PREM density (Dziewonski & Anderson 1981) and reference viscosity profile W4a from Hager & Richards (1989). Following the approach of Panasyuk *et al.* (1996), we calculated the mantle flow velocity and strain rate kernels and convolved them with the density anomaly model, a seismic tomography model converted with a $d\ln\rho/d\ln V_S$ profile. For illustrative purposes we chose the global shear-wave seismic velocity anomaly model by Masters *et al.* (1996), and the conversion factors of 0.056 and 0.09 in the upper and the lower mantle, respectively. Note that this mantle flow model assumes a Newtonian rheology, so we are not being self-consistent, but the results from this model should serve as a useful first approximation.

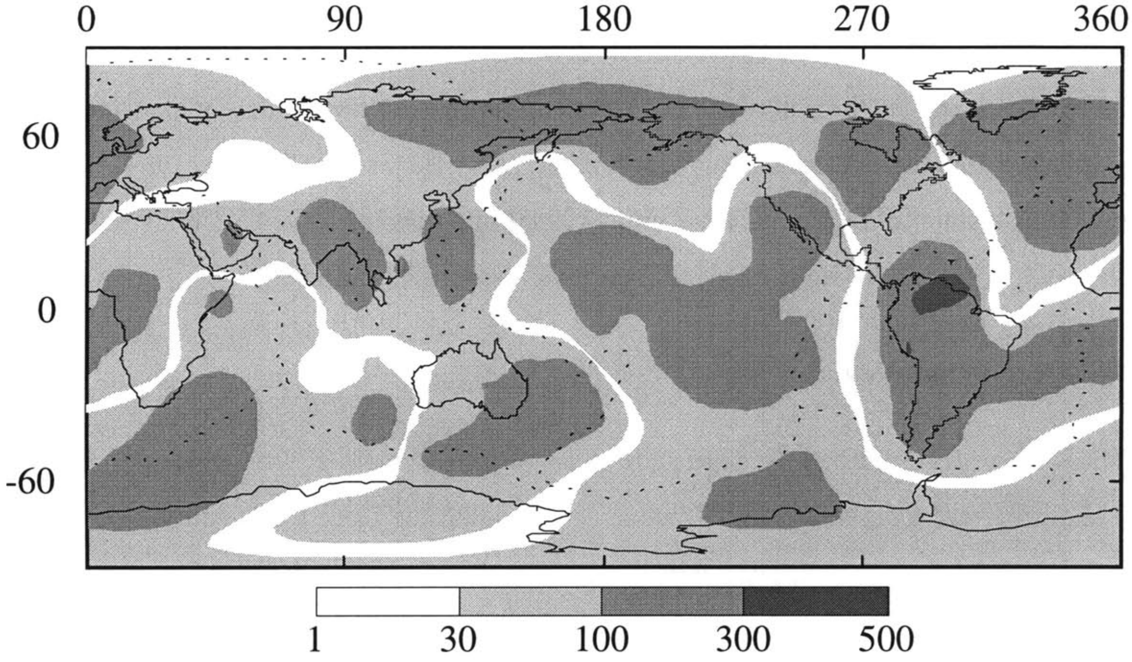

Figure III-9. Transformational superplasticity map at 670-km depth for a mantle flow model with lateral density contrasts inferred from a global seismic tomography model (see text for description and references). The viscosity decreases by a factor of 1 to 500, with the mean value of the reduction about a factor of 90. It has order of magnitude variations at intermediate-to-long wavelengths (white and light gray areas). The locations of the biggest viscosity reductions (dark gray areas) roughly correlate with the major upwellings (such as beneath the Central Pacific, the North Atlantic, and south of Africa) and downwellings (near the circum Pacific subduction zones, West Africa, and the South Atlantic) of the mantle flow in this model. There are a few spots where the TS reaches 3 to 5 times the mean (the black area).

The flow that develops is characterized by large-scale upwellings beneath the Central Pacific, the North Atlantic, and south of Africa, and downwellings near the Circum Pacific subduction zones, West Africa, and the South Atlantic. The locations of the biggest viscosity reductions inside the transformational region at 670-km depth roughly correlate with the major up- and down-wellings in this model. The TS-field shows that viscosity reduces by 1 to 500 times (Fig. 9). The mean value of the viscosity reduction due to superplasticity is about 90 and it has order of magnitude variations at intermediate-to-long wavelengths. However, there are regions where the TS is 1 to 3 times the mean (dark gray areas), and a few spots where the TS reaches 3 to 5 times the mean (the black area). That the lateral variations in TS are dominant at $l\approx 6$, as in Fig. 9, can be understood from eq. (25). Since TS is related to the magnitude of the radial flow, it fluctuates at half of the flow-dominant wavelength, which is $l\approx 3$ for this viscosity and density anomaly model. However, if density anomalies generate mantle flow with increased power at the intermediate wavelengths [as for the models which include the subducted-slab-associated density anomalies, (e.g. Hager & Clayton, 1989) or as for regional seismic tomography (e.g. Grand 1994)], the power of the TS-field would tend to flatten, increasing the significance of short wavelength variations.

TS effect on mantle flow

The effect of a uniformly softened layer on mantle flow with linear rheology is straightforward to investigate. However, to evaluate the effects of coupling of different harmonics one needs to apply a non-linear analysis or numerical methods. We approach some aspects of the problem below, but the complete analysis is beyond the scope of this paper.

Previously, we briefly discussed the effect of transformational superplasticity on global mantle flow (Panasyuk *et al.* 1996). Particularly, we evaluated the system of equations governing mantle flow across an assumed uniform viscosity phase transformation region and reduced it to a set of boundary conditions in the spherical harmonic domain [eq. 40 in Panasyuk *et al.* (1996)]. However, in the case of a thin layer with laterally variable viscosity, the boundary conditions across this layer should be written in the space, not the frequency, domain. For a thin layer with significantly reduced viscosity within it, the stresses can be considered as continuous across the transformation region. The vertical velocity jumps, preserving continuity. The lateral velocity also changes across the layer:

$$\Delta v_{\theta,\varphi}(\theta,\varphi) \approx -2\zeta(\theta,\varphi)\dot{\varepsilon}_{r\theta,r\varphi}(\theta,\varphi)\Delta z\,. \qquad \text{(III-25)}$$

Two interesting phenomena result. One is that the sign of the jump is controlled by the sign of the ambient shear strain rate. This leads to an interesting change of the mantle flow in the transition zone (between 400 and 670 km depth). Another is that one can recognize the places in the mantle where the greatest perturbations of the lateral flow occur.

For flows with a convecting cell center located in the lower mantle, the sign of the shear is similar at both transformational depths. Therefore, the velocity changes in a similar fashion. But what happens if the shear changes sign between the two slippery layers? The stream lines of this current would bend from a circular toward a square shape, so the flow would be "squashed" between the transformational depths. To investigate this, we use the same flow model with the W4a viscosity model.

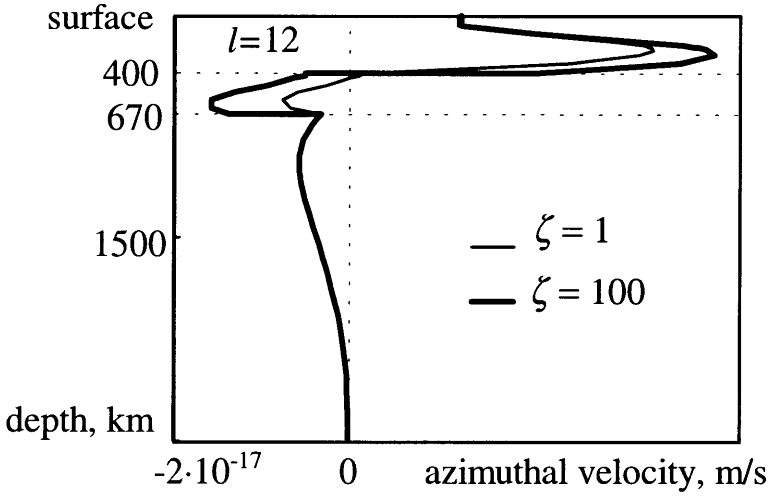

Figure III-10. Azimuthal velocity of the flow excited by a unit density anomaly of harmonic degree 12 located within the transition zone, at 525 km depth. When transformational superplasticity is included at the phase transformations at 400- and 670-km depths (thick line, ζ_{phase}=100), there are significant shears across the two-phase regions. A similar effect is observed for any wavelength flow driven by a source located within the transition zone. The discontinuity in the radial gradient of the azimuthal velocity across the transformational layer is related to an abrupt shear strain rate reduction below 670-km depth (which is proportional to the degree of lower mantle hardening assumed in the viscosity model).

Fig. 10 illustrates the effects on the azimuthal flow velocity excited by a unit density anomaly of harmonic degree 12 at 525 km depth -- within the transition zone, at a depth where we expect substantial density contrasts at this wavelength from subducted slabs. When transformational superplasticity is included at both 400- and 670-km depths, there is significant shear across the phase transitions (thick line in Fig. 10), with "plug flow" within the transition zone. The increase in lateral velocity would facilitate mixing across the two-phase regions at 400- and 670-km depths. A similar effect is observed for any wavelength flow driven by a source located within the transition zone. Note that, although the radial gradient of the azimuthal velocity is discontinuous across the transforming layer, the shear stress is still (nearly) continuous due to the compensating effect of the vertical velocity change with azimuth and the relatively small effective viscosity.

To estimate the change in the horizontal velocity field for a laterally varying viscosity reduction, we calculate the shear strain rate components for the mantle model described in the previous section and substitute them, together with the TS field (as in Fig. 9), into the boundary conditions (25). By this we assume that the deviatoric stress and the radial velocity at each wavelength are only slightly affected by the TS-induced coupling. Fig. 11 shows the map of the lateral velocity near 670-km depth, with the maximum arrow length equal to 2 cm year^{-1}. The black arrows show the direction and the amplitude of the horizontal velocity just above the 1-km thick transformational region and the gray arrows show them just below the region.

Significant changes in the horizontal velocity are observed over the major up/downwellings (such as the East Australia, South America, and South Alaska downwellings, and the North Atlantic and South Africa upwellings) in Fig. 11. To interpret this, we combine eqs. (24) and (25) and obtain the result that the absolute vertical rate of the current defines the largest magnitude, and the ambient stress determines the sign of the lateral velocity change:

$$\Delta v_{\theta,\varphi} \propto \mathrm{abs}\left\{v_{\mathrm{rad}}\right\}\mathrm{sign}\left\{\dot{\varepsilon}_{r\theta,r\varphi}\right\}.$$

Note that, in contrast to a single-wavelength flow, in the multi-wavelength flow the shears are non-zero where the current is vertical. Given slab trajectories depicted by regional seismic tomography, it might be possible to relate the change in the dip angle to the amplitude of the softening inside the transformational region.

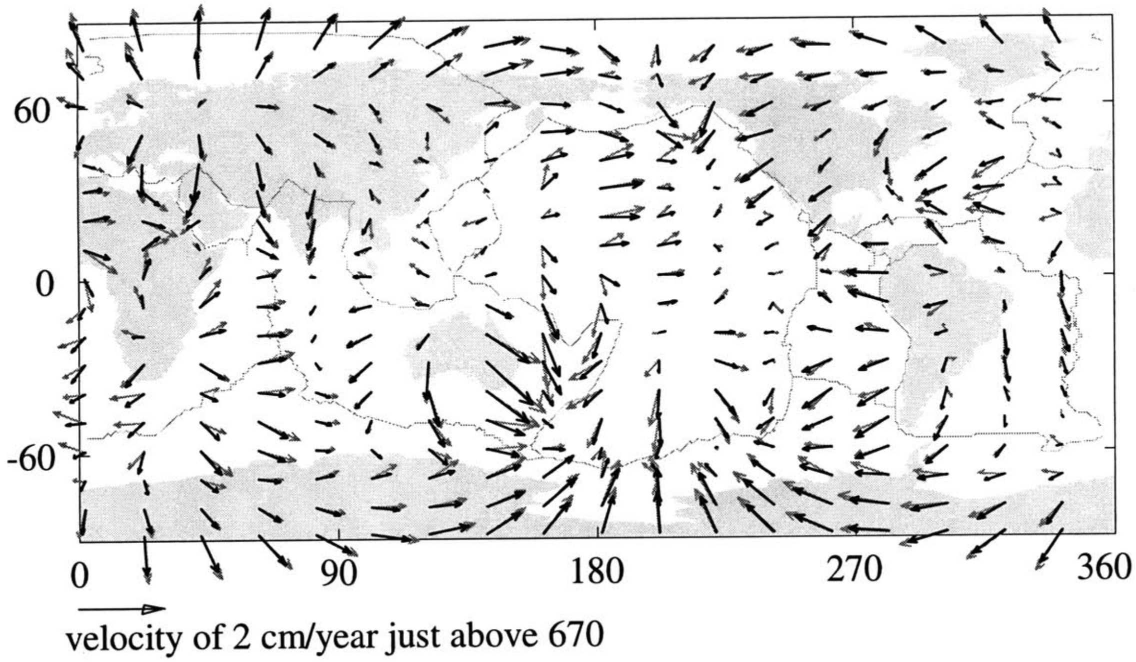

Figure III-11. Map of lateral flow velocity across the 670-km transition for a compressible mantle flow model with W4a viscosity, with lateral density contrasts inferred from a global seismic tomography model (see text for references), and the TS field as in Figure 9. The maximum arrow length equals 2 cm/year. The black arrows show the direction and the amplitude of the horizontal velocity just above the 1-km thick transformation region and the gray arrows show the azimuthal velocity just below the region. Large changes in horizontal velocity are observed over the major up/downwellings (such as the East Australia, South America, and South Alaska downwellings, and the North Atlantic and South Africa upwellings).

TS effect on the geoid

Geoid anomalies are affected by TS through a change in the dynamic topography at the surface and the core-mantle boundary. In general, the presence of thin low viscosity layers in the upper mantle facilitates turning of the flow in the vicinity of the surface, acting like a distributed zone of low viscosity. The inclusion of TS shifts the long-wavelength geoid kernels to more positive values (thick lines in Fig. 12). The situation reverses for short-wavelength sources (e.g., $l=12$) when the center of a convecting cell is above the low viscosity layer; the geoid kernels shift to the left (Panasyuk *et al.* 1996). Fig. 12 illustrates the effect on geoid kernels at degree 2, 5, and 12 for a compressible mantle model with the W4a viscosity profile.

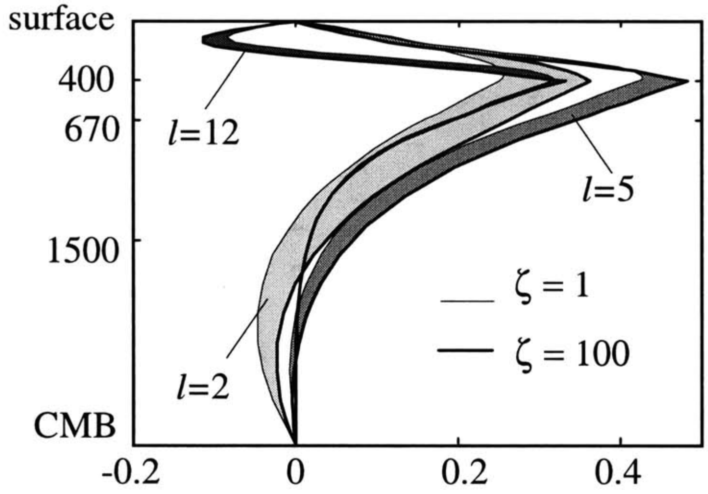

Figure III-12. Geoid anomaly kernels for a compressible mantle model with W4a viscosity. The inclusion of TS at phase transformations at 400- and 670-km depths shifts the geoid kernels to more positive values with the shaded area showing the change in kernels as ζ_{phase} increases from 1 (thin lines) to 100 (thick lines). The situation reverses for the short wavelength sources (e.g., *l*=12); when the center of a convecting cell is above the low viscosity layer, the geoid kernels shift to the left, as ζ_{phase} increases from 1 to 100.

The effect of the reduction of viscosity by a factor of 100 in 1-km thick layers at 400- and 670-km depths on the long-wavelength geoid is comparable to the effect of increasing the viscosity of the lower mantle by 50 per cent. The effect on the short-wavelength geoid is similar to extending the boundaries of the upper mantle low-viscosity zone down to 450-km depth.

SUMMARY

We present quantitative and qualitative analyses of the transformational superplasticity (TS) phenomenon applied to creeping mantle material undergoing a solid-solid phase transformation with a density change. To accommodate the volume change, there must be a reshaping of the frame-supporting grains. We relate the corresponding deviatoric strain rate of the reshaping grains to the macroscopic dilatational strain rate of the entire aggregate and show that the transformational strain rates can exceed the dilatational ones by an order of magnitude.

We calculate the degree of the effective viscosity reduction for mantle material within the two-phase regions at 400 km and 670 km depths. We estimate that the mantle becomes softer by one to two orders of magnitude in the power-law (n=3) regime. The viscosity reduction would be even more significant in a low tectonic stress environment, where the relatively high transformational strain rates and stresses alone control the effective viscosity of mantle material. In the diffusional creep regime the granularity of the new phase defines the degree of softening, ranging from none to a factor equal to the number of nucleation sites per dissolving grain. Applying the same approach to the phase change at 670-km, we estimate that mantle viscosity falls by two orders of magnitude or more due to the larger volumetric strain rates observed across that phase change region and the lower tectonic strain rates due to the higher viscosity of the non-transforming, ambient mantle material.

The magnitude of transformational superplasticity varies with the pattern and vigor of mantle flow. The lateral variations in TS-magnitude introduce a coupling between flows of different wavelengths. We use a flow model for a compressible Earth, a seismic tomography-based density model and a viscosity structure supported by geoid studies to calculate the TS-field inside the 1-km-thin phase transformation layer at 670 km depth. On average, the viscosity decreases by two orders of magnitude. The TS-field varies by one order of magnitude at intermediate-to-long wavelengths. However, there are regions where TS is 1 to 3 times its mean, and a few spots where it reaches 3 to 5 times its mean. Being related to the magnitude of the radial flow, TS fluctuates at half of the flow-dominant wavelength, increasing the significance of short wavelength variations. The locations of the biggest viscosity reductions roughly correlate with the major up- and down-wellings of the flow.

The presence of the thin soft layers causes an abrupt change in the lateral velocity of the flow. Depending on the position of the driving density anomaly relative to 400- and 670-km depths, the corresponding currents are refracted by the two transformational regions in a similar or an opposite fashion. Density anomalies inside the mantle transition zone develop a "plug flow" within the zone. When compared to the flow speeds at the same location, the lateral velocity variations across the thin phase change region are 10 to 20 percent nearly everywhere in the mantle. However, the biggest refraction by the slippery layers is observed within the major up- and down-wellings.

We also show that incorporation of transformational superplasticity changes the geoid. The effect on the long-wavelength geoid is comparable to a 50% stiffening of the lower mantle, and the effect on the short-wavelength geoid is similar to an extension of the upper mantle low-viscosity zone down to 450-km depth.

Based on the analysis conducted, we speculate on some other possible effects of transformational superplasticity on the behavior of mantle material and the flow pattern. We hypothesize that the TS phenomenon may help to explain the difference in the character of tomographic mantle models across the region at 670-km depth and the richness of slab structure revealed by regional tomographic models.

The greatly increased strain rates inside the transformational region would facilitate the mixing (stirring) of temperature and compositional heterogeneities carried by the flow. The small vertical scale of the enhanced strain-rate area eases the breaking down of the heterogeneity length scale. The fact that the TS-effect is maximum in the areas of intense vertical motion suggests that it facilitates mixing most in these regions.

ACKNOWLEDGMENTS

We thank Slava Solomatov for beneficial and constructive discussions on the kinetics of phase transformations, Rick O'Connell for stimulating questions which led to the extension of the geometry section, and Shun Karato for his critical review, which helped to clarify the manuscript significantly. Financial support was provided by NSF Grant EAR95-06427. SVP is grateful to her family, Alexander and Sanya, for the uplifting emotional support and patience.

REFERENCES

Benz, H.M. & Vidale, J.E., 1993. Sharpness of upper-mantle discontinuities determined from high-frequency reflections, *Nature*, **365**, 147-150.

Dziewonski, A.M. & Anderson, D.L., 1981. Preliminary reference Earth model, *Phys. Earth planet. Inter.*, **25**, 297-356.

Edington, J.W., Melton, K.N. & Cutler, C.P., 1976. *Superplasticity*, Progress in Material Science, **21**, pp. 61-158, Pergamon Press, Oxford.

Engdahl, E.R. & Flinn, E.A., 1969. Seismic waves reflected from discontinuities within Earth's upper mantle, *Science*, **163**, 177-179.

Forte, A.M., Dziewonski, A. & Woodward, R.L., 1993. Aspherical structure of the mantle, tectonic plate motions, nonhydrostatic geoid, and topography of the core-mantle boundary, *Am. Geophys. Un., Geophys. Mon.*, **72**, 135-166.

Frost, H.J. & Ashby, M.F., 1982. *Deformation-mechanism maps. The plasticity and creep of metals and ceramics,* Pergamon press, Oxford.

Grand, S.P., 1994. Mantle shear structure beneath the Americas and surrounding oceans, *J. geophys. Res.*, **99**, 11,591-11,621.

Green, H.W., Young, T.E., Walker, D. & Scholz, C.H., 1992. The effect of nonhydrostatic stress on the $\alpha \rightarrow \beta$ and $\alpha \rightarrow \gamma$ olivine phase transformations, in *High-Pressure Research: Application to Earth and Planetary Sciences*, pp. 229-235, ed. Syono, Y. & Manghnani, M.H., TERRAPUB, Washington, D.C.

Greenwood, G.W. & Johnson, R.H., 1965. The deformation of metals under small stresses during phase transformations, *Proc. Royal Soc.*, A, **283**, 403-422.

Hager, B.H. & Clayton, R.W., 1989. Constraints on the structure of mantle convection using seismic observations, flow models, and the geoid, in *Mantle Convection*, pp. 657-763, ed. Peltier, R.W., Gordon and Breach, New York, NY.

Hager, B.H. & Richards, M. A., 1989. Long-wavelength variations in Earth's geoid: physical models and dynamical implications, *Philos. Trans. R. Soc. Lond.*, A, **328**, 309-327.

Handy, M.R., 1994. Flow laws for rocks containing two non-linear viscous phases: a phenomenological approach, *J. Struct. Geol.*, **16**, 287-301.

Karato, S., 1989. Defects and plastic deformation in olivine, in *Rheology of Solids and of the Earth*, pp. 176-208, ed. Karato, S. & Toriumi, M., Oxford University Press, Oxford.

Kot, R.A. & Weiss, V., 1970. Transformation plasticity in iron-nickel alloys, *Metall. Trans.*, **1**, 2685-2693.

Lees A.C., Bukowinski, M.S.T. & Jeanloz, R., 1983. Reflection properties of phase transition and compositional change models of the 670-km discontinuity, *J. geophys. Res.*, **88**, 8145-8159.

Maehara Y. & Langdon, T.G., 1990. Review superplasticity in ceramics, *J. Mater. Sci.*, **25**, 2275-2286.

Masters, G., Johnson, S., Laske, G. & Bolton, H., 1996. A shear velocity model of the mantle, *Philos. Trans. R. Soc. Lond.*, A, **354**, 1385-1414.

Meike, A., 1993. A critical review of investigations into transformation plasticity, in *Defects and Processes in the Solid State: Geoscience Applications*, pp. 5-25, eds Bolard, J.N. & Fitz Gerald, J.D., Elsevier Science Publishers B.V.

Milne, G.A., Mitrovica, J.X. & Forte, A.M., 1997. The sensitivity of GIA predictions to a low viscosity layer at the base of the upper mantle, submitted to *Earth planet. Sci. Lett.*

Morris, S., 1992. Stress relief during solid-state transformations in minerals, *Philos. Trans. R. Soc. Lond.*, A, **436**, 203-216.

Panasyuk, S.V., 1998. The effects of compressibility, phase transformations, and assumed density structure on mantle viscosity inferred from Earth's gravity field, Ph.D. thesis, Massachusetts Institute of Technology.

Panasyuk, S.V., Hager, B. H. & Forte, A.M., 1996. Understanding the effects of mantle compressibility on geoid kernels, *Geophys. J. Int.*, **124**, 121-133.

Paterson, M.S., 1983. Creep in transforming polycrystalline materials, *Mech. Mater.*, **2**, 103-109.

Poirier, J-P., 1982. On transformation plasticity, *J. geophys. Res.*, **87**, 6791-6797.

Poirier, J-P., 1985. Transformation plasticity, in *Creep of crystals,* pp. 213-228, Cambridge University Press, Cambridge.

Ranalli, G., 1991. The microphysical approach to mantle rheology, in *Glacial isostasy, sea-level and mantle rheology,* pp. 343-378, eds Sabadini, R., Lambeck, K. & Boschi, E., Kluwer, Boston.

Richards, P.G., 1972. Seismic waves reflected from velocity gradient anomalies within the Earth's upper mantle, *Z. Geophys.*, **38**, 517-527.

Rubie, D.C., Tsuchida, Y., Yagi, Y., Utsumi, W., Kikegawa, T., Shimomura, O. & Brearly, A.J., 1990. An *in situ* X-ray diffraction study of the kinetics of the Ni_2SiO_4 olivine-spinel transformation, *J. geophys. Res.*, **95**, 15,829-15,844.

Sauveur A., 1924. What is steel? - Another answer, *The Iron Age,* **113**, 581-583.

Sammis, C.G. & Dein, J.L., 1974. On the possibility of transformational superplasticity in the earth's mantle, *J. geophys. Res.*, **79**, 2961-2965.

Solomatov, V.S., 1995. Batch crystallization under continuous cooling: analytical solution for diffusion limited crystal growth, *Journal of Crystal Growth*, **148**, 421-431.

Solomatov, V.S. & Stevenson, D.J., 1994. Can sharp seismic discontinuities be caused by non-equilibrium phase transformations?, *Earth planet. Sci. Lett.*, **125**, 267-279.

Steinberger, B. & O'Connell, R.J., 1996. Changes of the earth's rotation axis owing to advection of mantle density heterogeneities, *Nature*, **387**, 169-173.

van der Hilst, R., 1995. Complex morphology of subducted lithosphere in the mantle beneath the Tonga trench, *Nature*, **374**, 154-157.

Whitcomb, J.H. & Anderson, D.L, 1970. Reflection of P'P' seismic waves from discontinuities in the mantle, *J. geophys. Res.*, **75**, 5713-5728.

APPENDIX

We describe here the deformation state of a reshaping grain with a nearly round geometry (Fig. 1). We approximate the reshaping as viscous flow of a 2D-circular grain of radius R which is driven by its surface motion, with velocity contrast:

$$v_\Sigma = \frac{R}{\lambda}\dot{\varepsilon}_{\mathrm{vol}}, \tag{A 1}$$

as in eq. (10), no body force is considered.

The governing equations for incompressible viscous flow are continuity: $\operatorname{div}\mathbf{v} = 0$, and motion: $\nabla\sigma = 0$, where we assume that the stress and strain rate tensors are linearly related, $\sigma = 2\eta_{\mathrm{eff}}\dot{\varepsilon}$. Since the equations are linear and the coordinate vectors are orthogonal (we use a 2D cylindrical (r,θ) coordinate system), we can separate the radial and angular variables and express the flow parameters through their Fourier expansion. Then the radial and tangential velocities can be written as:

$$v_r(r,\theta) = \sum v_r^k(r)\cos k\theta \quad \text{and} \quad v_\theta(r,\theta) = \sum v_\theta^k(r)\sin k\theta,$$

and the normal and shear stress components as:

$$\sigma_{rr}(r,\theta) = \sum \sigma_{rr}^k(r)\cos k\theta \quad \text{and} \quad \sigma_{r\theta}(r,\theta) = \sum \sigma_{r\theta}^k(r)\sin k\theta.$$

Similarly, we expand the surface velocity, v_{surf}, into a Fourier set, and approximate it by a rectangular function of period k ($k = 4$ in Fig. 4 assumes that the number of new-born B-grains is the same as A-grains, $s = N_B/N_A = 1$):

$$v_{\mathrm{surf}} \approx \sum_{k=4}^{K} a_k \cos k\theta \text{ , where } a_k = 2v_\Sigma\lambda\frac{\sin \pi k\lambda}{\pi k\lambda}, \tag{A 2}$$

(later we omit the summation limits unless they are different).

To solve for the stresses inside the grain, we use a well-developed propagator technique. Introduction of the radial-dependent vector:

$$\mathbf{u} = \begin{bmatrix} v_r^k & v_\theta^k & \sigma_{rr}^k \frac{r}{4k\eta} & \sigma_{r\theta}^k \frac{r}{4k\eta} \end{bmatrix}^{\mathrm{T}} \tag{A 3}$$

allows us to rewrite the governing equations in the form of the first-order matrix differential equation: $\frac{r\partial}{\partial r}\mathbf{u} = \mathbf{A}\mathbf{u}$, where the matrix $\mathbf{A}$ is:

$$\mathbf{A} = \begin{bmatrix} -1 & -k & 0 & 0 \\ k & 1 & 0 & 4k \\ 1/k & 1 & 1 & -k \\ 1 & k & k & -1 \end{bmatrix} \tag{A 4}$$

The solution of the system can be expressed as:

$$\mathbf{u}(r) = \mathbf{P}(r, r_0)\mathbf{u}(r_0),$$

where the propagator for cylindrical coordinates is:

$$\mathbf{P}(r, r_0) = \left(\frac{r}{r_0}\right)^{\mathbf{A}}.$$

Characteristic numbers for the $\mathbf{A}$ matrix are: $\lambda_{1,2} = \pm(k+1)$ and $\lambda_{3,4} = \pm(k-1)$.

To propagate the flow variables from one boundary to another, we write the boundary conditions at a single radius. That is, given the variables at the grain center $v_r|_{r=0} = v_\theta|_{r=0} = \sigma_{r\theta}|_{r=0} = 0$, we propagate them to the grain surface:

$$\mathbf{u}(R) = a_k \begin{bmatrix} 1 & \frac{P_{23}}{P_{13}} & \frac{P_{33}}{P_{13}} & \frac{P_{43}}{P_{13}} \end{bmatrix}^{\mathrm{T}}.$$

Calculating the propagator, we get:

$$\mathbf{u}(R) = a_k \begin{bmatrix} 1 & -\frac{k+2}{k} & \frac{(k+1)(k-2)}{2k^2} & -\frac{k+1}{2k} \end{bmatrix}^{\mathrm{T}}. \tag{A 5}$$

Now all the flow parameters can be calculated from the surface inside the grain as:

$$\mathbf{u}(r) = \mathbf{P}(r,R)\mathbf{u}(R)\,. \tag{A 6}$$

Since the flow is driven by periodic boundary conditions, and the deviatoric strain rate is zero at the grain center, the normal and shear components of the deviatoric strain rate tensor have similar radial dependence $\dot{\gamma}_k(r)$:

$$\dot{\varepsilon}_{rr}(r,\theta) = \sum \dot{\gamma}_k(r)\cos k\theta \quad \text{and} \quad \dot{\varepsilon}_{r\theta}(r,\theta) = -\sum \dot{\gamma}_k(r)\sin k\theta\,. \tag{A 7}$$

(the same is true for flow in a 2D half-space). That feature allows us to obtain an analytical solution. Defining the radial dependence of the deviatoric strain rate as: $\dot{\gamma}_k(r) = \dot{\varepsilon}^k_{rr}(r) = -\dot{\varepsilon}^k_{r\theta}(r) = -\dot{\varepsilon}^k_{\theta\theta}(r)$, we write the matrix equation for the stresses only:

$$\frac{r\partial}{\partial r}\begin{bmatrix} u_3 \\ u_4 \end{bmatrix} = \begin{bmatrix} 1 & 2-k \\ k & 2k-1 \end{bmatrix} \cdot \begin{bmatrix} u_3 \\ u_4 \end{bmatrix}. \tag{A 8}$$

Convolution of the new propagator with the boundary conditions (A 5) gives the radial component of the deviatoric strain rate:

$$\dot{\gamma}_k(r) = \frac{a_k(k+1)}{r}\left(\frac{r}{R}\right)^{k+1}. \tag{A 9}$$

The amplitude of the deviatoric strain rate is defined in terms of the second invariant of the strain rate tensor: $\dot{\gamma}(r,\theta) = \sqrt{I_2(r,\theta)}$, where the latter is defined in terms of the strain rates, $I_2 = \dot{\varepsilon}^2_{rr} + \dot{\varepsilon}^2_{r\theta}$, for a 2-D cylindrical incompressible flow (**A** 7). On the local *(r, θ)* scale, the large, sharp contrasts in the flow velocity cause high amplitudes of the strain rates, which increase the second invariant significantly. To investigate these effects on the scale of the entire grain, we calculate the amplitude of the deviatoric strain rate averaged over the grain:

$$\langle \dot{\gamma} \rangle = \frac{1}{\pi R^2}\int_0^R\int_0^{2\pi} \dot{\gamma}(r,\theta)\, r\,dr\,d\theta\,, \tag{A 10}$$

where the sub-integral expression is simplified to the following:

$$\dot{\gamma} = \dot{\gamma}_1 \sqrt{1 + \sum_{k=2}^{K} \chi_k^2 + 2\sum_{k=2}^{K-1} \chi_k \sum_{m=k+1}^{K} \chi_m \cos(k-m)\theta}\,, \tag{A 11}$$

with $\chi_k = \frac{a_k}{a_1} \frac{k+1}{2} \left(\frac{r}{R} \right)^{k-1}$ and $\dot{\gamma}_1 = \frac{2a_1 r}{R^2}$.

We calculate the integral numerically for different k and K to explore the effect of fine granularity (when the new phase develops many fine grains instead of a few coarse ones) and the effect of sharp grain edges.

To assist understanding of the numerical results, we consider a situation that allows an analytical solution. When the areas for outflow and inflow are almost equal to each other, the surface boundary load on the reshaping grain can be approximated by a monochromic function, for example, a sinusoid, with a wavenumber equal to the number of outflow areas. Then the second invariant becomes a radial function only, $I_2 = \dot{\gamma}_k^2(r)$, and by substituting eq. A 9, we simplify eq. A 10 to the following:

$$\langle \dot{\gamma} \rangle_{\text{mono}} = \frac{2a}{R} \frac{k+1}{k+2} = \frac{\pi}{2\sqrt{f_\mu}} \frac{k+1}{k+2} \dot{\varepsilon}_{\text{vol}}\,, \tag{A 12}$$

where $a = \pi v_{\text{in}}/2$. The monochromic approximation shows that the averaged deviatoric strain rate depends only weakly on the load wavelength.

Chapter IV. GRAVITATIONAL CONSTRAINTS ON THE MANTLE VISCOSITY PROFILE. [3]

INTRODUCTION

The deviations of earth's gravitational potential field from a hydrostatic pattern are due to lateral density contrasts, which are related to thermal and/or compositional variations within the planet and to the deflection of external and internal boundaries, such as the surface, the core-mantle boundary, and others related to chemical or phase changes. Over thousands of years the large-scale internal density anomalies force the mantle rocks to creep; the consequent mantle flow deflects the boundaries. The long-wavelength, non-hydrostatic geoid is highly sensitive both to the internal density distribution and to the radial stratification of mantle viscosity (Richards and Hager 1984; Ricard *et al.* 1984).

Seismic tomographic imaging of the structure of the interior (e.g., Dziewonski *et al.* 1977; Clayton and Comer 1983; Su and Dziewonski 1991; Masters *et al.* 1996; Ekstrom and Dziewonski 1996), as well as geodynamic models of slab reconstructions (e.g., Hager 1984; Ricard *et al.* 1993) allow us to estimate the density distribution within the mantle. An analytical description of mantle circulation driven by those anomalies can give an estimate of the deflections of the equipotential surfaces and the mantle boundaries (e.g. Richards and Hager 1984; Ricard *et al.* 1984; Hager and Clayton 1989; Forte and Peltier 1991; Dehant and Wahr 1991; Panasyuk *et al.* 1996). The resemblance of a modeled geoid to the observed geoid field is used as a measure of the feasibility of a proposed mantle viscosity profile (e.g. Hager and Richards 1989; Ricard *et al.* 1989; Forte *et al.* 1994; King 1995).

A viscosity stratification inferred from the gravitational fit should not be sensitive to the fitting criteria, e.g., variance reduction (e.g., Mitrovica and Forte 1997), degree correlation (e.g., Ricard *et al.* 1989), or power spectrum (Cizkova *et al.* 1996), used in the inverse method. However, several distinct viscosity profile families are found by the

---

[3] to be submitted to *Journal of Geophysical Research*, by Panasyuk, S.V., and B.H. Hager, 1998.

above mentioned inverse studies, which all satisfy observed geoid reasonably well. In order to improve the resolution of the viscosity structure, the most recent studies carry out joint inversions, where, in addition to gravity, simultaneous fits to other observables are performed, such as to seismic data (Forte *et al.* 1994), post-glacial rebound data (Mitrovica and Forte 1997), or dynamic topography estimates (Quinn and McNutt 1997). An interdisciplinary approach, assembling results of observational, analytical, and numerical studies, can bring us closer to understanding the mantle viscosity structure. However, the downside of such an approach is that to carry it out effectively, one ought to consider the reliability of the information, that is, include an error analysis of the data (measured or modeled) and an estimate of the model deficiencies.

We suggest carrying out a joint inversion, simultaneously accounting for these error sources. We identify three classes of errors, related to the density distribution (e.g., uncertainty in the seismic tomography models), to insufficiently constrained observables (e.g., dynamic topography derived from the surface topography and bathymetry after an ambiguous correction for static topography, such as the subsidence of the oceanic lithosphere and the tectosphere), and to limitations of our analytical model (e.g., absence of lateral viscosity variations). We estimate the errors for geoid and dynamic topography in the spectral domain and define a fitting criteria. A minimization function weights the squared deviation of the residual quantities with a corresponding error, so that the components with the most reliability contribute to the solution more strongly than the less well constrained ones. Following this approach, we decrease the contamination of our results by errors.

METHOD DESCRIPTION

Forward, analytical model.

We assume that mantle rocks creep slowly subject to stresses generated by rising and sinking material. Following the now standard approach (Hager and O'Connell 1981), we employ the equations of continuity and motion, the constitutive equation, which relates stress and strain rate linearly, as for a Newtonian viscous rheology (for large time and length scales). Self-gravitation is accounted for through Poisson's equation. We consider also the gradual (due to pressure) and step-like (due to solid-solid phase change) radial variations in rock density throughout Earth (Dziewonski and Anderson 1981) and the corresponding variations in gravitational acceleration (Panasyuk *et al.* 1996). In addition, we assume a uniform ocean layer overlying a free-slip Earth surface, and azimuthal symmetry of viscosity, and we consider possible softening of the deforming rocks during phase transformations (Panasyuk and Hager 1997).

We modify the previous analytical models in order to handle a continuous radial variation of mantle viscosity, together with step-like, discontinuous changes. The latter are meant to simulate major discontinuities in viscosity, which are expected to occur across phase change boundaries (Sammis *et al.* 1977). In ambient mantle of a constant solid phase, however, the effects of gradual pressure and temperature changes will lead to a continuous variation of viscosity (Ranalli 1991). Under the old formulation, to simulate continuously varying viscosity, the number of isoviscous layers within the mantle had to be increased at the cost of over-parameterization of the viscosity profile and of significant slow-down of computer calculations (see Appendix B). These become a serious problem for a highly non-linear inversion when thousands of runs are to be done, as in the case we discuss below.

The constraint of constant viscosity within a layer comes from the analytical method used to solve the matrix differential equation, the so-called matrixant, or propagator technique. This method requires an exponent matrix to be constant from the top of the layer to the bottom in order to provide permutability in subintervals (Panasyuk *et al.* 1996). We modify the mathematical representation of the governing equations and the boundary conditions, and the subsequent matrix differential equation to allow for exponential variations of viscosity within the layers (see Appendix A). The matrixant solution is still valid, because the new exponent matrixes are permutable (to the accuracy of the solution for compressible flow).

We solve the resulting system of equations with respect to ocean-mantle boundary deflection, δa, and potential anomaly, V_1, at the ocean surface (see Appendix A). By definition, the Green's function, $V_1(r,l)$, represents a gravitational potential disturbance at the earth's surface caused by a unit density anomaly of degree l within a layer of unit thickness located at radius r. To obtain the geoid anomaly field, δN, or its spherical harmonic expansion coefficients, we convolve the potential Green's function with the density perturbations, D_{lm}, over the radius, and approximate the integral by the sum:

$$\delta N_{lm} = \frac{1}{g_{\text{sur}}} \int_{\text{cmb}}^{\text{omb}} V_1(r,l) D_{lm}(r)\,dr \approx \frac{1}{g_{\text{sur}}} \sum_{i}^{I} V_1(r_i,l) D_{lm}(r_i) \Delta r_i \,, \tag{IV- 1}$$

where the summation is done over I-propagation layers of thickness Δr_i centered at radius r_i (the notation is consistent with Panasyuk *et al.* 1996, unless stated differently). The number, I, and the distribution of layers is chosen to provide a sufficient accuracy of the minimization function (see an example in Appendix B). The lateral density anomaly is expanded in a spherical harmonic set:

$$D(r,\theta,\varphi) = \sum_{lm} D_{lm}(r) \mathrm{Y}_{lm}(\theta,\varphi)\,,$$

where the D_{lm} coefficients can be obtained from a tomographic model of seismic velocity anomalies, dv/v:

$$D_{lm}(r) = \frac{d\ln\rho}{d\ln v}\left(\frac{dv}{v}\right)_{lm} \rho \ . \tag{IV- 2}$$

The conversion factor, $d\ln\rho/d\ln v$, depends on the type of seismic velocity (e.g. v_p or v_s), temperature, pressure, and the compositional state of the mantle, and usually on the type of tomographic inversion. However, due to the large uncertainties of these dependencies, we consider only its radial variation, approximated as constant within three layers: 0-220, 220-670, and 670-2891 km depth range. The density anomaly field can also be derived from a geodynamic model tracking slabs and reconstructing their trajectories within the mantle. In that case, we consider the scaling factor as the density contrast between the slab and the ambient mantle.

The forward solution described above provides us with the predicted geoid anomaly at the surface, δN, and the dynamic topography at the ocean-mantle boundary, δa, (with the density jump across it given by $\Delta\rho^a$). These two fields are to be compared with the observed ones during the inversion. The gravitational potential field is provided by satellite geodesy (GEM-L2, Lerch *et al.* 1983). To obtain the non-hydrostatic geoid, we correct the observed geoid for $J_{20}=1072.618\cdot10^{-6}$ and $J_{40}=-1.992\cdot10^{-6}$, according to Nakiboglu, 1982 (assuming zero uncertainty associated with the correction). The dynamic topography field is unavailable for direct measurement; therefore, we derive the surface undulations from the observed topography and bathymetry by correcting for the deformations due to static loads (see Chapter V). Since the resulting dynamic topography refers to the deflection of the air-mantle boundary (with the density jump across $\Delta\rho^e+\Delta\rho^a$), we correct for the difference in density across the boundaries and obtain the spherical harmonic coefficients for the dry-planet dynamic topography by convolving with the density anomaly:

$$\delta T_{lm} = \frac{\Delta\rho^a}{\Delta\rho^e + \Delta\rho^a} \sum_i \delta a(r_i, l) D_{lm}(r_i) \Delta r_i \, . \qquad \text{(IV- 3)}$$

The predicted fields, δN_{lm} and δT_{lm} , and the model parameters, such as viscosity and velocity-to-density (or trajectory-to-density) conversion factor, are used for setting up the inverse problem discussed below.

Inverse problem

Traditionally, an inverse problem deals with the minimization of a multivariable function which determines the fitting criteria. Some of the previous studies utilized the reduction of variance between the two fields (e.g., Hager and Clayton 1989; Mitrovica and Forte 1997; Forte *et al.* 1994; King 1995), or the increase in degree correlation (Ricard *et al.* 1989), or the resemblance to slope of the geoid spectrum (Cizkova *et al.* 1996). However, none of the mentioned methods takes into account the errors associated with the forward and inverse problems.

We suggest using a minimization function which weights the misfit of a quantity by an error related to the uncertainty of measuring, observing, and modeling this quantity. Such a treatment makes the fit to a well-determined parameter much more important than the fit to a poorly resolved one. In the case of a joint inversion, when the fit is performed to two or more quantities simultaneously, the minimization function is determined for each quantity separately, and their sum is minimized. For example, when we perform a joint inversion for the viscosity profile (see Results section later) based on the fit to the geoid and the surface dynamic topography, we minimize a function in the spectral domain:

$$f^2 = f_{\mathrm{geoid}}^2 + f_{\mathrm{topo}}^2 . \qquad \text{(IV-4)}$$

The fitting criteria for any of these fields, say an F-field, is:

$$f_{\mathrm{F}}^2 = \frac{1}{n_{\mathrm{F}}} \sum_{lm} \frac{\left[F_{lm}^{\mathrm{obs}} - F_{lm}^{\mathrm{mod}}\right]^2}{\sigma_{lm}^2}, \qquad \text{(IV-5)}$$

where the error includes contributions from the different error sources, $\sigma^2 = \sigma_{\mathrm{density}}^2 + \sigma_{\mathrm{obs}}^2 + \sigma_{\mathrm{model}}^2$, and the scaling factor n_{F} equals the number of lm-coefficients of the F-field for which the error is defined. The errors associated with the density anomaly distribution, $\sigma_{\mathrm{density}}^2$, reflect the uncertainty in the velocity-to-density conversion factor, the seismic anomalies, and the location and density contrast of slabs. The second type of error, σ_{obs}^2, is related to the uncertainty in an observed field, such as the geoid (or gravity, or dynamic topography). The errors $\sigma_{\mathrm{model}}^2$ contaminate the terms which are mostly affected by the incompleteness of the forward model (e.g., a short wavelength signal when lateral variations of viscosity are ignored). In cases when the errors are related to a poor spatial coverage, e.g., an estimate of the dynamic topography under the continents vs. under the oceans, one could use a minimization function in the spatial domain, where the errors are defined in a similar way as above but as a function of position.

Once we estimate the errors (see the description in the next section) and define the observed fields (see the description of a model of dynamic topography in Chapter V), we characterize the minimization function and proceed with an inversion for mantle viscosity. To perform an inversion, we use an algorithm based on a Sequential Quadratic Programming method (Matlab 5, 1997), where in order to determine the search direction, the gradients and the second derivatives are estimated numerically. The method analyzes the second derivative matrix, the Hessian, constructs a quadratic multi-parameter function and determines its minimum as a tentative solution. The Hessian is usually modified or updated until the inversion converges successfully (defined by the custom-supplied tolerance level), or aborts due to exceeding the control parameters (e.g., the number of iterations).

In order to minimize the fitting criterion function, the inversion program is allowed to vary the viscosity profile and the density scaling factor within the specified stratification and value range. To reduce the number of inversion parameters and yet achieve fast convergence and good resolution, we conducted an elaborate study altering the number and the depths of viscosity layers, choosing constant and exponential laws for viscosity variations. As a result we define nine parameters to successfully and optimally describe mantle viscosity. This parameterization is based on knowledge that the effective viscosity of the mantle can change abruptly across (Sammis *et al.* 1977) and within (Sammis and Dein 1974) the phase change regions; otherwise it varies continuously under the influence of temperature and/or pressure for a constant-phase material (Ranalli 1991). The viscosity jump across a transformation and the reduction of viscosity within the region we describe by two parameters, a total of four for the entire mantle: two for the 400-km and two for the 670-km phase boundaries. We also approximate the viscosity variation associated with the thermal boundary layers near the ocean-mantle and core-mantle boundaries with discontinuous jumps in viscosity at 75-km and 2600-km depth. Continuous variations of viscosity are generally described as an exponential function of activation energy E_a and volume V_a, pressure p, and temperature T,

$$\eta(z) = A\frac{d^{\mathrm{m}}}{\sigma^{\mathrm{n-1}}}\exp\left\{\frac{E_a + pV_a}{RT}\right\}, \qquad \text{(IV- 6)}$$

with the proportionality term related to the stress σ and grain size d dependence of the creep mechanism (Ranalli 1991). We assume that outside the phase and thermal boundaries the total radial variation of the under-exponent functions is close to linear, and the pre-exponential term changes weakly with depth (that is, is independent of stress and grain size as well). Then the viscosity can be approximated with a single exponent slope within the layer of constant phase. Under this assumption we prescribe a viscosity parameter above each inner boundary: 400-km and 670-km phase changes, and 75-km and 2600-km thermal boundaries. The viscosity of the mantle around 2500-km is taken as a reference value, with the other eight values permitted to vary during the inversion. Note that all nine parameters used to describe the viscosity profile are pinned to a particular depth level, and only their values can be changed. Such an imposed inflexibility on the viscosity stratification is based on the fairly hard constraints on the depths of phase change regions and on the existence of thermal boundary layer in the convecting mantle. The ranges for viscosity parameter variations allow but do not require reduction of viscosity within the phase transformations, or discontinuous changes across them.

The density conversion factor is kept uniform in the upper and in the lower mantle, with these two values inverted for during each solution. We chose this simple parameterization for two reasons. First, the amplitude of the conversion factor (and even its sign) is still highly ambiguous (explanation follows). The possibility of an erroneous estimate of this factor for the whole mantle increases because it is used as a multiplication term between the kernels and the seismic anomaly data (eqs 1 and 2). Therefore, varying the conversion factor spatially allows the alteration of the geoid/topography kernels and/or the density anomaly signal directly, creating numerous, mainly artificial, density disturbances within the mantle.

Although mineral physics experiments (e.g., Karato 1993; Chopelas 1992) provide some constraints on the value and variation of the $d\ln\rho/d\ln v$-factor, the conversion from velocity to density anomalies is not obvious. Besides being dependent on pressure, temperature, composition, and melt fraction in the crust and mantle, the factor also depends on the characteristics of a particular tomographic inversion, e.g., the types of seismic waves involved, the Earth reference model, and the method of inversion used. The most poorly constrained region is the top part of the upper mantle, where the effects of chemical composition (e.g., continental tectosphere, Jordan 1988) in combination with thermal variations and anelasticity obscure the interpretation of seismic anomalies. The signal visible to the seismic waves near the surface has contributions from static surface features, such as the crust and affixed lithosphere ("frozen in" oceanic lithosphere and tectosphere coupled to the continents) as well as from the features participating in convection (plates and hot ridges). Sharp horizontal heterogeneities get smeared out over larger scales and radial variations get smeared out over depths. To reduce the contamination of our results by the high uncertainty of the signal from the top part of the upper mantle and to avoid double counting the dynamic features, we make two assumptions. First, we account for the crustal and lithosphere static load in our model of dynamic topography (see Chapter V). Second, we assume that within the errors considered, the first 220-km from the surface do not contribute to the density anomaly signal (though this does not stop the top layer from participating in the mantle flow). In addition to the seismic anomaly models, we also consider a geodynamical model which identifies the slab trajectories based on the locations of earthquake epicenters. Assuming that the slabs consist of cold (and presumably heavy) material, we assign a conversion factor (similar to velocity-to-density) which equals the density contrast between the slab and the ambient mantle. These two types of density distribution models, seismic tomography and slab recovery, provide us with a wide spectrum of input data.

Error analysis

The intricate part of the approach is the way in which one estimates the errors. For statistically well-represented problems, such as seismic tomography, which deals with the thousands arrival-times of events, yet is often of poor spatial coverage, there are several successful error-analysis methods (e.g. Tarantola 1997) which help to determine a well-suited solution. However, having a dozen density distribution models, several analytical and numerical studies of convection, and a few measurements of observed fields, we suggest here a first approximation of an error analysis to be applied to the inversion for mantle viscosity problems.

Uncertainty in density anomaly distribution, $\sigma^2_{\text{density}}$

Recent developments in seismic tomography techniques, together with a growing data base and computerized methods of data processing, have made it possible to produce several elaborate models of seismic velocity anomaly distribution inside the mantle (e.g., Masters *et al.* 1996; Ekstrom and Dziewonski 1996; Grand 1996; van der Hilst *et al.* 1997). The models generally agree on the lower mantle signal (Gordon Research Conference 1996); however, the discrepancy among them grows in the more heterogeneous upper mantle. The different depths of seismic wave resolution in combination with the variety of tomographic methods and data sets are responsible for the disagreements. The conversion of seismic anomaly to density perturbation introduces additional errors. Although some authors perform an error analysis, there is still deficiency in such analysis for a major number of models, and there is no straightforward way to account for all errors.

Instead of evaluating the uncertainty in density-anomaly models, we estimate the discrepancies in the geoid and dynamic topography fields predicted by our viscous-flow approach when several density-anomaly models are used as input data. For this study we consider nineteen density-anomaly models. Ten of these are derived from ten seismic tomography models (Tanimoto 1991; Masters and Bolton 1991; Su and Dziewonski 1991; Su, Woodward and Dziewonski 1994; Master *et al.* 1996; Ekstrom and Dziewonski 1996; Grand 1994; Inoue 1990; Clayton and Comer 1984; van der Hilst *et al.* 1997). The other nine are modifications of all of the above, except the one before last, such that an upper mantle signal is replaced with the geodynamic model of slab locations (Hager 1984). The last four references above are given on a spatial grid. Since our analysis is spectral, we define the spherical harmonic coefficients of the data field by numerical integration on a sphere at each depth where data are defined. There are many differences in the way the tomography models were built and in the range of data which were used. For example, in a case of data with poor coverage over the South Pole, a regional tomography model that inverts for a signal within blocks would not resolve that area at all, whereas a global tomography inversion (e.g., the first six references) using polynomials would assign a value despite poor data coverage. To handle the gaps in the block-type models during the numerical integration, we zero them out in models 7, 8, and 10 for the depths below 220-km, and we apply horizontal and radial filtering in model 9 (Hager and Clayton 1989). To minimize the effect of the gaps in the block-type models one could invert for spherical harmonic coefficients, using the least-square technique. To ensure that the density models provide a consistent representation of the inner structure that drives the convection, we perform a test on the compatibility between the models (the description follows). Then we continue our analysis with the most coherent models and estimate the errors, based on averaging over those chosen.

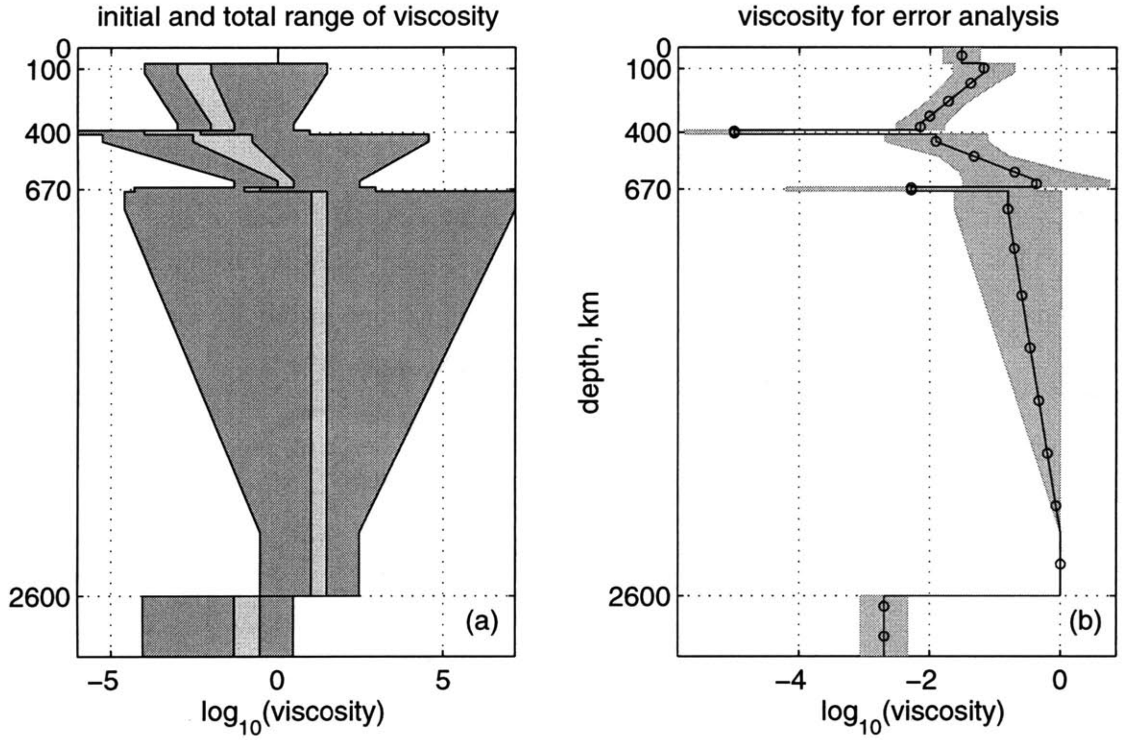

Figure IV-1. Decimal logarithm of relative mantle viscosity versus depth (km). a) Inversions are started from a randomly chosen viscosity profile constrained by the light gray shading. During the inversions, the viscosity is allowed to vary within the dark gray shading area. b) The logarithmic mean of 19 viscosity profiles chosen for the first-step of the error analysis (solid line with the circles centered at each step) and the standard deviation around the mean (gray shading).

To determine the models most compatible with each other, we complete the inversion several times for each of the nineteen density models, each time starting from randomly chosen initial values for the viscosity parameters and the density conversion factors. The initial parameter range allows roughly one order of magnitude viscosity variation (light gray shading in Fig. 1a). The conversion factor in the upper mantle is varied initially near zero (positive and negative) for the seismic models and between 100 and 200 kg m^{-3} for the hybrid models. In the lower mantle the *d*ln*ρ/d*ln*v*-factor varies between 0.1 and 0.2. The range of viscosity variations that is allowed during inversion exceeds the initial range by several orders of magnitude (dark gray shading in Fig. 1a). The *d*ln*ρ/d*ln*v*-factor can change between -2 and 2 in the upper mantle, and between 0 and 2 in the lower mantle. The slab density contrast is allowed to vary from 40 to 300 kg m^{-3}. The fitting criterion used at this stage of our analysis is the reduction of the geoid and dynamic topography variances:

$$F = \frac{\sum_{lm}\left[\delta N_{lm}^{\text{obs}} - \delta N_{lm}^{\text{mod}}\right]^2}{\sum_{lm}\delta N_{lm}^{\text{obs}\,2}} + \frac{1}{10}\frac{\sum_{lm}\left[\delta T_{lm}^{\text{obs}} - \delta T_{lm}^{\text{mod}}\right]^2}{\sum_{lm}\delta T_{lm}^{\text{obs}\,2}}. \qquad \text{(IV-7)}$$

Note, the topography variance reduction is lessened ten times relative to the one for the geoid. We apply this scaling because the dynamic topography is much more poorly constrained, as compared to the observed geoid (see observed error analysis in Chapter V).

For each of the 19 density models, we select a viscosity profile that provides the best combined variance reduction. To show the common characteristics of all 19 profiles, we calculate their logarithmic mean and plot it in Fig. 1b (the solid line with the circles centered at each step). The standard deviation around this mean is shown by the gray shade. In the next step we consider each of the selected 19 profiles as a fixed parameter and perform an inversion again for each of the models. This time, using the same fitting criterion, we allow for the free adjustment of only the density conversion factor and its jump between the upper and lower mantle. Such a choice of fixed viscosity and free conversion parameters allows us to compare the self-tuned density models against each other under otherwise equal conditions. After all inversions have converged, we obtain the 361 sets of spherical harmonic l,m-coefficients for geoid and topography fields, C_{lm}, calculated, using signals from the 19 different density distributions and the 19 fixed viscosity profiles. To estimate the dispersion of the predicted geoid and topography, we arrange the density models into a pure seismic and a hybrid group. Within each group we calculate the geoid and the topography means over the models (total of K=9 or 10 depending on the group) in the spectral domain:

$$\left\langle {}^{h}C_{lm} \right\rangle_{\text{group}} = \frac{1}{K}\sum_{k=1}^{K} {}^{h}C_{lm}^{k} \qquad \text{(IV-8)}$$

and the standard deviation (std) for each model k and each viscosity profile h (total of H=19):

$$ {}^{h}\sigma^{k2} = \sum_{lm} \left({}^{h}C_{lm}^{k} - \left\langle {}^{h}C_{lm} \right\rangle_{\text{group}} \right)^2 . \qquad \text{(IV- 9)} $$

The total of 361 standard deviations reflect the solution sensitivity to the variation of the viscosity profile, as shown in Fig. 1b for each model, and to the variation of the driving density model for each viscosity profile. To differentiate among the models, we normalize the std for each profile and model by the mean within the group for the same profile:

$$ \left\langle {}^{h}\sigma^{2} \right\rangle_{\text{group}} = \frac{1}{K} \sum_{k=1}^{K} {}^{h}\sigma^{k2} . \qquad \text{(IV- 10)} $$

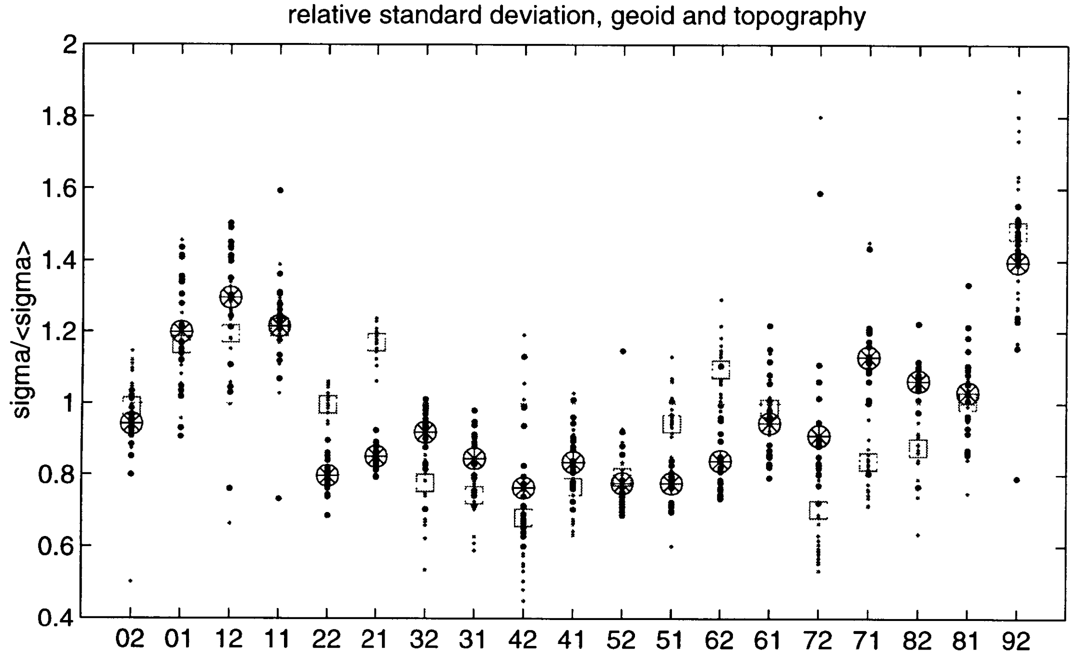

Figure IV-2. Geoid (large dots) and topography (small dots) standard deviations for each viscosity profile (total of 19 as in Fig 1b) and each density model (abscissa) normalized by the mean within a group (see text). The std averaged over the viscosity profiles is shown by wheels (geoid) and squares (topography) for each density model.

The results of the last normalization are shown in Fig. 2. For the names of the density models (abscissa) we use a two-digit abbreviation, where the first digit corresponds to the model number by order in the reference list above and the second digit corresponds to a group number: 1 is for a pure seismic model and 2 is for a hybrid model (the upper mantle signal is replaced by slabs). The ordinate corresponds to the normalized std, where large dots are for the geoid, and small dots are for the topography. Each point in the plot shows by how much the field from a particular model deviates from the mean field in units of mean deviation for a particular viscosity profile. To generalize the information over the range of viscosity profiles, we plot an std value averaged over 19 profiles for each model. The wheels (for geoid) and the squares (for topography) show the normalized standard deviation for each density model for the viscosity assemblage (such as in Fig. 1b). We define a cut-off line at a level of 1 (solid line in Fig. 2). That is, we assume that the models that produce fields within one standard deviation form a self-consistent group. Based on the selected density models, we calculate errors and use only these models for the final inversion runs.

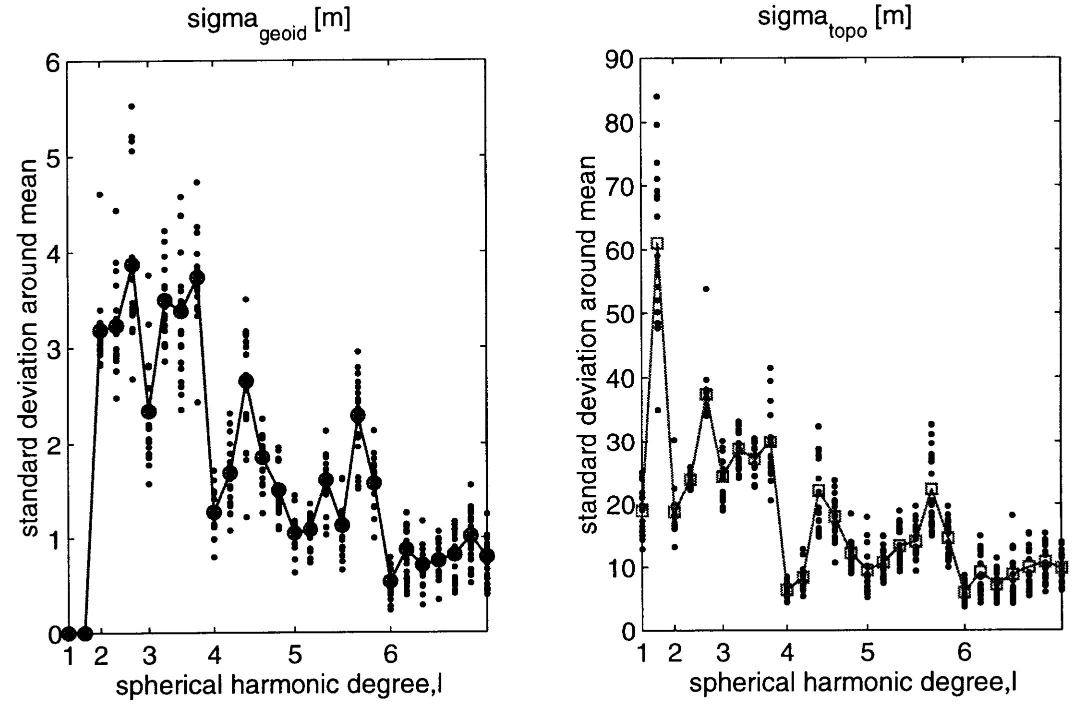

Figure IV-3. Uncertainty in the density anomaly models, geoid (a) and topography (b) in meters, versus spherical harmonic degree and order. The dots are the standard deviations for each viscosity profile (from assemblage as in Fig. 1b), and the symbols connected by solid lines are the average over the viscosity profiles.

To estimate the errors related to the variety of density models used, we calculate the standard deviation around the mean-over-models for each viscosity profile and display it in Fig. 3 by the dots versus spherical degree and harmonic number. To generalize the errors for a set of viscosity profiles, we calculate the mean-over-viscosity std as well,

$$\left\langle \sigma_{lm}^2 \right\rangle = \frac{1}{KH} \sum_{k=1,h=1}^{K,H} \left({}^{h}C_{lm}^{k} - \left\langle {}^{h}C_{lm} \right\rangle_{\text{chosen}} \right)^2 \tag{IV- 11}$$

and show its values by the solid lines (Fig. 3a is for geoid and Fig. 3b is for topography). The standard deviations calculated as above reflect the sensitivity of the different harmonics to the variations in viscosity profile (as long as there is a low viscosity zone in the upper mantle) and to the variations in the density models (as long as the models are from the chosen set). Later in the final inversions we use these errors, $\sigma_{\text{density}}^2 = \left\langle \sigma_{lm}^2 \right\rangle$ (marked by the wheels in Fig. 3a for geoid and by the squares in Fig. 3b for topography), to account for uncertainty in the density anomaly models.

Uncertainty in the observed field, σ_{obs}^2

The undulation of the gravitational equipotential surface is rather well measured by satellite gravimetry. Therefore, we could assume that any errors related to that observation are much smaller than the ones discussed above and could be ignored in the inverse problem. However, there are some relatively small geoid anomalies which are not related to the steady-state viscous mantle flow described by our approach (as in section 1). For example, the gravitational signal due to post-glacial relaxation over Hudson Bay (e.g., Simons and Hager 1997) and due to isostatically compensated crust and lithosphere (e.g., Hager 1983; Le Stunff and Ricard 1995). Although these geoid anomalies were estimated in several studies, the uncertainty relative to the signal is high owing to the variety of data and models used. Due to the relatively small and highly uncertain amplitude of the signal at the long wavelength l=2-6, at this stage of our investigation we assume that the total geoid anomalies related to post-glacial relaxation and the crustal/lithospheric formations are zero. We assume that the observational uncertainties for the geoid are equal to the spectral amplitude of a modeled geoid due to both processes. As an example of the post-glacial-relaxation geoid we adapted a model by Simons and Hager (1997). The root-mean-squared (rms) amplitude is shown by the crosses in Fig. 4a with the total non-hydrostatic geoid rms represented by the solid line.

The geoid anomaly due to the isostatically compensated crust we calculated using the CRUST5 model by Mooney *et al.* 1997 (see Chapter V). The geoid signal related to the isostatically compensated lithosphere and tectosphere were calculated using a model of oceanic floor ages by Müller *et al.* 1997 and the tectonic regionalization by Jordan 1981 (see Chapter V). The total surface-formation-geoid rms is shown by the plusses in Fig. 4a. We summed the geoid anomalies due to rebound, crust, lithosphere and tectosphere and display the rms by the circles in Fig. 4a. The significant excess of the total geoid amplitude over these observational errors for the high-amplitude harmonics justifies our earlier assumption in application to the inverse modeling.

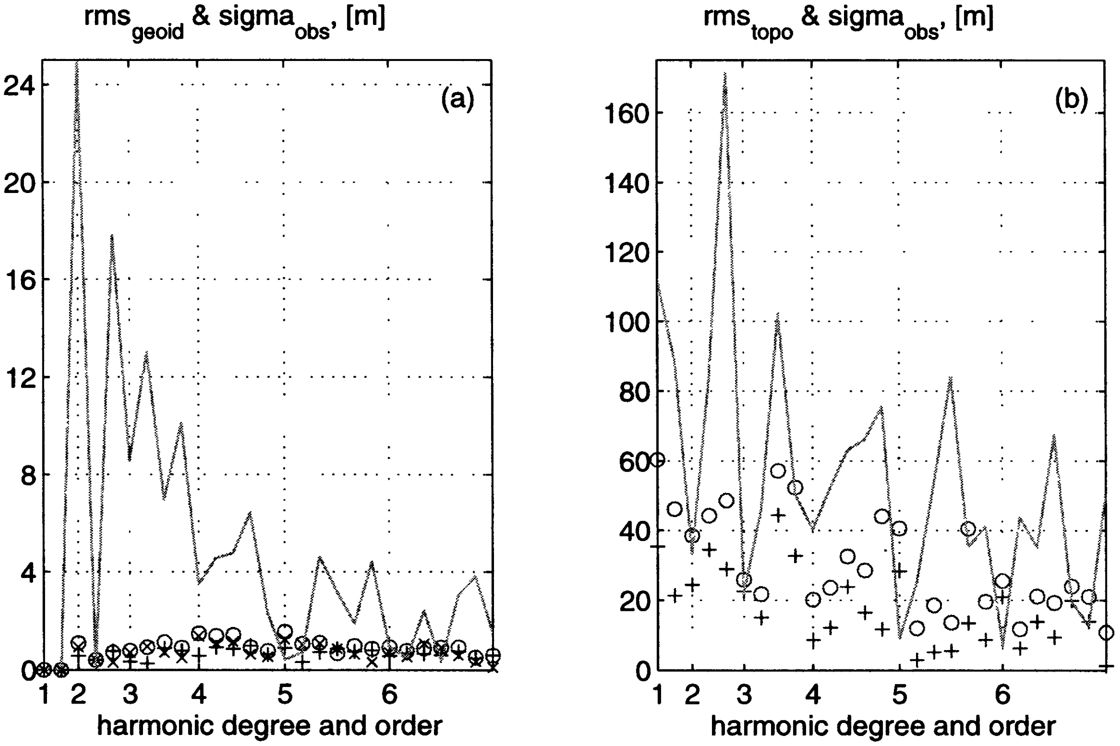

Figure IV-4. Observational uncertainty, geoid (a) and topography (b) in meters, versus spherical harmonic degree and order. The rms amplitude of the signal (solid lines) is compared with the total observational error rms (circles). Crosses represent the rms of the geoid due to post-glacial-relaxation (a), plusses are for the geoid due to static topography (a) and for errors in topography due to uncertainty in the ocean-floor-age and crust data (b).

The other observable in the geoid-topography joint inversion, dynamic topography, is not as well constrained as the geoid. The topography due to mantle-dynamics processes is distorted by the crust and the lithosphere attached to it. There are only a few measurements of the dynamic topography amplitude, such as flooding records related to the rise and fall of continents (Gurnis 1990), or the smooth topography over the oceanic basins (Parsons and Sclater 1977). To recover the frequency pattern of the dynamic topography, the observed topography and bathymetry is usually corrected for crustal thickness variations (e.g., Cazenave *et al.* 1988; Forte *et al.* 1993) and the attached lithosphere under the oceans (e.g., Marty and Cazenave 1989; Stein and Stein 1992), assuming general principles of isostasy (e.g., Love 1911).

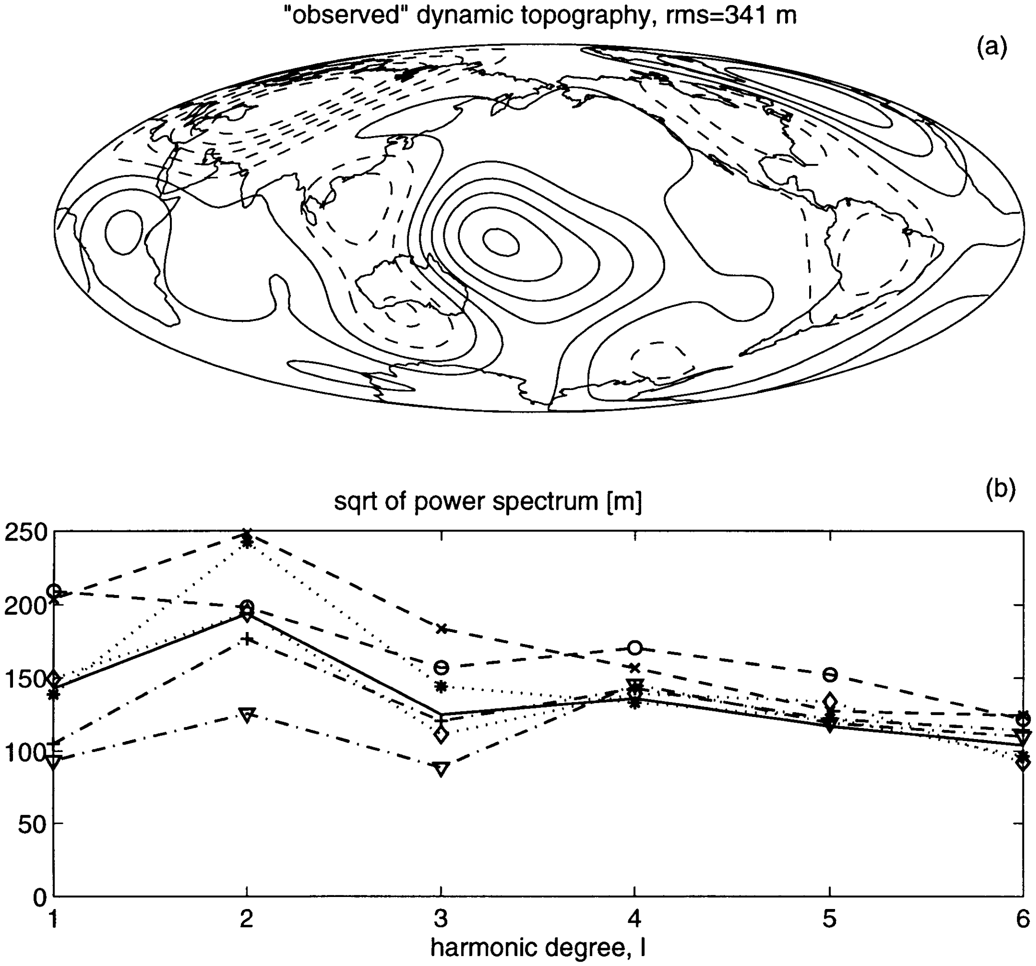

Figure IV-5. A model of "observed" surface dynamic topography of spherical harmonic degree l=1-6. The field is contoured at 200 m interval (a), solid lines are for zero and positive values, dashed lines are for negative, the field rms is 340 m. Square root of the power spectrum of a set of topography fields (non-solid lines in b) used to construct the final field (solid line in b) versus spherical harmonic degree. The assemblage (b) consists of fields built under assumptions of thin- (open symbols) and thick-plate cooling (crossed symbols), global isostasy (dashed lines), continent vs. ocean (dash-dotted lines), and shield-platform vs. ocean-orogenic zones (dotted lines) baseline leveling.

Since the ambiguity of the corrections is so high, we avoid using any particular model to retrieve the dynamic topography for inverse modeling. Rather, we follow several currently accepted approaches and analyze the contribution of the considered phenomena to the amplitude and pattern of the obtained dynamic topography (see detailed description in Chapter V). Applying combinations of the assumptions, we build several fields of dynamic topography (the spectral amplitudes are shown by the dashed, dot-dashed, and dotted lines in Fig. 5b). On the basis of this assemblage we calculate the mean long-wavelength dynamic topography field displayed in Fig. 5a, with the spectral amplitude and the rms shown by the solid lines in Fig. 5b and 4b, respectively. The total errors reflecting the scatter of all the topography fields (as in Fig. 5b) and the uncertainties in the ocean-floor-age and crustal data (crosses in Fig. 4b) are shown by the circles in Fig. 4b. Thus, the obtained dynamic topography represents the general amplitude and frequency characteristics, and it is within the errors of our understanding of the physical processes controlling the topography formation. The dynamic topography field has a maximum in the power spectrum at the second degree with a slight decrease in the power at l=1 and l=3 and a relatively strong contribution from the higher harmonics (see Fig. 5b). The depressions are associated with the European and American continents, and with the Circum Pacific. The dynamic topography (Fig. 5a) and its sigma (Fig. 4b) are used later in the final inversion runs as the "observed" dynamic topography field and the associated observational errors, $\sigma^2_{\text{obs}} = \langle \sigma^2_{lm} \rangle$. The high ambiguity has been apparent from comparing the global dynamic topography models calculated previously (e.g., Hager *et al.* 1985; Cazenave *et al.* 1988; Hager and Clayton 1989; Forte 1993). Our way of estimating and including the errors into the inverse procedure allows us to fit the general features (such as the Central Pacific and African Uplifts, or the Pacific Circum and North America lows) and their amplitudes without tying the solution to poorly constrained regions, such as questionable depressions under the all continents.

Uncertainty due to incompleteness of forward model, σ^2_{model}

Our current model treats only spherically symmetric variations of viscosity and it assumes free-slip boundary conditions at the surface. However, lateral variations in viscosity (LVV) are undoubtedly present due to temperature, composition, and deviatoric stress variations within the mantle. Closer to the surface, they become critically high due to the change of mantle rheology from viscous to elastic, and to brittle within the plates. The essentially rigid plates, driven by mantle flow, act back on the flow, maintaining their integrity and geometry. Having relatively weak boundaries, a plate causes a toroidal flow of the mantle. Thus, the density-driven poloidal flow is coupled to the plate-driven toroidal flow, and the resulting, total flow creates the dynamic topography and determines the gravity field. Therefore, our assumptions are justified to only some extent, and they restrict us from explaining the part of geoid and topography signal related to the lateral viscosity variations, the toroidal flow, and the surface plate-like behavior. On an optimistic note, however, we recognize that for the long-wavelength flow these effects are of second order compared to those due to changes in radial-viscosity structure. Thus, instead of elaborating our model, at this point, we attempt to estimate the maximal errors in geoid and dynamic topography due to ignoring such effects, based on different studies of the above mentioned phenomena.

In earlier studies, the observed equal poloidal/toroidal energy partitioning at the surface (Hager and O'Connell 1978) was directly related to the plate-like surface division (O'Connell *et al.* 1991; Olson and Bercovici 1991), and plates were incorporated into models (Hager and O'Connell 1981; Ricard and Vigny 1989; Gable *et al.* 1991; Forte and Peltier 1991). The importance of the poloidal-toroidal coupling on dynamic surface topography and the geoid was pointed out (Forte and Peltier 1987), and later investigated analytically and numerically (Richards and Hager 1989; Christensen and Harder 1991; Ribe 1992; Zhang and Christensen 1993; Cadek *et al.* 1993; Forte and Peltier 1994). Although each approach above analyzes the effects of LVV and boundary conditions by different means, there are some general points they agree upon. For example, the effects are much stronger when the viscosity of the mantle increases with depth compared to the isoviscous case. The strongest effects on the flow (and hence surface deformation and geoid) are produced by the self-coupling between the density source and the viscosity anomaly and by the coupling at the doubled harmonics. The relative effect is stronger for the higher harmonics. We realize that evaluation of the error amplitudes is very ambiguous; however, we attempt an estimate for the low harmonics (l=1-6). Richards and Hager (1989), based on the results of perturbation theory and numerical models of mantle convection, concluded that the longest wavelength geoid anomalies (l=2,3) are not seriously contaminated, however, for the higher degrees ($l \geq 4$) the effect could be significant due to coupling between density heterogeneity and viscosity variation. They showed that the self-coupled anomalous surface deformation and the anomalous geoid behave as l^2 and estimated an anomalous geoid, in percent, as a function of the load/viscosity mode number for different strengths of viscosity variations. The size of the effect increases linearly with the wave number for the geoid due to its l-dependence on the load. We use this result as an estimate of the geoid and topography errors:

$$\sigma^{\text{geoid}}_{\text{model}}(l) \propto l \sum_m \delta N^{\text{mod}}_{lm} \quad \text{and} \quad \sigma^{\text{topo}}_{\text{model}}(l) \propto l^2 \sum_m \delta T^{\text{mod}}_{lm} \, . \qquad \text{(IV- 12)}$$

To account partially for the higher order coupling, we doubled the errors at l=2, 4, 6.

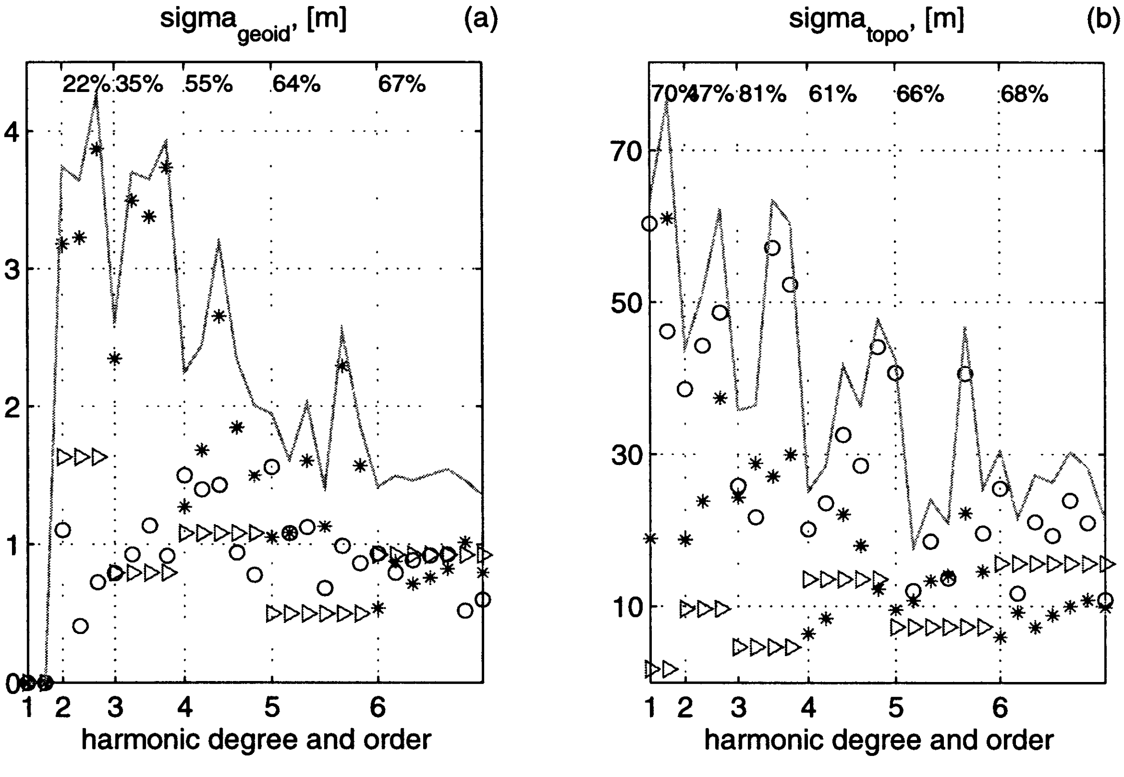

Figure IV-6. The total error (solid line), geoid (a) and topography (b) in meters, versus spherical harmonic degree and order. Three types of errors are show: the density model uncertainty (stars), the observational error rms (circles), and the modeling errors (triangles). The numbers on the top show the percent of the harmonic degree error relative to the total signal amplitude of the same harmonic.

To show the contribution of each error type to the total errors assigned with the geoid and dynamic topography during the inversion, we plot individual errors together with the total error in Fig. 6 (stars are for density model errors, circles are for observational errors, triangles are for the model deficiency, and the solid line is for the total error). For the geoid field the density-model-related errors dominate strongly (Fig. 6a). The total error is on the order of 20 per cent of the observed geoid rms for long wavelengths, increasing to about 50-70 per cent for the shorter wavelength signals. For the topography field the observational errors define most of the total error (Fig. 6b). The least resolvable features of topography are at $l=1$, 3, where the uncertainty reaches 70-80 per cent. For other harmonics, the errors vary between 50 per cent and 70 per cent of the signal.

RESULTS OF THE INVERSION

We performed an inversion based on a simultaneous fit to the geoid and dynamic topography, defined by the criterion in eqs 4 and 5. The observed geoid was obtained from the spherical harmonic expansion data (Lerch *et al.* 1983) by the removal of the hydrostatic deflections (Nakiboglu 1982). The observed dynamic topography was reduced from the surface topography and bathymetry by correcting for the crust and lithosphere (see Chapter V). The errors associated with the geoid and dynamic topography modeling were taken as in Fig 6. We inverted for the viscosity profile and the density conversion factor. The mantle viscosity was parameterized in five layers. Three layers were assumed to consist of a constant-phase material with the viscosity changing continuously by an exponential law. The other two layers simulate the thermal boundary layers, lithosphere and D", and were assigned a constant viscosity within and a jump in viscosity at their borders. The viscosity within the phase transformation regions (400 and 670 km depths) was allowed, but not required, to drop in magnitude relative to the ambient mantle. The density conversion factor was set free to adjust its constant value within the upper and the lower mantle during all runs of the inversion. The density anomaly models used are those which fall under the cut off line in Fig. 2. To make sure that the final results do not depend on the initial values of the parameters, each time we started the inversions from randomly (uniform distribution) chosen initial conditions within the assigned range (see light gray area in Fig. 1a). During the inversion, the parameters are allowed to vary within a range of several orders of magnitude (dark gray area in Fig. 1a). To gain a statistically significant result, we carried out tens of inversion runs for each of the density models.

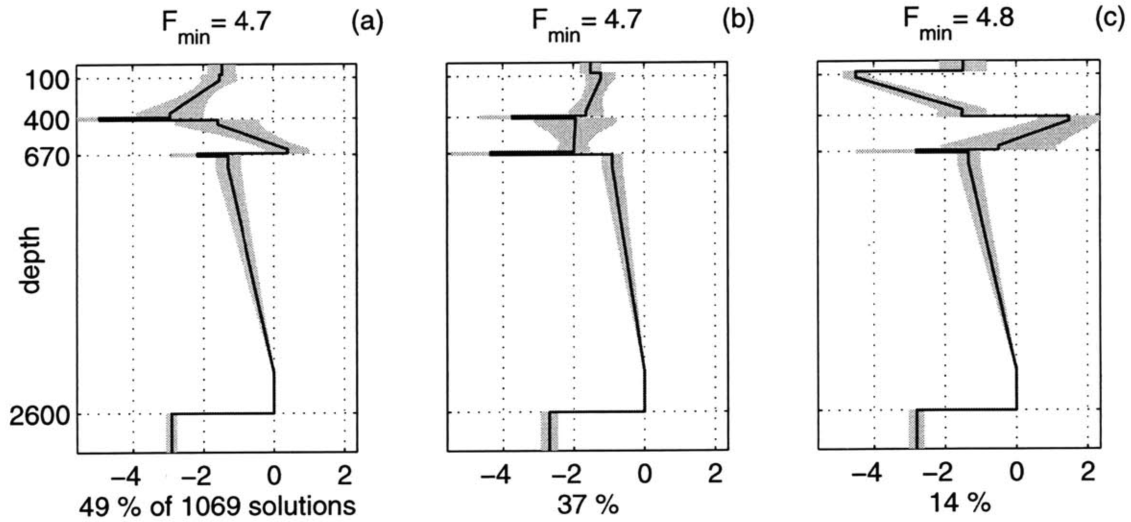

Figure IV-7. Three families of mantle viscosity profiles (decimal logarithm relative to the viscosity at 2500 km depth) versus depth (km). The weighted average (solid line), the standard deviation (shaded area), and the weighted minimization function F_{min} are shown for the first (a), second (b), and third (c) family.

All inversion runs successfully converged. The solutions formed three families of viscosity profiles (see Fig. 7a-c, where we plot the logarithm of normalized viscosity versus depth). Since the solutions scatter within each family, we calculate the logarithmic average of the viscosity profiles, where each term is weighted by the inverse of its minimization function value, *f* (solid lines in Fig. 7). Therefore, the solutions with the best fit to the observables contribute more to the representative profile. The standard deviation of all the participating solutions from the weighted average is shown by the gray area around the solid line (each squared std was weighted correspondingly). Each group of solutions in Fig. 7 can be distinguished by the depth of the low-viscosity zone (LVZ) in the upper mantle, clearly identified by the peak in the geoid kernels (Fig. 8). Almost all of the viscosity profiles have a significant viscosity drop within one or both phase-change regions, and display an increase of viscosity within the lower mantle down to 2600-km depth, followed by a soft layer above the CMB.

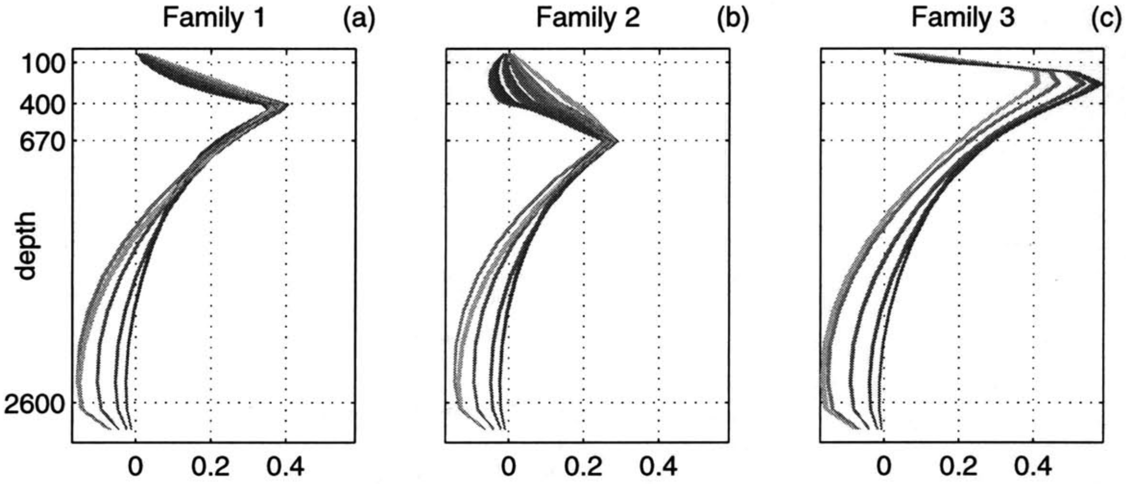

Figure IV-8. Geoid kernels for spherical harmonics l=2-6 corresponding to the three families of mantle viscosity profiles (as in Fig. 7). For clarity, only one fifth of the standard deviation around the weighted average is shown. The darkness of the shading increases for the shorter wavelengths.

To show the general trend in the geoid/topography kernels of each family, we calculate a representative geoid/topography kernel for each l weighted by the minimization function of the solution. The weighted standard deviation when plotted around the representative line overlaps for most harmonics. To maintain a clear presentation of the results, we plot only one fifth of the std around each representative kernel and plot the area with the shading getting darker toward the higher harmonics.

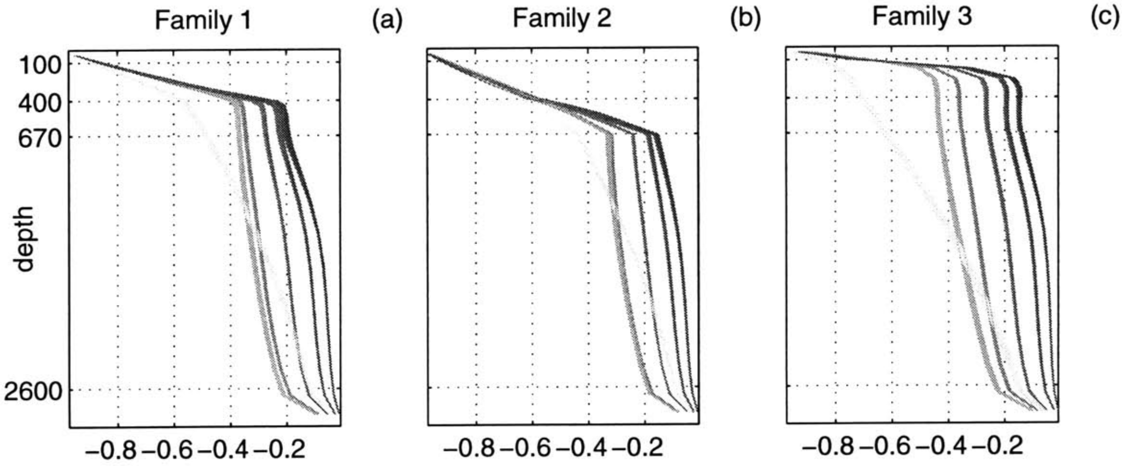

Figure IV-9. Surface dynamic topography kernels for spherical harmonics *l*=2-6 corresponding to the three families of mantle viscosity profiles (as in Fig. 7). For clarity only one fifth of the standard deviation around the weighted average is shown. The darkness of the shading increases for the shorter wavelengths.

The most popular family (half of all solutions) has a LVZ centered at the 400-km phase change region (Fig. 7a). The geoid kernels peak with a positive value at this depth (Fig. 8a). The surface dynamic topography kernels are nearly linear from the surface to the LVZ-depth and decrease gradually down to D", from where they diminish to zero at the CMB (Fig. 9a). The next family of viscosity profiles (more than one third of all solutions) has an exponential decrease in viscosity from the surface down to the 670-km phase change region (Fig. 7b). The geoid kernels peak at 670-km depth, but in contrast to the first family, they have negative values in the top part of upper mantle in addition to the lower half of mantle (Fig. 8b). The topography kernels are almost linear from the surface to the LVZ depth, and stay nearly constant throughout the lower mantle down to D" (Fig. 9b). The final group of viscosity profiles (a little over 10 per cent of all solutions) has a LVZ right under the lithosphere with an increase of viscosity to 400-km, followed by a decrease to 670-km (Fig. 7c). The geoid kernels reach maximum values in the top of upper mantle and cross over to negative values around mid-mantle (Fig. 8c). The topography kernels decrease sharply within the first 200 km, and then fall linearly to zero at the CMB (Fig. 9c).

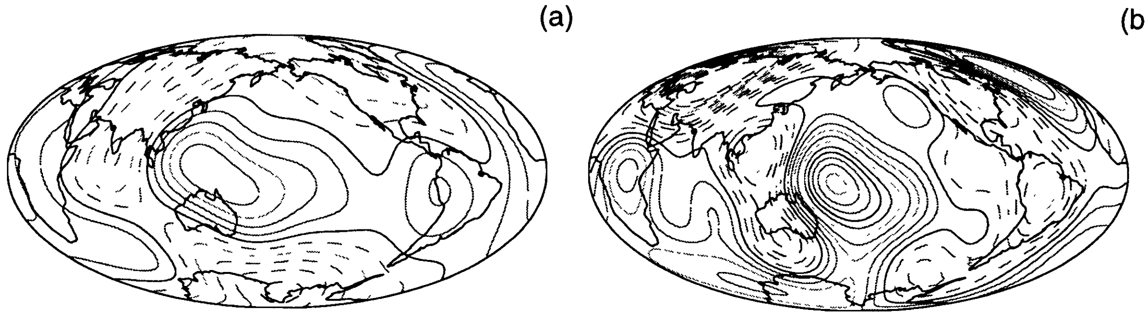

Figure IV-10. The observed geoid (a) and surface dynamic topography (b). The contour levels are 20 m (geoid) and 100 m (topography). Zero and positive values are solid lines, negative contours are shown by the dashed lines.

To analyze the spatial characteristics of the geoid and topography fields obtained, we calculated *f*-weighted mean fields within each solution-family and display the results in Figs 11-13 (geoid is on the left and topography is on the right). For comparison, we also show the observed geoid and the dynamic topography.

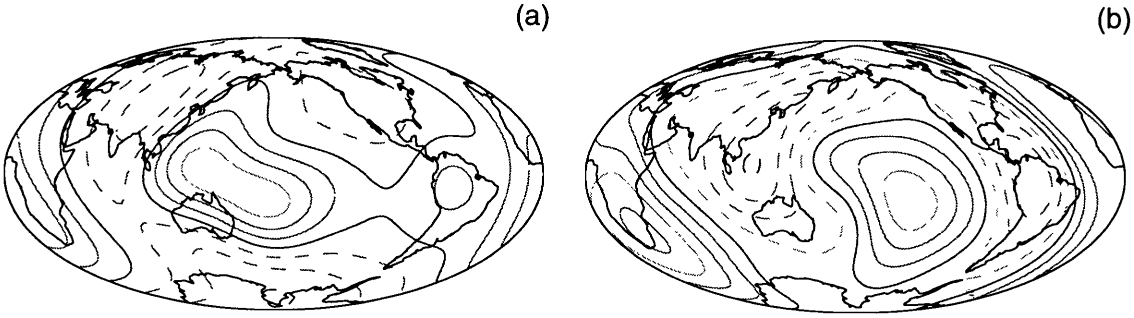

Figure IV-11. The geoid (a) and surface dynamic topography (b) fields corresponding to the first family (as in Fig. 7a). The contour levels are as in Fig. 10. Field characteristics: variance reduction, VR_{geoid}=83% and VR_{topo}=20%, degree correlation, DC_{geoid}=93% and DC_{topo}=46%, minimization function, F_{min} =4.7, and rms_{ttopo}= 193 m.

The first (Fig. 11) and the second (Fig. 12) solution-families produce similar minimization function fit values, *f*=4.7. However, the geoid variance reduction and degree correlation in the first family (VR=83%, DC=93%) exceed those of the second family (VR=79%, DC=90%) providing obviously better resemblance to the observed field (compare Fig. 11a and Fig. 12a to Fig. 10a). The fit of the topography fields is relatively poor, with the better fit for the second family (VR=20% and DC=46% for the first family versus VR=38% and DC=62% for the second family).

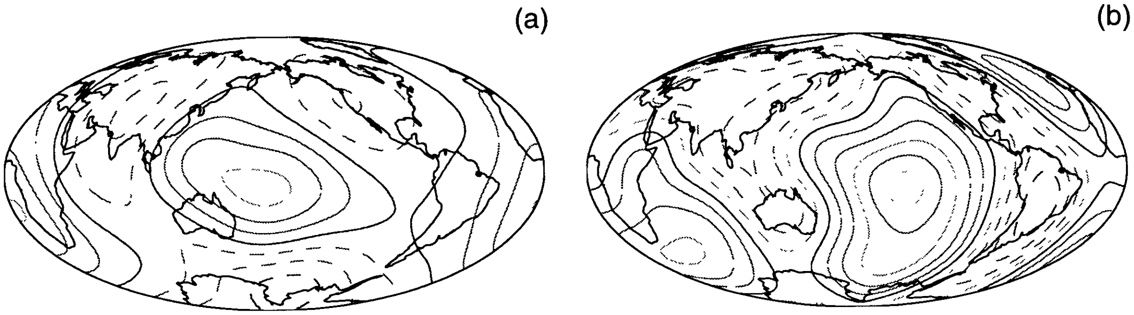

Figure IV-12. The geoid (a) and surface dynamic topography (b) fields corresponding to the second family (as in Fig 7b). The contour levels are as in Fig. 10. Field characteristics: variance reduction, VR_{geoid}=79% and VR_{topo}=38%, degree correlation, DC_{geoid}=90% and DC_{topo}=62%, minimization function, F_{min} =4.7, and rms_{topo}= 216 m.

The third solution-family (Fig. 13) produces a fairly good geoid (variance reduction 80% and degree correlation 91%), but rather poor resemblance to the topography (15% and 5%), which is responsible for the higher value of minimization function, *f*=4.8. The amplitudes of the surface dynamic topography field are under-predicted, the rms are 193 m, 216 m, and 194 m for the first, second, and third families correspondingly (compare to rms of 340 m for the observed field, Fig. 10b). The maxima for the geoid and topography coincide closely, although for the topography it is displaced further into the Central Pacific.

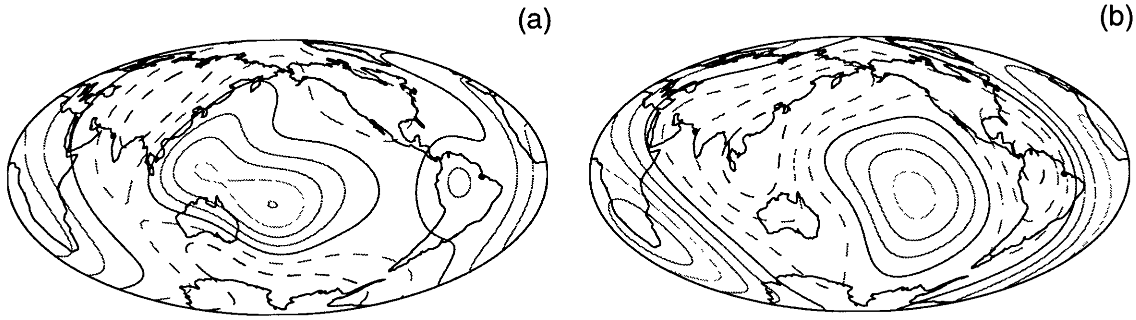

Figure IV-13. The geoid (a) and surface dynamic topography (b) fields corresponding to the third family (as in Fig 7c). The contour levels are as in Fig. 10. Field characteristics: variance reduction, VR_{geoid}=80% and VR_{topo}=15%, degree correlation, DC_{geoid}=91% and DC_{topo}=5%, minimization function, F_{min} =4.8, and rms_{topo}= 194 m.

We also analyzed the contribution of each density model to the different solution-families and their density conversion factors in the upper and lower mantle obtained during inversion. The results are shown in Fig. 14, where each plot corresponds to a density model with the abbreviated name shown in the title. The abscissa always represents the $d\ln\rho/d\ln v$-value in the lower mantle. The ordinate is for the conversion factor in the upper mantle. For the hybrid-models (names ending with digit 2) it corresponds to the subduction slab density contrast (kg m^{-3}) relative to the ambient mantle density. For the pure-seismic models (names ending with digit 1) it becomes the $d\ln\rho/d\ln v$-value. Each data-point in the plots corresponds to a solution of one inverse-run, and in most cases the data show a strong minimum in conversion factor space. We show the first family solutions by stars, the second family by circles, and the third family by triangles. The pure seismic models lead to convergence only to the first and second families of viscosity profiles. The hybrid models converge only to the first and third families of viscosity profiles. Thus, the only viscosity profiles seen by all density models are those from the first family.

The conversion factor varies from model to model, as we would expect. Generally, $d\ln\rho/d\ln v$-value is around 0.1 for the lower mantle, except for the Scripps model (0.04-0.05) and the block-type models, Grand (0.28) and van der Hilst (0.54). For the upper mantle the $d\ln\rho/d\ln v$-value is about the same as for the lower mantle or could be slightly higher. The slab density contrast varies around 110 kg m^{-3}.

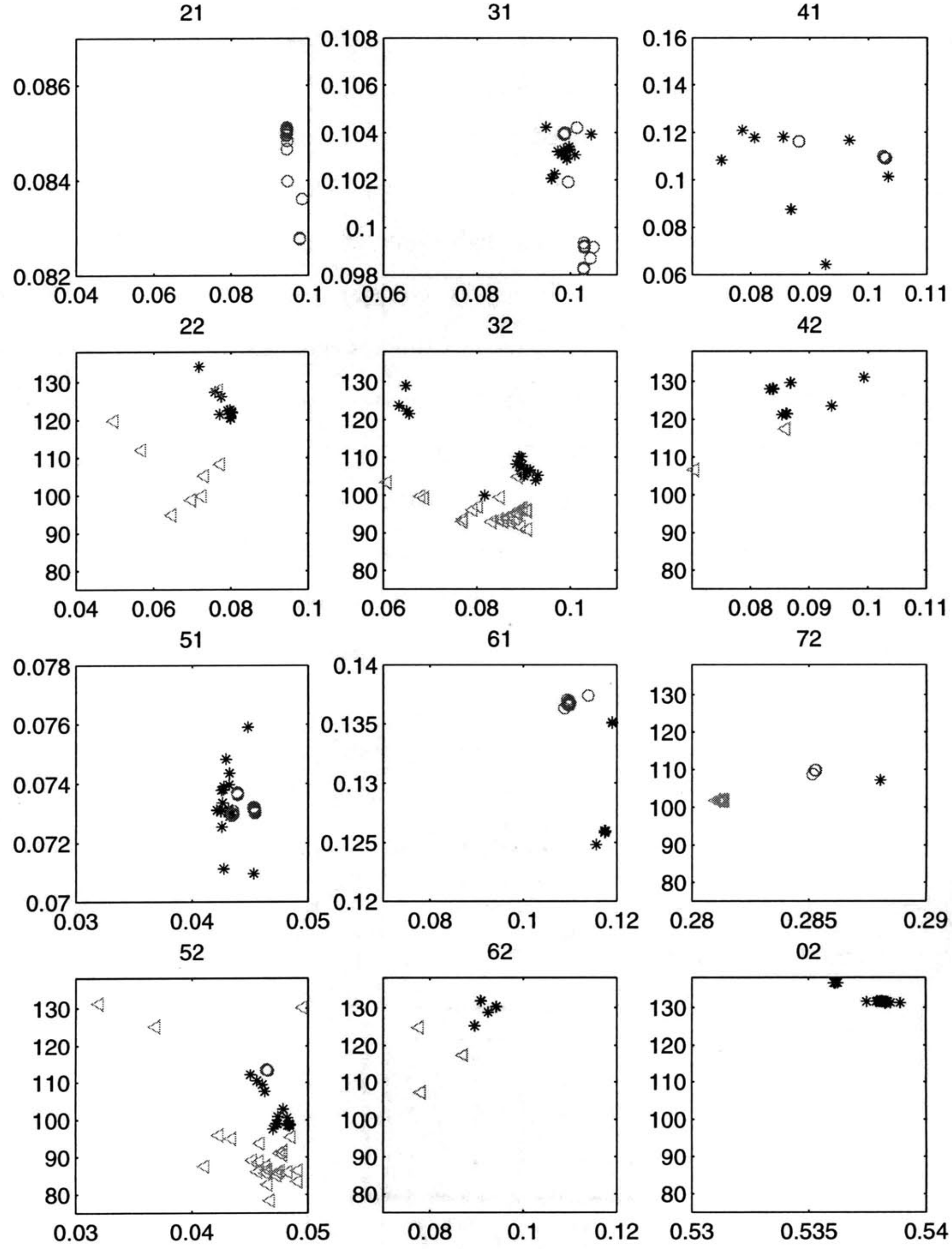

Figure IV-14. The conversion factor inverted for each density model. The abscissa corresponds to *d*ln*ρ*/*d*ln*v*-value of the lower mantle. The ordinate is *d*ln*ρ*/*d*ln*v*-value of the upper mantle for pure-seismic models (plot titles ending with digit 1), and it is the slab density contrast (kg m^{-3}) relative to the ambient mantle density for the hybrid-models (plot titles ending with digit 2). Solutions correspond to the first, second and third viscosity families (stars, circles, triangles, respectively) as in Fig. 7.

The three families provide different levels of fit to the observables. The first and the second families provide equally good fits, *f*=4.7 (the value was calculated based on the weighted average), the third family has *f*=4.8. Note, that the fitting criterion we use has information on the geoid and on the topography, including the corresponding errors. It differs from the generally used variance reduction and degree correlation. To analyze the relationships among those three, we calculate the corresponding values for each inversion solution accounted for in Fig. 7. We plot the value of the minimization function, *f* (ordinate in Fig. 15) as a function of variance reduction in per cent (stars are for the geoid and crests are for the topography in Fig. 15) and degree correlation in per cent (circles are for the geoid and triangles are for the topography).

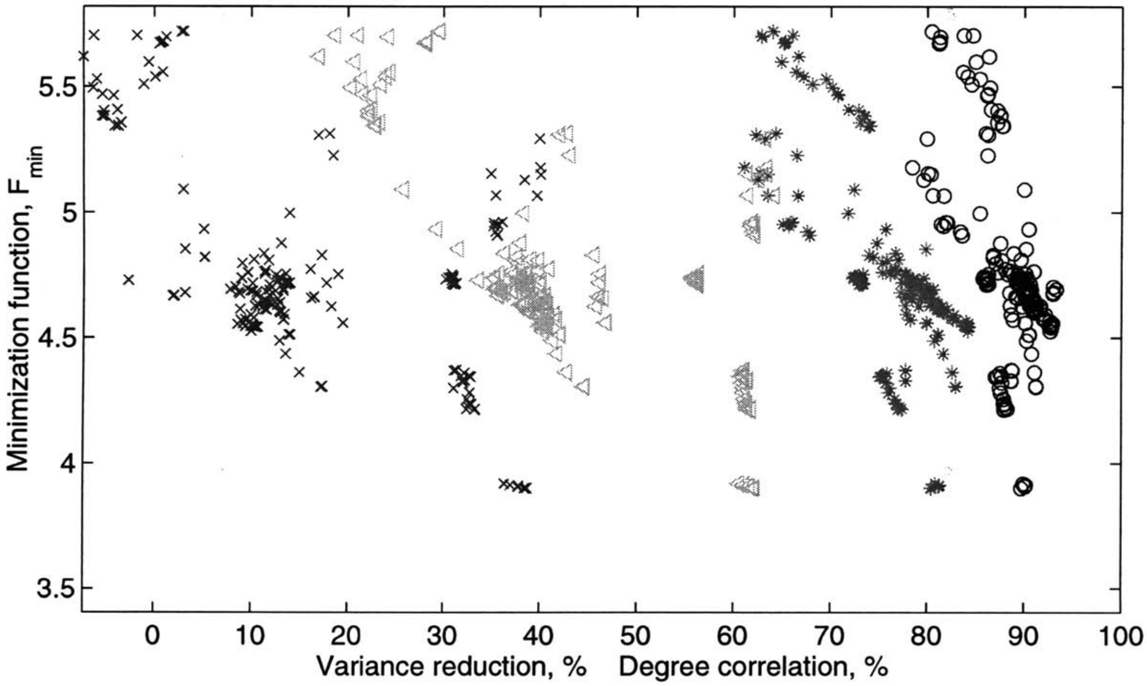

Figure IV-15. Relationship between the minimization function value (ordinate), the variance reduction (abscissa) and the degree correlation (abscissa). Variance reduction (stars for geoid, crests for topography) and degree correlation (circles for geoid, triangles for topography) are in per cent. Data points are inversion solutions, as in Fig. 7.

The data points in Fig. 15 are grouped within each density model, therefore the values do not fall on a single line, however, the general slope values are negative. This is related to the fact that different density anomaly models produce different fits to the observables. We clarify this in Fig. 16, where the ordinate corresponds to the minimization functions for the geoid (crossed symbols) or for the topography (open symbols), calculated separately as in eq. 5. The abscissa corresponds to the abbreviated name for each density anomaly model used in the inversions. The different symbols represent the different families of viscosity profile chosen by a particular inversion solution.

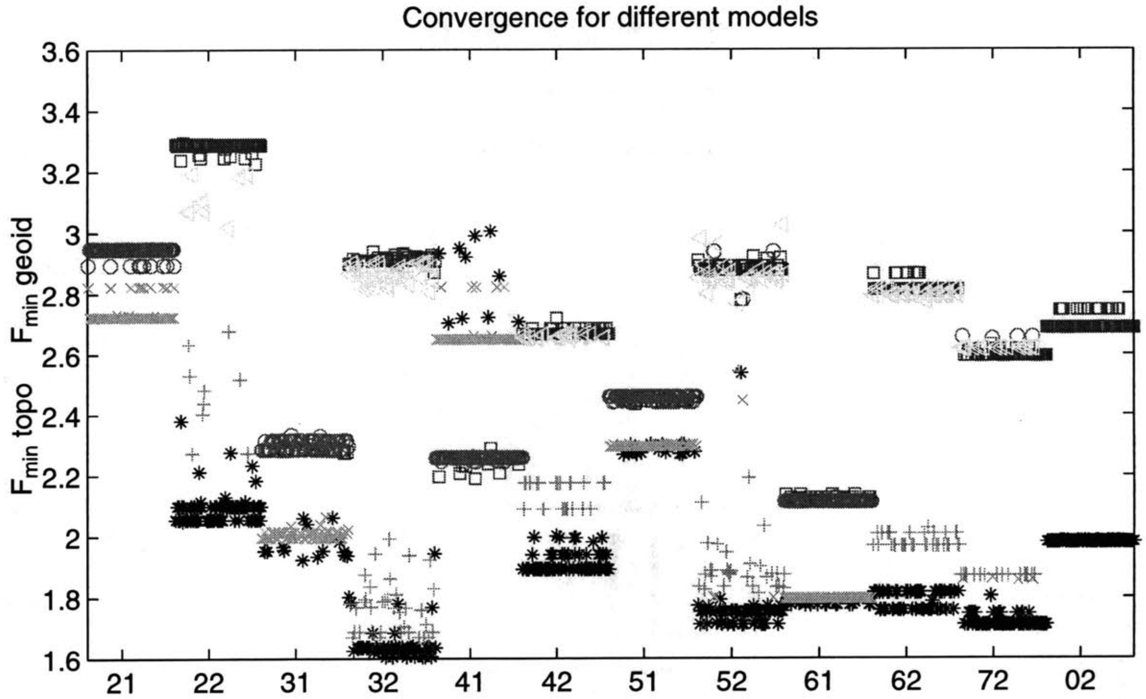

Figure IV-16. The degree of convergence for each density model participating in the inversion. The minimization function value (ordinate) is calculated separately for the geoid (crossed symbols) and for the topography (open symbols) and plotted versus model name (abscissa). Data points correspond to the first, second and third viscosity families (stars, crosses, crests for geoid, and squares, circles, triangles for topography, respectively) as in Fig. 7.

DISCUSSION

The fields of the geoid and the dynamic topography at the surface obtained during the inversion reproduce many features of the observed fields (compare Figs 11-13 with Fig. 10). The spectral resemblance is typically good, although the amplitude of the signal is usually under-predicted. To understand the general spectral characteristics of the fields, we present the results in terms of the power spectrum slope (Fig. 17, where the top panel is for the geoid and the bottom panel is for the dynamic topography).

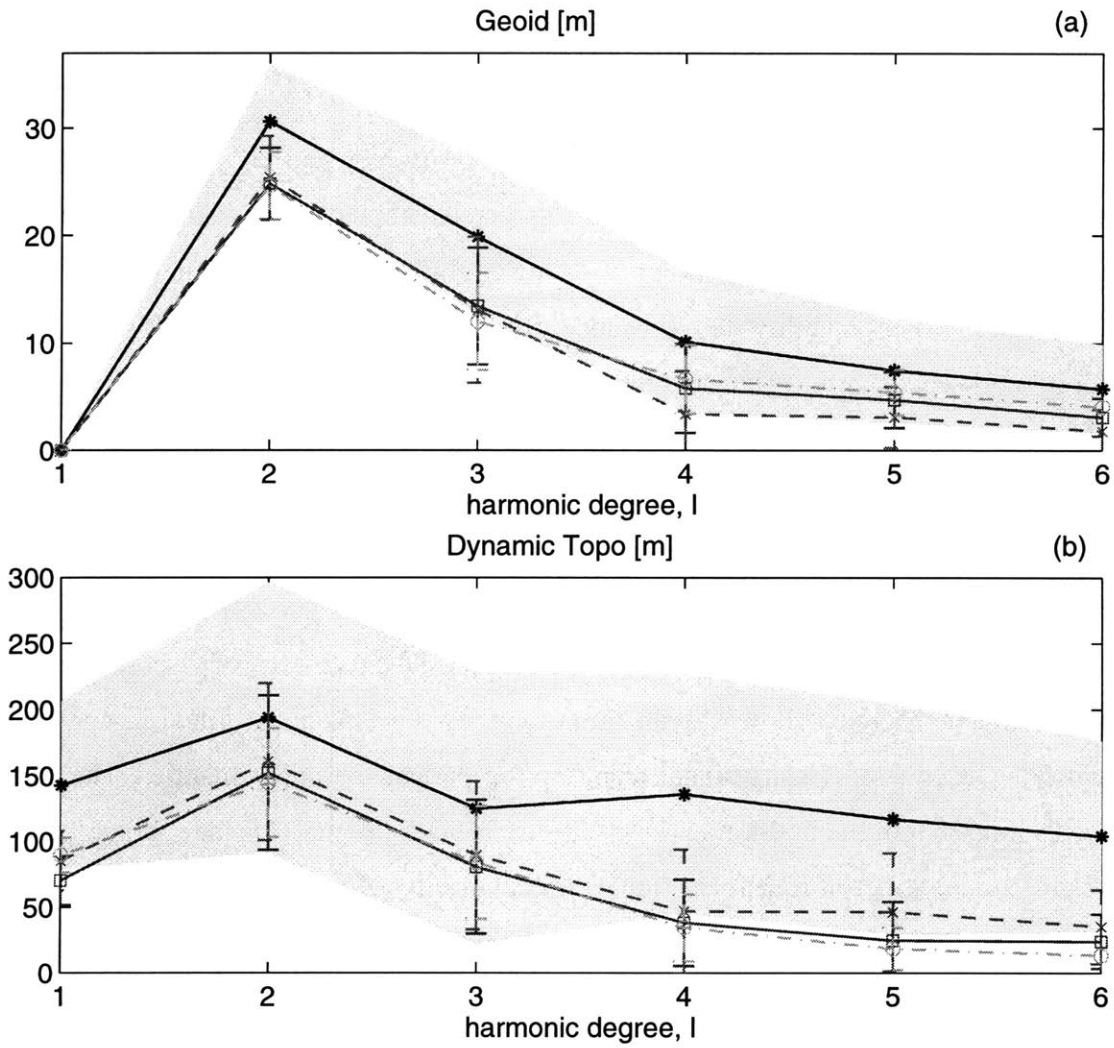

Figure IV-17. The square root of the power of the geoid (a) and the surface dynamic topography (b) fields versus spherical harmonic degree (abscissa). The observed fields are shown by the solid line with stars surrounded by the gray shading, which represents the uncertainties associated with each harmonic. The calculated fields are shown by the lines, with the error-bars corresponding to the standard deviation around the mean. The data are for the first, second, and third families of η-profiles (the solid line with squares, the dashed line with crosses, and the dash-dotted line with circles, respectively).

The observed fields (solid lines with stars) with corresponding spectral errors (gray shading) have an amplitude which always exceeds the predicted values for all three viscosity profile families (solid, dashed, and dash-dotted lines with the error bars corresponding to the first, second, and third families with the std around the mean). The geoid field amplitudes are under-predicted for all harmonics, although the values lie within the assumed uncertainties. The gradual decay of the observed signal at shorter wavelengths is repeated by all three solutions for the geoid. The observed dynamic topography spectral behavior (the relatively strong signal from the shorter wavelengths, as in Fig. 17b) could not be reproduced by the inversions. Moreover, the estimates of the first and third families of solutions lie beyond the assumed uncertainties for the shorter wavelengths. The power spectrum of the predicted topography is similar to the geoid spectrum slope: the peak is at $l=2$, followed by a weakened signal at the higher harmonics. The inability to reproduce the spectral characteristics of the dynamic topography at shorter wavelengths suggests that there are probably errors and uncertainties unaccounted for in our analysis of the short-wavelength surface dynamic topography. On the other hand, the small amplitudes of the dynamic topography for all the inversion solutions prove the compatibility of whole-mantle convection with the small dynamic topography observed on the surface. The success in modeling of the small topography amplitude is a consequence of a strong reduction of viscosity within the phase change regions (shown by all three families of viscosity profiles) in combination with the absence of density signal from the top part of the upper mantle. The material weakening within the 400-km and the 670-km solid-solid phase change regions could be related to the effect of transformational superplasticity (Panasyuk and Hager 1997). The small density anomaly in the top part of mantle is probably associated with strong chemical and thermal heterogeneities that cancel out the gravitational signature of each other (e.g., the isopycnic model by Jordan, 1988).

The viscosity profile solutions obtained can be compared with previously published results. However, the fact that our forward method considers continuous variations in viscosity and density should be kept in mind as a possible reason for disagreement. One way to compare the results is to match the shape of the geoid kernels at lower harmonics. This, for example, allows us to see the similarities between our second family (Fig. 7b) and the viscosity profile preferred by the joint inversion by Forte and Mitrovica 1996. Our first family of solutions identifies the high-viscous transition zone (Fig. 7a), which could result if a strong garnet phase controls the deformation, instead of the weaker olivine and pyroxene phases (Karato 1989; Jeanloz 1989). A stiff-transition-zone viscosity profile has been previously found by King (1995); however, the exact profiles and the geoid kernels are hard to compare due to the differences in the forward modeling. The third family of geoid kernels (Fig. 7c) resembles those of the lower-viscosity asthenosphere models (Hager and Clayton 1989). The third family of viscosity profiles is also somewhat similar to those of Cizkova *et al.* (1996) and Cadek *et al.* (1997). The familial similarity to the results of the different mentioned studies is explained by the fact that in our analysis we consider not a single density anomaly model, but nineteen models, which include P-, and S-wave seismic tomography and a slab reconstruction. As a result, we are able to determine that the second type of η-profiles is seen only by the purely seismic-tomography based models (with the exception of a couple of solutions for the two hybrid-models), and the third type of η-profiles is seen only by models with the slab-related signal. It is interesting to note that the first family of viscosity profiles was found by all density models.

Besides the viscosity profile, we simultaneously invert for the conversion factors for each of the density models. The slab-to-ambient mantle density contrast is in general agreement with earlier proposed values (Hager and Clayton 1989; Ricard *et al.* 1993). The seismic slowness-to-density anomaly conversion obtained during our analysis differs from model to model, however, it is generally smaller than the ones predicted by experimental (Karato 1993; Chopelas 1992) or analytical (Forte *et al.* 1994; Hager and Clayton 1989; Cadek *et al.* 1997) studies. There are many reasons for these differences. When comparing to the experimental results, one has to remember that the factors obtained during the inversion depend on the types of seismic waves involved, the earth reference model, and the method of inversion. The analytical studies adopt a different parameterization of the conversion factor, continuous or step-like profiles, and a different modification of the seismic/slab models, such as a combination of signals from seismic tomography, slab reconstruction, and dynamic topography of internal boundaries.

CONCLUSIONS

The main goal of this study was to analyze the gravitational constraints on the mantle viscosity profile using a variety of models for the earth's inner structure and additional constraints applied by the surface topography. We suggest a new approach in η-inverse studies, which takes into consideration uncertainties in the observables and in the input density data, and deficiencies of forward modeling. This method uncovers the reasons for the inexact resemblance to the geoid field, which are mainly due to the uncertainties in measurement and interpretation of the earth's inner structure. This careful error analysis allows to reduce the impact of the most erroneous information on the results of the inversion.

To improve the quality of the forward model, we modified the formulation to handle more realistic, continuous variations in radial viscosity, allowing for discontinuous jumps where appropriate (Appendix A). To perform a joint inversion in a self-consistent way, we built a model of the surface dynamic topography with associated spectral errors. We also accounted for errors associated with neglecting the geoid anomalies produced by the isostatically compensated crust, lithosphere, and tectosphere. To gain statistical confidence, we performed the inversion using a variety of density models (based on the global, block-type, S-, P- seismic velocity tomographic models in combination with a slab reconstruction model) starting from a hundred randomly distributed initial conditions.

The inversion revealed three distinct viscosity profile families (Fig. 7). All three solution-groups identify a similar viscosity profile in the lower mantle: one order of magnitude stiffening from 670-km to 2500-km, followed by a three orders of magnitude reduction in viscosity of the 300-km thick boundary layer at CMB. The small standard deviations around the mean profiles show the apparent robustness of this viscosity profile within the lower mantle. The main distinctions between the families lie within the upper mantle: the depth of the layer which has the lowest viscosity is at 400-km, 670-km, or just under the lithosphere. The most popular group of solutions is characterized by a soft layer around the 400-km phase change, with gradual stiffening to the surface and to 670-km depth. The second family displays a gradual reduction of viscosity to 670-km depth, with strong softening at both phase change regions, 400-km and 670-km depth. The third family favors a soft asthenosphere followed by a stiff transition zone.

A characteristic feature of all viscosity profiles is a one-to-two orders of magnitude reduction of viscosity within the major phase transformations, at 670-km depths, with two families having reduction at 400-km as well. Such a viscosity profile leads to a reduced dispersion of the geoid and the dynamic topography kernels in the upper mantle: the different wavelength kernels essentially overlap at the location of the softest layer. This leads to a strong positive correlation of the modeled geoid with the density anomalies at the base of upper mantle, and to a relatively small amplitude of calculated surface dynamic topography.

ACKNOWLEDGMENTS

SVP thanks Tom Jordan for inspiring the error analysis. Financial support was provided by NSF Grant EAR95-06427.

REFERENCES

Cazenave, A., Dominh, K., Rabinowicz, M., and G. Ceuleneer, Geoid and depth anomalies over ocean swells and throughs: evidence for an increasing trend of the geoid to depth ratio with age of plate, *J. Geophys. Res.*, *93*, 8064-8077, 1988.

Cadek, O., Ricard, Y., Martinec, Z., and C. Matyska, Comparison between Newtonian and non-Newtonian flow driven by internal loads, *Geophys. J. Int.*, *112*, 103-114, 1993.

Cadek, O., Yuen, D.A., and H. Cizkova, Mantle viscosity inferred from geoid and seismic tomography by genetic algorithms: results for layered mantle flow, submitted to *Phys. and Chem. of the Earth*, 1997.

Chopelas, A., Sound velocities of MgO to very high compression, *Earth Planet. Sci. Lett*, *114*, 185-192, 1992.

Christensen, U., and H. Harder, 3-D convection with variable viscosity, *Geophys. J. Int.*, *104*, 213-226, 1991.

Cizkova, H., Cadek O., Yuen, D.A., and H.-W. Zhou, Slope of the geoid spectrum and constraints on mantle viscosity stratification, *Geophys. Res. Lett.*, *23*, 3063-3066, 1996.

Clayton, R.W., and R.P. Comer, A tomographic analysis of mantle heterogeneities, *Terra Cognita*, *4*, 282-283, 1984.

Dehant, V. and J.M. Wahr, The response of a compressible, non-homogeneous earth to internal loading: theory, *J. Geomag. Geoelect.*, *43*, 157-178, 1991.

Dziewonski, A.M., B.H. Hager, and R.J. O'Connell, Large-scale heterogeneities in the lower mantle, *J. Geophys. Res.*, *82*, 239-255, 1977.

Dziewonski, A.M. and D.L. Anderson, Preliminary reference Earth model, *Phys. Earth Planet. Inter.*, *25*, 297-356, 1981.

Ekstrom, G. and A.M. Dziewonski, Improved models of upper mantle S velocity structure, *Eos Trans. AGU*, *76*, 421, 1995.

Forte, A.M. and W.R. Peltier, Plate tectonics and aspherical earth structure: the importance of polidal-toroidal coupling, *J. Geophys. Res.*, *92*, 3546-3680, 1987.

Forte, A.M. and W.R. Peltier, Viscous flow models of global geophysical observables, 1 Forward problems, *J. Geophys. Res.*, *96*, 20,131-20,159, 1991.

Forte, A.M., Peltier, W.R., Dziewonski, A.M., and R.L. Woodward, Dynamic surface topography: a new interpretation based upon mantle flow models derived from seismic tomography, *Geophys. Res. Lett.*, *20*, 225-228, 1993.

Forte, A.M. and W.R. Peltier, The kinematics and dynamics of poloidal-toroidal coupling in mantle flow: The importance of surface plates and lateral viscosity variations, *Adv. Geophys.*, *36*, 1-119, 1994.

Forte, A.M., Woodward, R.L., and A.M., Dziewonski, Joint inversions of seismic and geodynamic data for models of three-dimensional mantle heterogeneity, *J. Geophys. Res.*, *99*, 21,857-21,877, 1994.

Forte, A.M., and J.X. Mitrovica, A new inference of mantle viscosity based on a joint inversion of post-glacial rebound data and long-wavelength geoid anomalies, *Geophys. Res. Lett.*, *23*, 1147-1150, 1996.

Gable, C.W., O'Connell, R.J., and B.J. Travis, Convection in three dimensions with surface plates; Generation of toroidal flow, *J. Geophys. Res.*, *96*, 8391-8405, 1991.

Gordon Research Conference, 1996.

Grand, S.P., Mantle shear structure beneath the Americas and surrounding oceans, *J. Geophys. Res.*, *99*, 11,591-11,621, 1994.

Gurnis, M., Bounds on global dynamic topography from Phanerozoic flooding of continental platforms, *Nature, 344*, 754-756, 1990.

Hager, B.H., Global isostatic geoid anomalies for plate and boundary layer models of lithosphere, *Earth Planet. Sci. Lett, 63*, 97-109, 1983.

Hager, B.H., Subducted slabs and the geoid: Constraints on mantle rheology and flow, *J. Geophys. Res.*, *89*, 6003-6015, 1984.

Hager, B.H., and R.J. O'Connell, Subduction zone dips and flow driven by the plates, *Tectonophysics, 50*, 111-134, 1978.

Hager, B.H., and R.J. O'Connell, A simple global model of plate dynamics and mantle convection, *J. Geophys. Res.*, *86*, 4843-4867, 1981.

Hager, B.H., and R.W. Clayton, Constraints on the structure of mantle convection using seismic observations, flow models, and the geoid, in *Mantle Convection*, edited by W.R. Peltier, pp. 657-763, Gordon and Breach Science Publishers, 1989.

Hager, B.H, and M.A. Richards, Long-wavelength variations in the Earth's geoid: physical models and dynamical implications, *Phil. Trans. R. Soc. Lond. A, 328*, 309-327, 1989.

Hager, B.H., Clayton, R.W., Richards, M.A., Comer R.P., and A.M. Dziewonski, Lower mantle heterogeneity, dynamic topography and the geoid, *Nature, 313*, 541-545, 1985.

Inoue, H., Y. Fukao, K. Tanabe, and Y. Ogata, Whole mantle P-wave travel time tomography, *Phys. Earth Planet. Inter., 59*, 294-328, 1990.

Jeanloz, R., High pressure chemistry of the Earth's mantle and core, in *Mantle Convection*, edited by W.R. Peltier, pp. 203-259, Gordon and Breach Science Publishers, 1989.

Jordan, T., Continents as a chemical boundary layer, *Phil. Trans. R. Soc. Lond. A, 301*, 359-373, 1981.

Jordan, T., Structure and formation of the continental tectosphere, *J. Petrol.*, Special lithosphere issue, 11-37, 1988.

Karato, S.-I., Plasticity-crystal structures systematics in dense oxides and its implications for the creep strength of the Earth's interior: A preliminary result, *Phys. Earth Planet. Inter., 55*, 234-240, 1989.

Karato, S.-I., Importance of anelasticity in the interpretation of seismic tomography, *Geophys. Res. Lett.*, *20*, 1623-1626, 1993.

King, S.D., Radial models of mantle viscosity: results from a genetic algorithm, *Geophys. J. Int., 122*, 725-734, 1995.

Le Stunff, Y, and Ricard, Y., Topography and geoid due to lithospheric mass anomalies, *Geophys. J. Int.*, *122*, 982-990, 1995.

Lerch, F.J., S.M. Klosko, and G.B. Patch, A refined gravity model from LAGEOS (GEM-L2), *NASA Tech. Memo 84986*, 1983.

Love, A.E.H., *Some problems in Geodynamics*, Cambridge University Press, 1911.

Marty, J.C., and A. Cazenave, Regional variations in subsidence rate of lithospheric plates: Implication for thermal cooling models, *Earth Planet. Sci. Lett. 94*, 301-315, 1989.

Masters, G., and H. Bolton, Large-scale shear velocity structure of the mantle, *Eos Trans. AGU, 72*, 316, 1991.

Masters, G., Johnson, S., Laske, G., and H. Bolton, A shear velocity model of the mantle, *Philos. Trans. R. Soc. Lond., A, 354*, 1385-1414, 1996.

MATLAB 5, Optimization toolbox, 1997.

Mitrovica, J.X., and A.M. Forte, Radial profile of mantle viscosity: Results from the joint inversion of convection and post-glacial rebound observables, *J. Geophys. Res., 102*, 2751-2769, 1997.

Mooney, W.D., Laske, G., and G. Masters, CRUST 5.1: A new global Crustal Model at 5x5 degrees, *J. Geophys. Res.*, in press, 1997.

Müller, R.D., Roest, W.R., Royer, J.-Y., Gahagan, L.M. and J.G. Sclater, Digital Isochrons of the World's Ocean Floor, submitted to *J. Geophys. Res.*, 1997.

Nakiboglu, S.M., Hydrostatic theory of the Earth and its mechanical implications, *Phys. Earth Planet. Inter., 28,* 302-311, 1982.

O'Connell, R.J., Gable, C.W., and B.H. Hager, Toroidal-poloidal partitioning of lithospheric plate motion, in *Glacial isostasy, sea-level and mantle rheology*, eds Sabadini, R., Lambeck, K. and Boschi, E., pp. 535-551, Kluwer, Boston, 1991.

Olson, P., and D., Bercovici, On the equipartitioning of kinetic energy in plate tectonics, *Geophys. Res. Lett., 18,* 1751-1754, 1991.

Panasyuk, S.V., Hager, B.H., and A.M. Forte, Understanding the effects of mantle compressibility on geoid kernels, *Geophys. J. Int., 124,* 121-133, 1996.

Panasyuk, S.V., and B.H. Hager, A model of transformational superplasticity in the upper mantle, in press *Geophys. J. Int.,* 1997.

Parsons, B., and J.G. Sclater, An analysis of the variation of the ocean floor bathymetry and heat flow with age, *J. Geophys. Res, 82,* 803-827, 1977.

Quinn, K.J., and M.K. McNutt, Inversion of topography and geoid for mantle viscosity beneath the Pacific plate using genetic algorithms, submitted to *J. Geophys. Res.*, 1998.

Ranalli, G., The microphysical approach to mantle rheology, in *Glacial isostasy, sea-level and mantle rheology*, eds Sabadini, R., Lambeck, K. and Boschi, E., pp. 343-378, Kluwer, Boston, 1991.

Ribe, N.M., The dynamics of thin shells with variable viscosity and the origin of toroidal flow in the mantle, *Geophys. J. Int., 110,* 537-552, 1992.

Ricard, Y., Fleitout, L., and C. Froidevaux, Geoid heights and lithospheric stresses for a dynamic Earth, *Ann. Geophys., 2,* 267-286, 1984.

Ricard, Y., and C. Vigny, Mantle dynamics with induced plate tectonics, *J. Geophys. Res., 94,* 17,543-17,559, 1989.

Ricard, Y., Vigny, C., and C. Froidevaux, Mantle heterogeneities, geoid, and plate motion: A Monte Carlo inversion, *J. Geophys. Res., 94,* 13,739-13,754, 1989.

Ricard, Y., M.A. Richards, C. Lithgow-Bertelloni, and Y. LeStunff, A geodynamic model of mantle heterogeneity, *J. Geophys. Res., 98,* 21,895-21,909, 1993.

Richards, M.A., and B.H. Hager, Geoid anomalies in a dynamic Earth, *J. Geophys. Res., 89,* 5987-6002, 1984.

Richards, M.A., and B.H. Hager, Effects of lateral viscosity variations on long-wavelength geoid anomalies and topography, *J. Geophys. Res., 94,* 10,299-10,313, 1989.

Sammis, C.G., J.C. Smith, G. Schubert, and D.A. Yuen, Viscosity-depth profile in the Earth's mantle: Effects of polymorphic phase transitions, *J. Geophys. Res., 85,* 3747-3761, 1977.

Sammis, C.G., and J.L. Dein, On the possibility of transformational superplasticity in the Earth's mantle, *J. Geophys. Res., 79,* 2961-2965, 1974.

Simons M. and B. H. Hager, Localization of the gravity field and the signature of glacial rebound, *Nature, 390,* 500-504, 1997.

Stein, C.A., and A. Stein, A model for the global variation in oceanic depth and heat flow with lithospheric age, *Nature, 359,* 123-129, 1992.

Su, W.-J. and A.M. Dziewonski, Predominance of long wavelength heterogeneity in the mantle, *Nature, 352,* 121-126, 1991.

Su, W.-J., R.L. Woodward, and A.M. Dziewonski, Degree 12 model of shear velocity heterogeneity in the mantle, *J. Geophys. Res., 99,* 6945-6980, 1994.

Tanimoto, T., Long-wavelength S-wave velocity structure throughout the mantle, *Geophys. J. Int., 100,* 327-336, 1990.

Tarantola, A., *Inverse problem theory*, Elsevier Science B.V., Amsterdam, 1997.

van der Hilst, R.D., S., Widiyantoro, and E.R. Engdahl, Evidence for deep mantle circulation from global tomography, *Nature, 386,* 578-584, 1997.

Zhang, S., and U.R. Christensen, Some effects of lateral viscosity variations on geoid and surface velocities induced by density anomalies in the mantle, *Geophys. J. Int., 114,* 531-547, 1993.

APPENDIX A

Continuous variations of viscosity handled by matrixant approach

The general physical assumptions and their mathematical representation are based on the theory presented in Panasyuk *et al.* 1996; therefore, we omit the detailed description here. The formulation treats flow stresses without separating them into viscosity and strain rate parts. That is, when a stress component is expanded into spherical harmonics, the radial function (e.g. y_4, as in equations 10, Panasyuk *et al.* 1996) reflects both viscosity and strain rate depth dependencies. Therefore, the equations used to derive the matrix differential equation,

$$\partial^0 \mathbf{u}_l = \mathbf{A}_l \mathbf{u}_l + \mathbf{b}_l , \tag{A 1}$$

are true for continuously varying viscosity $\eta(r)$. The exponent matrix $\mathbf{A}_l$ has five non-diagonal terms containing the normalized viscosity. Since the mantle viscosity could vary by several orders of magnitude, the $\mathbf{A}_l$ matrix could change significantly within the layer, prohibiting use of the matrixant approach. We resolve this complication by introducing a new set of poloidal variables (the notation is similar to that used in Panasyuk *et al.* 1996):

$$\mathbf{u}(r) = \begin{bmatrix} y_1\eta^* & y_2\eta^*\Lambda & (y_3+\rho_0 y_5)r & y_4 r\Lambda & y_5 r\bar{\rho}\Lambda & y_6 r^2\bar{\rho} \end{bmatrix}^{\mathrm{T}} , \tag{A 2}$$

where $\eta^* = \eta_0(r)/\bar{\eta}$ is viscosity as a function of radius, normalized by the reference value. In analogy with the compressibility factor,

$$\chi(r) = \frac{r}{\rho_0(r)} \frac{\partial \rho_0(r)}{\partial r} , \tag{A 3}$$

we introduce a viscosity factor:

$$\zeta(r) = \frac{r}{\eta_0(r)} \frac{\partial \eta_0(r)}{\partial r} , \tag{A 4}$$

so that the matrix $\mathbf{A}_l$ becomes:

$$\begin{bmatrix} -(2+\chi-\zeta) & \Lambda & 0 & 0 & 0 & 0 \\ -\Lambda & 1+\zeta & 0 & 1 & 0 & 0 \\ (12+4\chi) & -6\Lambda & 1 & \Lambda & \frac{\chi\rho_0}{\Lambda\bar{\rho}} & 0 \\ -(6+2\chi)\Lambda & 2(2\Lambda^2-1) & -\Lambda & -2 & 0 & 0 \\ 0 & 0 & 0 & 0 & 1 & \Lambda \\ 0 & 0 & 0 & 0 & \Lambda & 0 \end{bmatrix}. \tag{A 5}$$

Note that now **A** can be represented as a sum of four matrix expressions instead of three terms as in Panasyuk *et al.* 1996:

$$\mathbf{A}(r) = \mathbf{A}_0 + \chi(r)\mathbf{A}_1 + \frac{\chi(r)\rho_0(r)}{\bar{\rho}}\mathbf{A}_2 + \zeta(r)\mathbf{A}_3 \tag{A 6}$$

Here $\mathbf{A}_0$ is equivalent to the matrix for incompressible flow (Hager and Clayton 1989). The matrix $\mathbf{A}_1$ gives the effect of compressibility on flow, $\mathbf{A}_2$ is related to a specific combination of stress and potential into one variable (Panasyuk *et al.* 1996). And the matrix $\mathbf{A}_3$ accounts for the continuously changing viscosity. Solving the matrix differential equation, we write the propagator between the upper (ocean-mantle boundary) and the lower boundary (core-mantle interface) as a product of sub-propagators (similar to the handling of compressible flow). Each sub-propagator now has one more additional term:

$$\mathbf{P}_{r_2}^{r_1} = \exp\left\{ \mathrm{A}_0 \ln\frac{r_1}{r_2} + \mathrm{A}_1 \ln\frac{\rho_0(r_1)}{\rho_0(r_2)} + \mathrm{A}_2 \frac{\rho_0(r_1)-\rho_0(r_2)}{\bar{\rho}} + \mathrm{A}_3 \ln\frac{\eta_0(r_1)}{\eta_0(r_2)} \right\}. \tag{A 7}$$

To be able to apply the propagator technique, we ought to make sure that the argument of the exponential does not vary significantly within the layer. Analysis of the variations due to the density change was done in Panasyuk *et al.* 1996. The variations due to a non-constant viscosity are expressed by the last term. It is only when the viscosity changes exponentially between r_1 and r_2, that the $\mathbf{A}_3$ term is constant within the layer. Where the slope of the exponent changes or the viscosity change is discontinuous, it is necessary to stop to tie up the propagators. Similarly, when the viscosity changes dramatically within/across a thin layer, such as a phase change region, it is reliable to treat it as a boundary and couple the solutions across it. We approximate the **u**-vector across the density/viscosity discontinuity and derive the boundary conditions for the new system. In the limit of a thin phase change region, there is a jump condition on **u**. The first two terms related to the flow velocity change as:

$$u_1^{z-} = \frac{\eta^{z-}}{\eta^{z+}}\frac{\rho^{z+}}{\rho^{z-}} u_1^{z+} \text{ and } u_2^{z-} = \frac{\eta^{z-}}{\eta^{z+}} u_2^{z+} + \frac{\eta^{z-}}{\eta_z^*}\frac{\Delta z}{z} u_4^{z+} . \qquad \text{(A 8)}$$

The third and the fourth **u**-components are approximated across the phase change as:

$$u_3^{z-} \approx 4\frac{\Delta\rho^{z}}{\rho^{z-}}\frac{\eta_z^*}{\eta^{z+}} u_1^{z+} + u_3^{z+} + \frac{\Delta\rho^{z}}{\Lambda\bar{\rho}} u_5^{z+} \text{ and } u_4^{z-} \approx -2\Lambda\frac{\Delta\rho^{z}}{\rho^{z-}}\frac{\eta_z^*}{\eta^{z+}} u_1^{z+} + u_4^{z+} . \qquad \text{(A 9)}$$

The gravity-related fifth and six components are continuous since we assume that the phase change or the thermal boundary is located at a constant radius.

We combine the internal and external boundary conditions with the matrixant approach to obtain a system of equations similar to eq. 42 in Panasyuk *et al.* 1996, and solve it with respect to the ocean-mantle boundary deflection, δa, and the potential anomaly, $V_1^e(r)$ at the ocean surface (r = e). The geoid kernels, displayed in the figures, are normalized by the geoid deflection due to a mass at the surface:

$$G^l(r) = \frac{(2l+1)}{4\pi\gamma e} V_1^e(r) . \qquad \text{(A 10)}$$

Note that the normalized geoid kernels are identical to the potential kernels normalized by the potential due to a mass at the surface. In the main text we omit the superscript *e* assuming that the gravity field is considered at the ocean surface.

APPENDIX B

Exponential viscosity variations versus constant layer approximation

We investigate the advantages of the new treatment of viscosity variation in the mantle by comparing the results of geoid and topography kernels calculations for both types of viscosity variation; continuous and step-like. We chose a viscosity profile that provides a somewhat similar geoid kernel at l=2 to that one obtained by the inversion. However, the test profile does not have the reduction in viscosity associated with the phase changes (Fig. B1). To simulate the test-viscosity profile, the mantle is subdivided into several layers, so that the depths of each layer are the same for both treatments, continuous and step-like. The only requirement of such a parameterization is that a layer boundary has to coincide with the depth of a discontinuous density/viscosity change, or with the depth where the viscosity functional dependence changes. Within the layer the viscosity is set to change exponentially in case of the "continuous" treatment, and it is kept constant in case of the "step-like" approach.

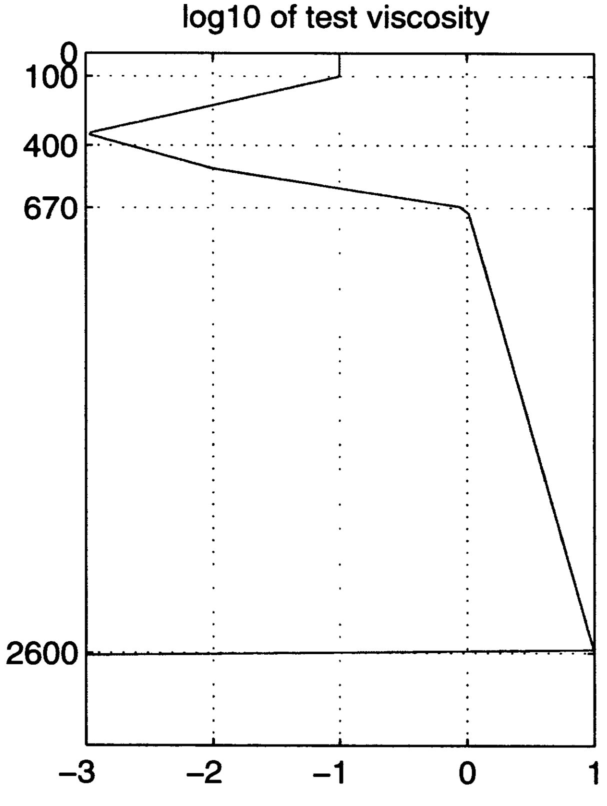

Figure IV-B1. Decimal logarithm of the viscosity profile versus depth (km) for the test comparison between the approaches considering continuous and step-like variations in viscosity.

The geoid and topography kernels for this test are displayed in Fig. B2, left and right panel correspondingly. We start with the accurate approximation, where we sample the upper mantle every 10 km and the lower mantle every 50 km (total of 114 steps). Both approaches lead to very similar kernels; the solid lines in Fig. B2 overlap.

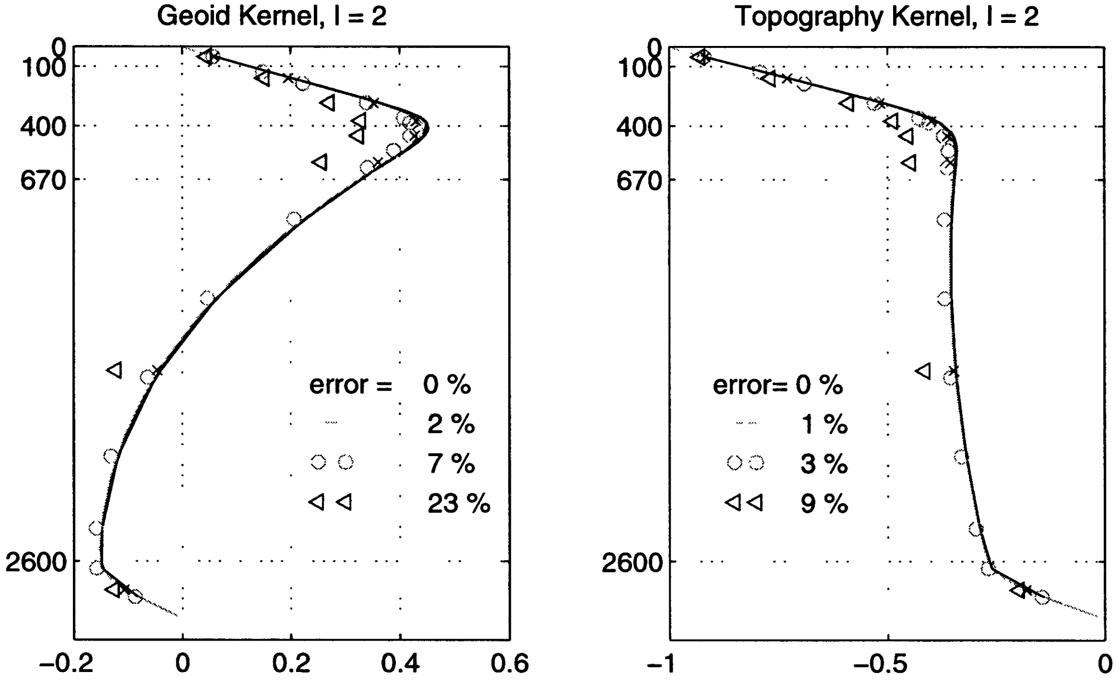

Figure IV-B2. Geoid (left panel) and surface dynamic topography (right panel) kernels for the test-viscosity profile (as in Fig. B1). The kernels of the different mantle sampling are shown by the solid lines (114 and 26 steps), circles (16), and triangles (8) for the step-like approach, and by the solid lines (114, 26, 16 steps) and crosses (8) for the continuous approach. The accuracy for the step-like approach is calculated in per cent of the maximum amplitude of the kernel.

Next we roughen the approximation by considering fewer layers. To estimate the accuracy of each approximation, we calculate the difference between the calculated kernel and the accurate one (with 114 steps) in per cent of the maximum value of the kernel (which is about 0.45 for the geoid, at a depth of 400-km, and -1 for the topography, at the surface). Since the step-like approach provides results not as accurate as the continuous treatment, we display the accuracy for only the step-like viscosity profile in the right corner of the plots (it is zero for the first test). The deviation of the kernels for the exponential approach could be barely detected on the plot for the most rough mantle sampling. The second mantle sampling is every 75 km in the upper mantle and 200 km in the lower mantle (total of 26 steps). The deviation of the step-like approach is about 2 per cent and could be distinguished as a slight mismatch in the solid lines at 400-km depth for the geoid kernel (1 per cent for topography). The third test samples the mantle every 150-km and 400-km in the upper and lower mantle, correspondingly, (total of 16 steps). The departure of the step-like approach is about 7 per cent for geoid and 3 per cent for topography, and it is marked by the circles centered at the sampling depths. The exponential approach solution is still indistinguishable from the first test kernels. As the largest degree of roughening, we consider only 8 steps across the entire mantle. The constant-in-layers approach deviates as much as 23 per cent for the geoid and 9 per cent for the topography, its solution is marked with triangles located at the sampling depths. The departure of the exponential solution is finally seen around the 400-km depth and is displayed with the crosses centered at the sampling depths.

As a result of this test, we conclude that the new approach which considers the exponential variations of mantle viscosity is very accurate. It allows us to calculate the geoid and the surface dynamic topography kernels with the minimum number of depth sampling points. The choice of a particular mantle stratification is crucial to the level of the accuracy achieved. The layer boundaries have to coincide with the discontinuities in density and viscosity, as well as with the depth of viscosity exponential law changes. In this case the minimal number of layers necessary to calculate mantle flow equals the number of density/viscosity discontinuities (which is three for the PREM density profile) plus the number of changes in the exponential law of viscosity variation.

Chapter V. A MODEL OF DYNAMIC TOPOGRAPHY. [4]

INTRODUCTION

The topography of the earth's surface reflects the distribution of compositional and thermal heterogeneities within the planet. Deep-seated, presumably thermal, anomalies drive mantle convection, creating normal stresses that deflect the chemical interfaces (e.g., the surface). The deflections of the mantle boundaries (top and bottom), shaped by viscous mantle flow, vary on the scale of mantle convection and are often referred to as dynamic topography. Unlike its origin, the amplitude and the pattern of dynamic topography causes unsettling debates within the geophysical community. The analysis is complicated by the fact that the dynamic topography signature is obscured by the crust and lithosphere. Owing to the continuous differentiation of mantle material, surface erosion, sedimentation, and active tectonics, a thick layer of generally light material overlies the mantle. These surface formations are often referred to as static topography. The term is probably accurate for the long-lived crust and stable tectosphere, e.g., billion-year-old cratonic rocks are found which have been brought to the surface from the depth 150-200 km (see review in Jordan, 1979). However, for the sub-oceanic lithospheric formations, what we call "non-dynamic topography" describes the changes due to a different material rheology, e.g., the transition to elastic behavior, which cannot be analyzed successfully in terms of current viscous flow models. In this paper we define the observed topography as a combination of dynamic and static parts, and we estimate the dynamic topography by correcting the observed topography for the static part. Since previous studies of dynamic topography suggest (Colin and Fleitout 1990; Cazenave and Lago 1991; Gurnis 1990; Le Stunff and Ricard 1997) or predict (Hager and Clayton 1989; Ricard *et al.* 1993; Forte *et al.* 1993) fields of extremely different amplitude and pattern, we also estimate the uncertainties associated with the dynamic topography.

---

[4] to be submitted to *Geophysical Research Letters*, by Panasyuk, S.V., and B.H. Hager, 1998.

A knowledge of dynamic topography would allow us to constrain the earth's mantle viscosity profile, the temporal and spatial variations of sea-level, and to apply these additional constrains on the earth model. There are several quantitative models of crust and tectonic regionalization (e.g., Dziewonski *et al.* 1975; Mauk 1977; Jordan 1981; Mooney *et al.* 1997) based on geological sampling of the upper crust and the seismic wave analysis. Models of sub-oceanic lithosphere subsidence (e.g., Cazenave *et al.* 1988; Marty and Cazenave 1989; Stein and Stein 1992) follow the general principles of isostasy (e.g., Love 1911). Each of these alterations of the observed topography is based on a model which describes the origin of the static topography and is compared with the acquired data. There are few indirect measurements of the dynamic topography amplitude, such as flooding records related to the rise and fall of continents (Gurnis 1990), or smooth topography over the abyssal oceanic floor (Parsons and Sclater 1977). In our approach, we apply recent models of the crust and the age of the ocean floor to estimate the static topography and to build a model of dynamic topography. Carrying the uncertainties associated with the crustal structure and the oceanic ages through the model, we estimate the spatial and the spectral errors which accompany our model. We compare the dynamic topography obtained by correcting for the static topography with the dynamic topography calculated based on the geoid-topography inversion.

METHOD DESCRIPTION

The observed topography and bathymetry (ETOPO5, 1992) are well correlated with crustal heterogeneities (see field expansion for l=1-12 in Fig. 1), which favors the hypothesis of isostatic compensation. A general principle of local isostasy states, to first-order accuracy, that if a heterogeneous mass is in static equilibrium, the pressure from any vertical mass-column has to be equal to pressure at a given depth, the so-called depth of compensation (e.g., Love 1911; Jeffreys 1970; Garland 1977). That is, if an isostatically compensated layer consisting of all static mass heterogeneities is subtracted from the observed topography, the isobaric surface at the compensation depth should have no topography. However, if residual topography is still observed, it is probably due to processes unaccounted for, static or/and dynamic.

ETOPO–5, contours +/– 1 km,

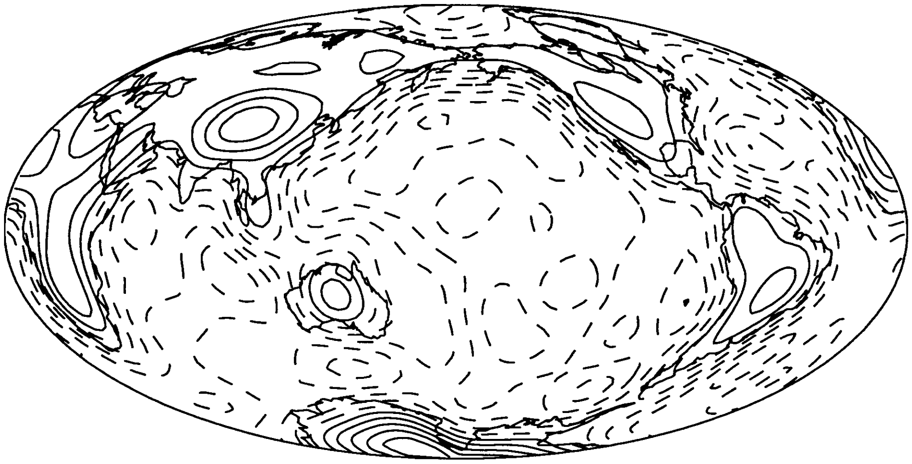

Figure V-1. Spherical harmonic expansion, l=1-12 , of the observed topography and bathymetry based on the data set ETOPO5, 1992. Contour intervals are 1km (solid lines are positive and zero values, dashed lines are negative).

To build a model of dynamic topography, we follow the conventional way and correct the observed topography for the static one assuming isostasy. That is, we calculate the thickness of a layer consisting of an isostatically compensated crust and remove it from the observed topography. Then we correct the residual topography for ocean floor subsidence due to lithospheric cooling. We also analyze the amplitude of the possible effect of isostatically compensated tectosphere. To estimate the uncertainties of the modeled dynamic topography, we analyze the errors brought by the input data-models (e.g., of ocean floor age) and by the variety of the currently acceptable assumptions (e.g., thickness of the plate in a model of the oceanic lithosphere cooling).

Effect of crustal correction

To correct for the static topography due to isostatically compensated crust, we use crustal model CRUST 5.1 (Mooney *et al.* 1997). The model provides data for seven structurally different layers (ice, water, soft and hard sediments, upper, middle, and lower crust); the density ρ_i and the thickness h_i for each layer as a function of position on a 5°-by-5° grid. First, we calculate the pressure due to the overburden at the base of the crust:

$$p_{\text{crust}}(\theta,\varphi)=\sum_{i=1}^{I}\rho_i g h_i \qquad \text{(V- 1)}$$

where I=7, and $h_{\text{crust}}(\theta,\varphi)=\sum_{i=1}^{I}h_i$ is the distance from the air-surface down to the base of the last crustal layer (we treat water as any other compositional layer in the model). Next, we assume a compensation-depth value, d_{comp}, under a surface point (θ^*,φ^*) and calculate pressure at this depth and location:

$$p_{\text{comp}}=p^*_{\text{crust}}+\rho^*_{\text{mantle}}gh^*_{\text{mantle}}, \qquad \text{(V- 2)}$$

where $h^*_{\text{mantle}}=d_{\text{comp}}-h_{\text{crust}}(\theta^*,\varphi^*)$.

Assuming that the density below the crust equals that of the reference mantle, ρ_{mantle}, we calculate the thickness of the mantle $h_{\text{mantle}}(\theta,\varphi)$ needed to reach p_{comp} (as in eq. 2) at every location:

$$p_{\text{comp}}=p_{\text{crust}}(\theta,\varphi)+\rho_{\text{mantle}}gh_{\text{mantle}}(\theta,\varphi). \qquad \text{(V- 3)}$$

To get the residual topography, the calculated thickness of the isostatically compensated layer, $h_{\text{crust}}(\theta,\varphi)+h_{\text{mantle}}(\theta,\varphi)$, is subtracted from the air-surface elevation.

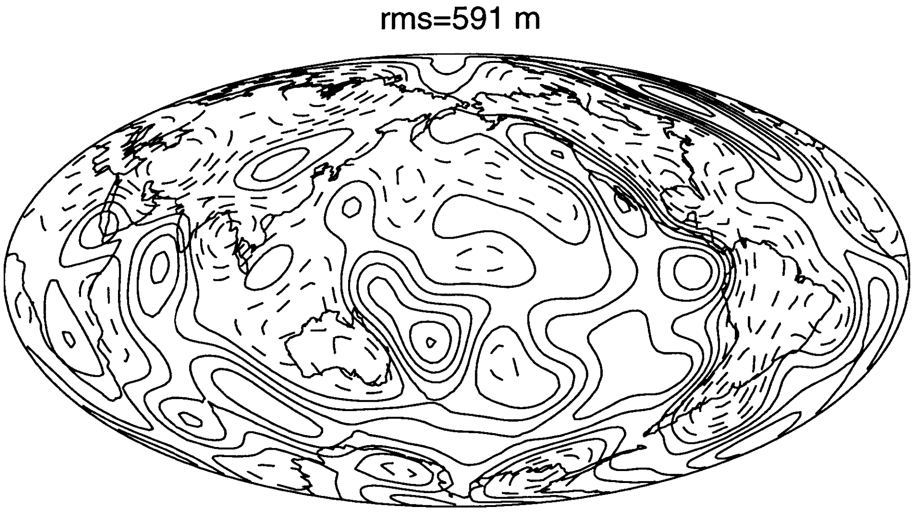

Figure V-2. Residual topography (spherical harmonic expansion, l=1-12) after correction for the isostatically compensated crust. Contour intervals are 300 m (solid lines are positive and zero values, dashed lines are negative).

We plot the topography field obtained by removing the isostatic columns of the crust and mantle material from the observed topography in Fig. 2, where we assumed $d_{\mathrm{comp}}=70$ km, which corresponds to the crust's deepest point under the Himalayas. The crustal residual topography field exhibits a clear correlation with the continents (depressions under Eurasia and the Americas) as well as with the mid-ocean ridges (uplifts over East Pacific, North Atlantic, and Indian oceans). The rms of the field, 591 m, is larger than we would expect from the geological record of continental flooding (Gurnis 1990). Noting that the residual topography was obtained by stripping only the crustal effect from the observed topography, we believe that the remaining signature of the continents and of the ridges is related to other lithospheric formations which we analyze next.

Effect of oceanic lithosphere

To correct for the effect of the lithosphere, we calculate the subsidence of the oceanic floor. Strictly speaking, the cold oceanic lithosphere is not static. Plate velocities on the order of several cm per year prove that it changes on the scale of mantle convection. Its lateral dimension is determined by the opening and closing of the oceans. However, despite the similarity with the deeper mantle, the lithosphere exhibits a distinctly different rheology. Due to lower temperatures near the surface, the sub-oceanic lithosphere behaves as an elastic plate. Therefore, we prefer to estimate the oceanic floor subsidence due to lithospheric cooling independently, without involving the crustal or the mantle material description. We follow two approaches, both relying on an assumption of isostasy: the thin plate (Stein and Stein 1992) and the thick plate (Marty and Cazenave 1989) cooling models for the lithosphere. First we correct for the crustal isostasy as above, then we use the ocean floor age data (Müller *et al.* 1997) to estimate the subsidence of the dry ocean floor, and we add the subsidence depths to the crust-corrected residual topography.

According to the model GDH1 by Stein and Stein (1992), the ocean floor depth could be calculated as a function of the ocean floor age:

$$d(t)=2{,}600+365\sqrt{t}, \qquad \text{for } t<20 \text{ Myr} \qquad \text{(V- 4)}$$

$$d(t) = 5{,}651 - 2{,}473\exp(-0.0278t), \text{ for } t \geq 20 \text{ Myr.}$$

For comparison, we also calculate a model proposed by Cazenave and Lago (1991), who assumed a thick plate cooling for the lithosphere, and obtained the worldwide mean of age-depth relationships regionally for all ages as:

$$d(t) = 2{,}400 + 315\sqrt{t}, \qquad \text{for } t<80 \text{ Myr} \qquad \text{(V-5)}$$

$$d(t) = 6{,}400 - 3{,}200\exp(-t/63), \text{ for } t \geq 80 \text{ Myr.}$$

Both models of lithospheric subsidence produce close results on a global scale (amplitude for the thick-plate cooling model is a few percent higher for l=1-12).

As an example, we calculate ocean floor subsidence using the thin-plate cooling assumption and apply the correction to the residual (Fig. 2) topography. Since the residual topography corresponds to the deflection of the mantle-air boundary, we correct the ocean floor subsidence for the difference in density:

$$d_{\text{dry}} = \frac{\rho_{\text{mantle}} - \rho_{\text{water}}}{\rho_{\text{mantle}}} d_{\text{wet}}. \qquad \text{(V-6)}$$

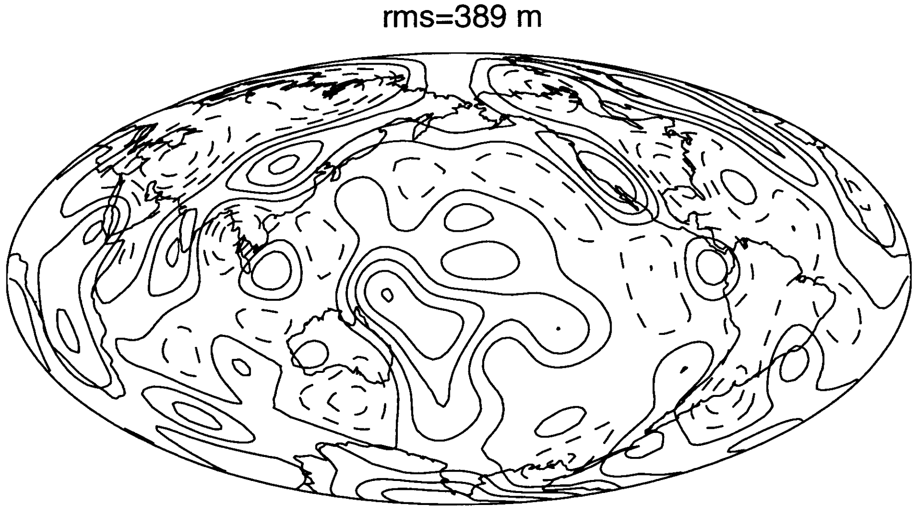

Figure V-3. Residual topography (spherical harmonic expansion, l=1-12) after correction for the isostatically compensated crust and lithosphere subsidence. Contour intervals are 300 m (solid lines are positive and zero values, dashed lines are negative).

The resulting residual topography is shown in Fig. 3, where we adjusted the sub-oceanic and sub-continental lithosphere baselines (that is the mean elevation over the continents was removed and the mean elevation over the oceans was removed). This is partially related to the uncertain lateral scales of isostasy: are the continental and the oceanic baselines level? If not, the ocean edges near the subduction zones would be uplifted up to 2.5 km relative to the closest continental coast. This would lead to a global relative depression of all continents by more than 2 km, including Africa and Antarctica. The resulting high correlation of dynamic topography with the ocean-continent pattern is in contradiction with the density anomaly distribution inferred from seismic tomography models. In addition, if the continents are to move on top of the dynamic topography, then they would have to undergo peak-to-peak vertical motions in excess of 4 km, which is at least one order of magnitude greater than the observations based on the sedimentological records of continental platforms (Gurnis 1990, 1993). The balancing is done on the base of the GTR1 regionalization model (Jordan 1981) in the spatial domain, and then the fields are converted into the spectral domain. In comparison to Fig. 2, the dynamic topography in Fig. 3 has significantly lower amplitudes (rms = 389m), and it displays no correlation with the continental or mid-ocean ridge signatures. There are noticeable, broad uplifts associated with Africa, Antarctica, and the Central Pacific. The large scale depression along the Circum Pacific is surrounded by a thin belt of uplift. More localized depressions are over Asia, North Siberia, and Eastern North America.

Effect of continental tectosphere

We estimate an order of magnitude variation in the dynamic topography that might be related to the deep-rooted continental tectosphere. Our main assumptions are based on the model presented by Jordan (1979). However, we extend the isopycnic model to allow the tectosphere to be slightly heavier than the surrounding mantle. We assume that it is much stiffer than the surrounding mantle and it is kept close to the surface by the viscous forces from the mantle flow (Shapiro 1995). First we assume that the tectosphere is static, that is at least its first 200 km is attached to the continental crust and does not participate in the mantle convective motion below. Therefore, we assume that the tectosphere exists over a long time, which allows it to reach isostatic equilibrium. To distinguish between the short- and the long-lived formations, we refer to the tectosphere regionalization (GTR1, Jordan 1981), which separates the Phanerozoic orogenic zones, Phanerozoic platforms, and Precambrian shields and platforms. To estimate the depth extent, we examine seismic tomography models of the upper mantle. As a first approximation, we assume that all three regions of tectosphere have constant thickness, and we consider the base of Precambrian shields (the oldest and the thickest) as the level of compensation. Then, the dynamic topography due to the variation in the tectosphere thickness is:

$$d = \frac{\delta\rho}{\rho_{\text{mantle}}}\left(h_{\text{shield}} - h_{\text{region}}\right), \qquad \text{(V-7)}$$

where h_{region} is the thickness of the orogenic zones or the Phanerozoic platforms, and $\delta\rho$ is the density contrast between the tectosphere and the surrounding mantle. To determine the density excess associated with the tectosphere, we rely on the research done by Shapiro, 1995. A weak correlation between the tectosphere regionalization and the geoid signal suggests only slight variations of the tectospheric density. An additional analysis of travel times allowed Shapiro to constrain the value of the conversion factor between seismic velocity, v, and density, ρ, anomalies as $d\ln\rho/d\ln v \approx 0.03$, which gives only 0.2 per cent density variation assuming a maximum of 7 per cent in the seismic velocity variation associated with the tectosphere. Therefore, assuming that the contrast in the tectosphere thickness could reach up to 300 km, one estimates the subsequent dynamic topography to be on the order of 60 meters (peak-to-peak). These deviations are indistinguishably small on the scale of the dynamic topography in Fig. 3 and on the scale of the model uncertainties, which we discuss next.

Model uncertainties

To determine the model uncertainties, we start with an analysis of the data involved (Müller *et al.* 1997; Mooney *et al.* 1997). The ocean-age errors are estimated for each data-point. They include the uncertainties in the floor ages identified from the magnetic anomalies along ship tracks, and the interpolation errors which depend on the distance of a given grid cell to the nearest magnetic anomaly identification and on the gradient of the age grid (Müller *et al.* 1997). Using the age-uncertainties, we calculate the related errors in the ocean-floor subsidence (e.g., for the plate cooling model):

$$\delta d_{\mathrm{wet}} = \frac{365}{2\sqrt{t}}\delta t, \qquad \text{for } t<20 \text{ Myr} \qquad \text{(V- 8)}$$

$$\delta d_{\mathrm{wet}} = 2473 \times 0.0278 \exp(-0.0278t)\delta t, \text{ for } t \geq 20 \text{ Myr.}$$

The errors related to the crust model CRUST 5.1 are on the order of several hundred meters for the crustal thickness (Mooney *et al.* 1997). Since a more extensive error-analysis is currently not available from the primary source, we assume that there is 50 per cent uncertainty in the residual (after the crust correction) topography.

Another source of uncertainty in the dynamic topography comes from the variety of assumptions and approaches used to determine the field. For example, as we discussed earlier, both models of sub-oceanic lithosphere cooling provide fairly good estimates of the ocean floor subsidence on a global scale. The question of the ocean-continental baseline balancing is still open to discussion. Are all continental areas leveled with the oceans or only with the old Phanerozoic platforms and Precambrian shields and platforms? To relate these uncertainties in modeling to the errors in the resulting dynamic topography, we build several dynamic topography fields, altering the assumptions used. The final field is then the spectral mean of all the fields,

$$\langle T_{lm} \rangle_N = \frac{1}{N}\sum_{n=1}^{N} T_{lm}^{n}, \qquad \text{(V- 9)}$$

and it reflects all the assumptions to a certain degree. For this set of modeled dynamic topography fields, a total of *N*, we calculate the standard deviation from the mean for each *lm*-coefficient:

$$\langle \sigma_{lm}^2 \rangle = \frac{1}{N}\sum_{n=1}^{N}\left(T_{lm}^{n} - \langle T_{lm} \rangle_{\mathrm{N}}\right)^2. \qquad \text{(V- 10)}$$

The total error in the spectral domain is then the sum of the data-related and the model-introduced uncertainties.

RESULTS

We build six fields of dynamic topography, $T^{(n)}$, N=6, where we consider assumptions of the crustal compensation depth (70 km), of the cooling lithosphere (thin- and thick-plate like) in balance with continents, and assumptions of three types of residual topography balance: no balance; GTR1-continent/ocean; GTR1-sheilds and platforms versus the oceans and the orogenic zones. We calculate a mean dynamic topography field (Fig. 4) and plot the harmonic rms for each combination of models considered (Fig. 5) together with the mean field (shown by the solid line with squares).

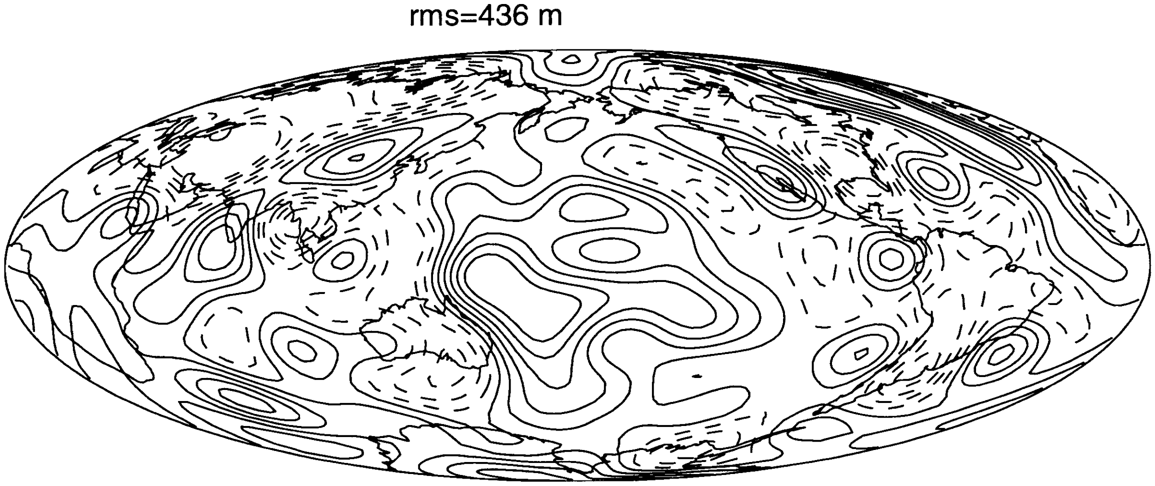

Figure V-4. A model of "observed" surface dynamic topography of spherical harmonic degree l=1-12. The field is contoured at 200 m interval (a), solid lines are for zero and positive values, dashed lines are for negative, the field rms is 340 m.

The assumption of global isostasy (no balancing) produces the fields which are shown by the dashed lines (Fig. 5, crests and circles are for the thick- and the thin-plate cooling models respectively). The dash-dotted lines are for continent-ocean balancing (pluses and triangles are for the thick- and the thin-plate cooling models respectively). The final type of baseline leveling, shield-platforms versus ocean-orogenic zones, is shown by the dotted lines (stars and diamonds are for the thick- and the thin-plate cooling models respectively). The resulting topography field has a spectral peak at degree l=2 with the decrease in the power to l=1 and l=3, and a relatively strong contribution from the higher harmonics (Fig. 5). The depressions are associated with the

Eurasian and American continents, and with the Circum Pacific. The oceans are generally uplifted together with Africa and Antarctica.

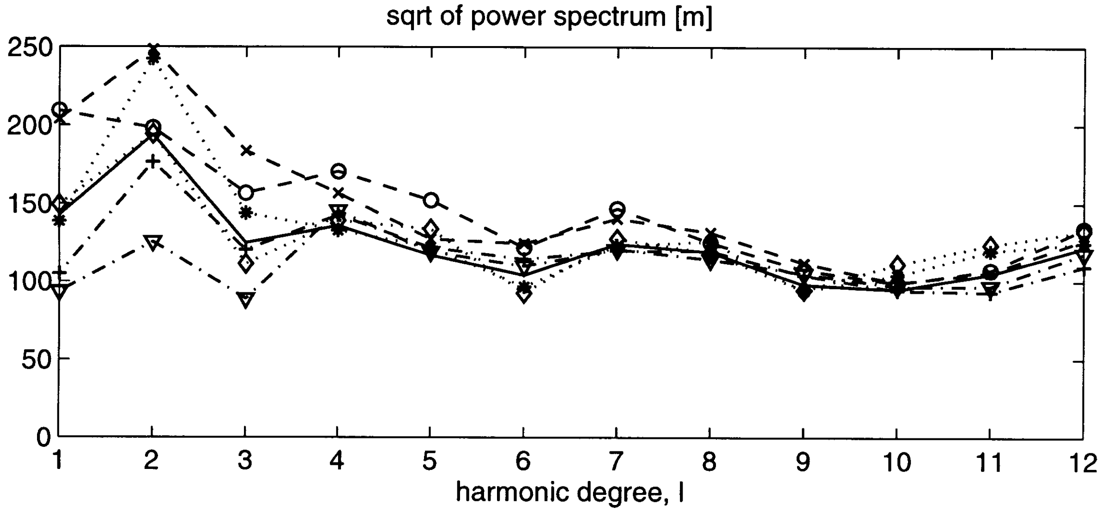

Figure V-5. Square root of power spectrum of a set of topography fields (non-solid lines) used to construct the final field (solid line) versus spherical harmonic degree. An assemblage consists of fields built under assumptions of thin- (open symbols) and thick-plate cooling (crossed symbols), global isostasy (dashed lines), continent vs. ocean (dash-dotted lines), and shield-platform vs. ocean-orogenic zones (dotted lines) baseline leveling.

For the set of six modeled dynamic topography fields, we calculate the standard deviation from the mean for each *lm*-coefficient according Eq. 10. The total errors (the sum of the data- and the model-related uncertainties) are shown by the line with circles in Fig. 6, together with the mean field rms (line with squares) versus the degree and order of spherical harmonics. The dynamic topography (Fig. 4) and the uncertainties (Fig. 6) can be used in geophysical analyses involving knowledge of the "observed" dynamic topography. As an example, we used them in a joint, geoid-topography, inversion for the mantle viscosity profile as the dynamic topography field and the associated, observational errors, $\sigma^2_{\mathrm{obs}} = \langle \sigma^2_{lm} \rangle$ (see Chapter IV).

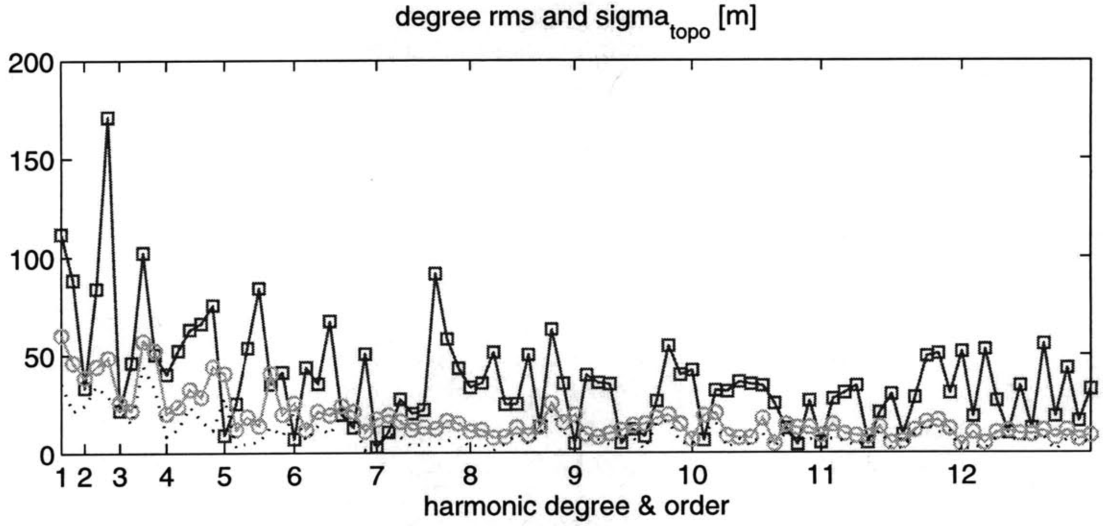

Figure V-6. The degree rms of the surface dynamic topography field (solid line with the squares) in meters versus the spherical harmonic degree and order. The signal is compared with the total observational error rms (circles) and the data-error rms (dots).

DISCUSSION

The ambiguity associated with the correction models has been apparent from comparing the global dynamic topography models calculated previously (e.g. Hager *et al.* 1985; Cazenave *et al.* 1988; Hager and Clayton 1989; Forte 1993). Our way of estimating and including the errors into the analysis allows us to describe the general features of the topography (such as Central Pacific and Africa Uplifts, or Circum Pacific and North America lows) and their amplitudes without tying the field to the poorly constrained regions, such as questionable depressions under all the continents.

Finally, we relate the dynamic topography model to the dynamic topography predicted from mantle flow driven by deeply settled density anomalies. The description of the inverse procedure can be found in Chapter 4. The "observed" dynamic topography is shown in Fig. 4. Its spectral amplitude is shown in Fig. 7 (solid line with stars), with the standard deviation shaded. The three minimums obtained during the inversion predict the dynamic topography fields displayed by the solid line with squares (first solution-family), by the dashed crossed line (second family), and by the circled dash-dotted line (third family), with the error bars corresponding to one standard deviation. Although the amplitudes of the fields are the same order of magnitude, there is a striking difference in the power of the higher harmonics. The dynamic topography generated by mantle flow displays a maximum at *l*=2 and the power gradually declines at the shorter wavelengths. However for the estimated dynamic topography, the contribution from the higher orders is as strong as for *l*=3.

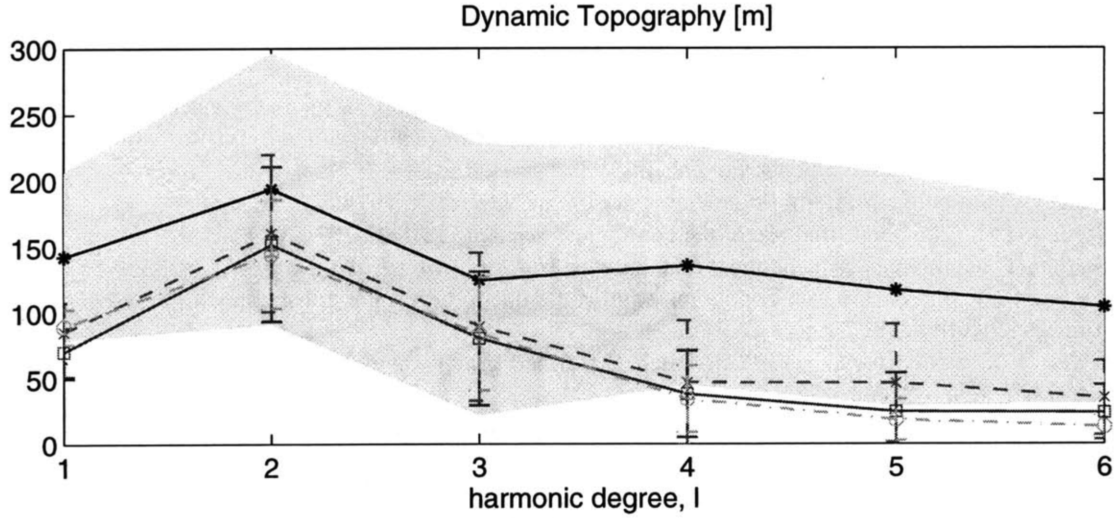

Figure V-7. The square root of the power of the surface dynamic topography fields versus spherical harmonic degree (abscissa). The estimated field is shown by the solid line, with stars surrounded by the gray shading representing the uncertainties associated with each harmonic. The calculated fields are shown by the lines, with the error-bars corresponding to the standard deviation around the mean. The data are for the first, second, and third families of η-profiles (the solid line with squares, the dashed line with crosses, and the dash-dotted line with circles, respectively).

ACKNOWLEDGMENTS

We thank Gabi Laske and Walter Moony for providing us with their latest crust model, and Müller *et al.* for sharing their ocean-floor age data and related errors through a www-site. Financial support was provided by NSF Grant EAR95-06427.

REFERENCES

Cazenave, A., Dominh, K., Rabinowicz, M., and G. Ceuleneer, Geoid and depth anomalies over ocean swells and throughs: evidence for an increasing trend of the geoid to depth ratio with age of plate, *J. Geophys. Res.*, *93*, 8064-8077, 1988.

Cazenave, A., and B. Lago, Long wavelength topography, seafloor subsidence and flattening, *Geophys. Res. Lett.*, *18*, 1257-1260, 1991.

Colin, P., and L. Fleitout, Topography of the ocean floor: Thermal evolution of the lithosphere and interaction of mantle heterogeneities with the lithosphere, *Geophys. Res. Lett.*, *11*, 1961-1964, 1990.

Dziewonski, A.M., B.H. Hager, and R.J. O'Connell, Large-scale heterogeneities in the lower mantle, *J. Geophys. Res.*, *82*, 239-255, 1977.

Forte, A.M., Peltier, W.R., Dziewonski, A.M., and R.L. Woodward, Dynamic surface topography: a new interpretation based upon mantle flow models derived from seismic tomography, *Geophys. Res. Lett.*, *20*, 225-228, 1993.

Garland, G.D., *The Earth's shape and gravity*, Pergamon Press, Oxford, 1977.

Gurnis, M., Bounds on global dynamic topography from Phanerozoic flooding of continental platforms, *Nature, 344*, 754-756, 1990.

Gurnis, M., Phanerozoic marine inundation of continents driven by dynamic topography above subducting slabs, *Nature, 364*, 589-593, 1993.

Hager, B.H., Clayton, R.W., Richards, M.A., Comer R.P., and A.M. Dziewonski, Lower mantle heterogeneity, dynamic topography and the geoid, *Nature, 313*, 541-545, 1985.

Hager, B.H., and R.W. Clayton, Constraints on the structure of mantle convection using seismic observations, flow models, and the geoid, in *Mantle Convection*, edited by W.R. Peltier, pp. 657-763, Gordon and Breach Science Publishers, 1989.

Jeffreys, H., *The Earth*, Cambridge University Press, New York, 1970.

Jordan, T.H., The deep structure of the continents, *Sci. Am., 240*, 92-107, 1979.

Jordan, T., Continents as a chemical boundary layer, *Phil. Trans. R. Soc. Lond. A, 301*, 359-373, 1981.

Le Stunff, Y, and Ricard, Y., Topography and geoid due to lithospheric mass anomalies, *Geophys. J. Int.*, *122*, 982-990, 1997.

Lerch, F.J., S.M. Klosko, and G.B. Patch, A refined gravity model from LAGEOS (GEM-L2), *NASA Tech. Memo 84986*, 1983.

Love, A.E.H., *Some problems in Geodynamics*, Cambridge University Press, 1911.

Marty, J.C., and A. Cazenave, Regional variations in subsidence rate of lithospheric plates: Implication for thermal cooling models, *Earth Planet. Sci. Lett. 94*, 301-315, 1989.

Mauk, F.J., A tectonic based Rayleigh wave group velocity model for prediction of dispersion character through ocean basins, *Ph.D. Thesis*, Univ. of Mich., Ann Arbor, 1977.

Mooney, W.D., Laske, G., and G. Masters, CRUST 5.1: A new global Crustal Model at 5x5 degrees, *J. Geophys. Res.*, in press, 1997.

Müller, R.D., Roest, W.R., Royer, J.-Y., Gahagan, L.M. and J.G. Sclater, Digital Isochrons of the World's Ocean Floor, submitted to *J. Geophys. Res.*, 1997.

Parsons, B., and J.G. Sclater, An analysis of the variation of the ocean floor bathymetry and heat flow with age, *J. Geophys. Res, 82*, 803-827, 1977.

Ricard, Y., M.A. Richards, C. Lithgow-Bertelloni, and Y. LeStunff, A geodynamic model of mantle heterogeneity, *J. Geophys. Res., 98*, 21,895-21,909, 1993.

Shapiro, S. S., Structure and dynamics of the continental tectosphere, Ph.D. Thesis, Mass. Inst. of Technology, 1995.

Stein, C.A., and A. Stein, A model for the global variation in oceanic depth and heat flow with lithospheric age, *Nature, 359*, 123-129, 1992.